

Measurement of Ratios of Fragmentation Fractions for Bottom Hadrons in $p\bar{p}$ Collisions at $\sqrt{s} = 1.96$ TeV

T. Aaltonen,²³ J. Adelman,¹³ T. Akimoto,⁵⁴ M.G. Albrow,¹⁷ B. Álvarez González,¹¹ S. Amerio,⁴² D. Amidei,³⁴ A. Anastassov,⁵¹ A. Annovi,¹⁹ J. Antos,¹⁴ M. Aoki,²⁴ G. Apollinari,¹⁷ A. Apresyan,⁴⁷ T. Arisawa,⁵⁶ A. Artikov,¹⁵ W. Ashmanskas,¹⁷ A. Attal,³ A. Aurisano,⁵² F. Azfar,⁴¹ P. Azzi-Bacchetta,⁴² P. Azzurri,⁴⁵ N. Bacchetta,⁴² W. Badgett,¹⁷ A. Barbaro-Galtieri,²⁸ V.E. Barnes,⁴⁷ B.A. Barnett,²⁵ S. Baroiant,⁷ V. Bartsch,³⁰ G. Bauer,³² P.-H. Beauchemin,³³ F. Bedeschi,⁴⁵ P. Bednar,¹⁴ S. Behari,²⁵ G. Bellettini,⁴⁵ J. Bellinger,⁵⁸ A. Belloni,²² D. Benjamin,¹⁶ A. Beretvas,¹⁷ J. Beringer,²⁸ T. Berry,²⁹ A. Bhatti,⁴⁹ M. Binkley,¹⁷ D. Bisello,⁴² I. Bizjak,³⁰ R.E. Blair,² C. Blocker,⁶ B. Blumenfeld,²⁵ A. Bocci,¹⁶ A. Bodek,⁴⁸ V. Boisvert,⁴⁸ G. Bolla,⁴⁷ A. Bolshov,³² D. Bortoletto,⁴⁷ J. Boudreau,⁴⁶ A. Boveia,¹⁰ B. Brau,¹⁰ A. Bridgeman,²⁴ L. Brigliadori,⁵ C. Bromberg,³⁵ E. Brubaker,¹³ J. Budagov,¹⁵ H.S. Budd,⁴⁸ S. Budd,²⁴ K. Burkett,¹⁷ G. Busetto,⁴² P. Bussey,²¹ A. Buzatu,³³ K. L. Byrum,² S. Cabrera^r,¹⁶ M. Campanelli,³⁵ M. Campbell,³⁴ F. Canelli,¹⁷ A. Canepa,⁴⁴ D. Carlsmith,⁵⁸ R. Carosi,⁴⁵ S. Carrillo^l,¹⁸ S. Carron,³³ B. Casal,¹¹ M. Casarsa,¹⁷ A. Castro,⁵ P. Catastini,⁴⁵ D. Cauz,⁵³ M. Cavalli-Sforza,³ A. Cerri,²⁸ L. Cerrito^p,³⁰ S.H. Chang,²⁷ Y.C. Chen,¹ M. Chertok,⁷ G. Chiarelli,⁴⁵ G. Chlachidze,¹⁷ F. Chlebana,¹⁷ K. Cho,²⁷ D. Chokheli,¹⁵ J.P. Chou,²² G. Choudalakis,³² S.H. Chuang,⁵¹ K. Chung,¹² W.H. Chung,⁵⁸ Y.S. Chung,⁴⁸ C.I. Ciobanu,²⁴ M.A. Ciocci,⁴⁵ A. Clark,²⁰ D. Clark,⁶ G. Compostella,⁴² M.E. Convery,¹⁷ J. Conway,⁷ B. Cooper,³⁰ K. Copic,³⁴ M. Cordelli,¹⁹ G. Cortiana,⁴² F. Crescioli,⁴⁵ C. Cuenca Almenar^r,⁷ J. Cuevas^o,¹¹ R. Culbertson,¹⁷ J.C. Cully,³⁴ D. Dagenhart,¹⁷ M. Datta,¹⁷ T. Davies,²¹ P. de Barbaro,⁴⁸ S. De Cecco,⁵⁰ A. Deisher,²⁸ G. De Lentdecker^d,⁴⁸ G. De Lorenzo,³ M. Dell'Orso,⁴⁵ L. Demortier,⁴⁹ J. Deng,¹⁶ M. Deninno,⁵ D. De Pedis,⁵⁰ P.F. Derwent,¹⁷ G.P. Di Giovanni,⁴³ C. Dionisi,⁵⁰ B. Di Ruzza,⁵³ J.R. Dittmann,⁴ M. D'Onofrio,³ S. Donati,⁴⁵ P. Dong,⁸ J. Donini,⁴² T. Dorigo,⁴² S. Dube,⁵¹ J. Efron,³⁸ R. Erbacher,⁷ D. Errede,²⁴ S. Errede,²⁴ R. Eusebi,¹⁷ H.C. Fang,²⁸ S. Farrington,²⁹ W.T. Fedorko,¹³ R.G. Feild,⁵⁹ M. Feindt,²⁶ J.P. Fernandez,³¹ C. Ferrazza,⁴⁵ R. Field,¹⁸ G. Flanagan,⁴⁷ R. Forrest,⁷ S. Forrester,⁷ M. Franklin,²² J.C. Freeman,²⁸ I. Furic,¹⁸ M. Gallinaro,⁴⁹ J. Galyardt,¹² F. Garberson,¹⁰ J.E. Garcia,⁴⁵ A.F. Garfinkel,⁴⁷ K. Genser,¹⁷ H. Gerberich,²⁴ D. Gerdes,³⁴ S. Giagu,⁵⁰ V. Giakoumopolou^a,⁴⁵ P. Giannetti,⁴⁵ K. Gibson,⁴⁶ J.L. Gimmell,⁴⁸ C.M. Ginsburg,¹⁷ N. Giokaris^a,¹⁵ M. Giordani,⁵³ P. Giromini,¹⁹ M. Giunta,⁴⁵ V. Glagolev,¹⁵ D. Glenzinski,¹⁷ M. Gold,³⁶ N. Goldschmidt,¹⁸ A. Golosanov,¹⁷ G. Gomez,¹¹ G. Gomez-Ceballos,³² M. Goncharov,⁵² O. González,³¹ I. Gorelov,³⁶ A.T. Goshaw,¹⁶ K. Goulianios,⁴⁹ A. Gresele,⁴² S. Grinstein,²² C. Grossi-Pilcher,¹³ R.C. Group,¹⁷ U. Grundler,²⁴ J. Guimaraes da Costa,²²

Z. Gunay-Unalan,³⁵ C. Haber,²⁸ K. Hahn,³² S.R. Hahn,¹⁷ E. Halkiadakis,⁵¹ A. Hamilton,²⁰
B.-Y. Han,⁴⁸ J.Y. Han,⁴⁸ R. Handler,⁵⁸ F. Happacher,¹⁹ K. Hara,⁵⁴ D. Hare,⁵¹ M. Hare,⁵⁵
S. Harper,⁴¹ R.F. Harr,⁵⁷ R.M. Harris,¹⁷ M. Hartz,⁴⁶ K. Hatakeyama,⁴⁹ J. Hauser,⁸
C. Hays,⁴¹ M. Heck,²⁶ A. Heijboer,⁴⁴ B. Heinemann,²⁸ J. Heinrich,⁴⁴ C. Henderson,³²
M. Herndon,⁵⁸ J. Heuser,²⁶ S. Hewamanage,⁴ D. Hidas,¹⁶ C.S. Hill^c,¹⁰ D. Hirschbuehl,²⁶
A. Hocker,¹⁷ S. Hou,¹ M. Houlden,²⁹ S.-C. Hsu,⁹ B.T. Huffman,⁴¹ R.E. Hughes,³⁸
U. Husemann,⁵⁹ J. Huston,³⁵ J. Incandela,¹⁰ G. Introzzi,⁴⁵ M. Iori,⁵⁰ A. Ivanov,⁷
B. Iyutin,³² E. James,¹⁷ B. Jayatilaka,¹⁶ D. Jeans,⁵⁰ E.J. Jeon,²⁷ S. Jindariani,¹⁸
W. Johnson,⁷ M. Jones,⁴⁷ K.K. Joo,²⁷ S.Y. Jun,¹² J.E. Jung,²⁷ T.R. Junk,²⁴ T. Kamon,⁵²
D. Kar,¹⁸ P.E. Karchin,⁵⁷ Y. Kato,⁴⁰ R. Kephart,¹⁷ U. Kerzel,²⁶ V. Khotilovich,⁵²
B. Kilminster,³⁸ D.H. Kim,²⁷ H.S. Kim,²⁷ J.E. Kim,²⁷ M.J. Kim,¹⁷ S.B. Kim,²⁷ S.H. Kim,⁵⁴
Y.K. Kim,¹³ N. Kimura,⁵⁴ L. Kirsch,⁶ S. Klimentko,¹⁸ M. Klute,³² B. Knuteson,³² B.R. Ko,¹⁶
S.A. Koay,¹⁰ K. Kondo,⁵⁶ D.J. Kong,²⁷ J. Konigsberg,¹⁸ A. Korytov,¹⁸ A.V. Kotwal,¹⁶
J. Kraus,²⁴ M. Kreps,²⁶ J. Kroll,⁴⁴ N. Krumnack,⁴ M. Kruse,¹⁶ V. Krutelyov,¹⁰
T. Kubo,⁵⁴ S. E. Kuhlmann,² T. Kuhr,²⁶ N.P. Kulkarni,⁵⁷ Y. Kusakabe,⁵⁶ S. Kwang,¹³
A.T. Laasanen,⁴⁷ S. Lai,³³ S. Lami,⁴⁵ S. Lammel,¹⁷ M. Lancaster,³⁰ R.L. Lander,⁷
K. Lannon,³⁸ A. Lath,⁵¹ G. Latino,⁴⁵ I. Lazzizzera,⁴² T. LeCompte,² J. Lee,⁴⁸ J. Lee,²⁷
Y.J. Lee,²⁷ S.W. Lee^q,⁵² R. Lefèvre,²⁰ N. Leonardo,³² S. Leone,⁴⁵ S. Levy,¹³ J.D. Lewis,¹⁷
C. Lin,⁵⁹ C.S. Lin,²⁸ J. Linacre,⁴¹ M. Lindgren,¹⁷ E. Lipeles,⁹ A. Lister,⁷ D.O. Litvintsev,¹⁷
T. Liu,¹⁷ N.S. Lockyer,⁴⁴ A. Loginov,⁵⁹ M. Loreti,⁴² L. Lovas,¹⁴ R.-S. Lu,¹ D. Lucchesi,⁴²
J. Lueck,²⁶ C. Luci,⁵⁰ P. Lujan,²⁸ P. Lukens,¹⁷ G. Lungu,¹⁸ L. Lyons,⁴¹ J. Lys,²⁸ R. Lysak,¹⁴
E. Lytken,⁴⁷ P. Mack,²⁶ D. MacQueen,³³ R. Madrak,¹⁷ K. Maeshima,¹⁷ K. Makhoul,³²
T. Maki,²³ P. Maksimovic,²⁵ S. Malde,⁴¹ S. Malik,³⁰ G. Manca,²⁹ A. Manousakis^a,¹⁵
F. Margaroli,⁴⁷ C. Marino,²⁶ C.P. Marino,²⁴ A. Martin,⁵⁹ M. Martin,²⁵ V. Martinj,²¹
M. Martínez,³ R. Martínez-Ballarín,³¹ T. Maruyama,⁵⁴ P. Mastrandrea,⁵⁰ T. Masubuchi,⁵⁴
M.E. Mattson,⁵⁷ P. Mazzanti,⁵ K.S. McFarland,⁴⁸ P. McIntyre,⁵² R. McNultyⁱ,²⁹
A. Mehta,²⁹ P. Mehtala,²³ S. Menzemer^k,¹¹ A. Menzione,⁴⁵ P. Merkel,⁴⁷ C. Mesropian,⁴⁹
A. Messina,³⁵ T. Miao,¹⁷ N. Miladinovic,⁶ J. Miles,³² R. Miller,³⁵ C. Mills,²² M. Milnik,²⁶
A. Mitra,¹ G. Mitselmakher,¹⁸ H. Miyake,⁵⁴ S. Moed,²² N. Moggi,⁵ C.S. Moon,²⁷
R. Moore,¹⁷ M. Morello,⁴⁵ P. Movilla Fernandez,²⁸ J. Mülmenstädt,²⁸ A. Mukherjee,¹⁷
Th. Muller,²⁶ R. Mumford,²⁵ P. Murat,¹⁷ M. Mussini,⁵ J. Nachtman,¹⁷ Y. Nagai,⁵⁴
A. Nagano,⁵⁴ J. Naganoma,⁵⁶ K. Nakamura,⁵⁴ I. Nakano,³⁹ A. Napier,⁵⁵ V. Necula,¹⁶
C. Neu,⁴⁴ M.S. Neubauer,²⁴ J. Nielsen^f,²⁸ L. Nodulman,² M. Norman,⁹ O. Norniella,²⁴
E. Nurse,³⁰ S.H. Oh,¹⁶ Y.D. Oh,²⁷ I. Oksuzian,¹⁸ T. Okusawa,⁴⁰ R. Oldeman,²⁹ R. Orava,²³
K. Osterberg,²³ S. Pagan Griso,⁴² C. Pagliarone,⁴⁵ E. Palencia,¹⁷ V. Papadimitriou,¹⁷
A. Papaikonomou,²⁶ A.A. Paramonov,¹³ B. Parks,³⁸ S. Pashapour,³³ J. Patrick,¹⁷
G. Pauletta,⁵³ M. Paulini,¹² C. Paus,³² D.E. Pellett,⁷ A. Penzo,⁵³ T.J. Phillips,¹⁶

G. Piacentino,⁴⁵ J. Piedra,⁴³ L. Pinera,¹⁸ K. Pitts,²⁴ C. Plager,⁸ L. Pondrom,⁵⁸ X. Portell,³
 O. Poukhov,¹⁵ N. Pounder,⁴¹ F. Prakoshyn,¹⁵ A. Pronko,¹⁷ J. Proudfoot,² F. Ptahos^{h, 17}
 G. Punzi,⁴⁵ J. Pursley,⁵⁸ J. Rademacker^{c, 41} A. Rahaman,⁴⁶ V. Ramakrishnan,⁵⁸
 N. Ranjan,⁴⁷ I. Redondo,³¹ B. Reisert,¹⁷ V. Rekovic,³⁶ P. Renton,⁴¹ M. Rescigno,⁵⁰
 S. Richter,²⁶ F. Rimondi,⁵ L. Ristori,⁴⁵ A. Robson,²¹ T. Rodrigo,¹¹ E. Rogers,²⁴ S. Rolli,⁵⁵
 R. Roser,¹⁷ M. Rossi,⁵³ R. Rossin,¹⁰ P. Roy,³³ A. Ruiz,¹¹ J. Russ,¹² V. Rusu,¹⁷
 H. Saarikko,²³ A. Safonov,⁵² W.K. Sakumoto,⁴⁸ G. Salamanna,⁵⁰ O. Saltó,³ L. Santi,⁵³
 S. Sarkar,⁵⁰ L. Sartori,⁴⁵ K. Sato,¹⁷ A. Savoy-Navarro,⁴³ T. Scheidle,²⁶ P. Schlabach,¹⁷
 E.E. Schmidt,¹⁷ M.A. Schmidt,¹³ M.P. Schmidt,⁵⁹ M. Schmitt,³⁷ T. Schwarz,⁷
 L. Scodellaro,¹¹ A.L. Scott,¹⁰ A. Scribano,⁴⁵ F. Scuri,⁴⁵ A. Sedov,⁴⁷ S. Seidel,³⁶ Y. Seiya,⁴⁰
 A. Semenov,¹⁵ L. Sexton-Kennedy,¹⁷ A. Sfyrla,²⁰ S.Z. Shalhout,⁵⁷ M.D. Shapiro,²⁸
 T. Shears,²⁹ P.F. Shepard,⁴⁶ D. Sherman,²² M. Shimojima^{n, 54} M. Shochet,¹³ Y. Shon,⁵⁸
 I. Shreyber,²⁰ A. Sidoti,⁴⁵ P. Sinervo,³³ A. Sisakyan,¹⁵ A.J. Slaughter,¹⁷ J. Slaunwhite,³⁸
 K. Sliwa,⁵⁵ J.R. Smith,⁷ F.D. Snider,¹⁷ R. Snihur,³³ M. Soderberg,³⁴ A. Soha,⁷
 S. Somalwar,⁵¹ V. Sorin,³⁵ J. Spalding,¹⁷ F. Spinella,⁴⁵ T. Spreitzer,³³ P. Squillaciotti,⁴⁵
 M. Stanitzki,⁵⁹ R. St. Denis,²¹ B. Stelzer,⁸ O. Stelzer-Chilton,⁴¹ D. Stentz,³⁷ J. Strologas,³⁶
 D. Stuart,¹⁰ J.S. Suh,²⁷ A. Sukhanov,¹⁸ H. Sun,⁵⁵ I. Suslov,¹⁵ T. Suzuki,⁵⁴ A. Taffard^{e, 24}
 R. Takashima,³⁹ Y. Takeuchi,⁵⁴ R. Tanaka,³⁹ M. Tecchio,³⁴ P.K. Teng,¹ K. Terashi,⁴⁹
 J. Thom^{g, 17} A.S. Thompson,²¹ G.A. Thompson,²⁴ E. Thomson,⁴⁴ P. Tipton,⁵⁹ V. Tiwari,¹²
 S. Tkaczyk,¹⁷ D. Toback,⁵² S. Tokar,¹⁴ K. Tollefson,³⁵ T. Tomura,⁵⁴ D. Tonelli,¹⁷
 S. Torre,¹⁹ D. Torretta,¹⁷ S. Tourneur,⁴³ W. Trischuk,³³ Y. Tu,⁴⁴ N. Turini,⁴⁵
 F. Ukegawa,⁵⁴ S. Uozumi,⁵⁴ S. Vallecorsa,²⁰ N. van Remortel,²³ A. Varganov,³⁴
 E. Vataga,³⁶ F. Vázquez^{l, 18} G. Velev,¹⁷ C. Vellidis^{a, 45} V. Veszpremi,⁴⁷ M. Vidal,³¹
 R. Vidal,¹⁷ I. Vila,¹¹ R. Vilar,¹¹ T. Vine,³⁰ M. Vogel,³⁶ I. Volobouev^{q, 28} G. Volpi,⁴⁵
 F. Würthwein,⁹ P. Wagner,⁴⁴ R.G. Wagner,² R.L. Wagner,¹⁷ J. Wagner-Kuhr,²⁶
 W. Wagner,²⁶ T. Wakisaka,⁴⁰ R. Wallny,⁸ S.M. Wang,¹ A. Warburton,³³ D. Waters,³⁰
 M. Weinberger,⁵² W.C. Wester III,¹⁷ B. Whitehouse,⁵⁵ D. Whiteson^{e, 44} A.B. Wicklund,²
 E. Wicklund,¹⁷ G. Williams,³³ H.H. Williams,⁴⁴ P. Wilson,¹⁷ B.L. Winer,³⁸ P. Wittich^{g, 17}
 S. Wolbers,¹⁷ C. Wolfe,¹³ T. Wright,³⁴ X. Wu,²⁰ S.M. Wynne,²⁹ A. Yagil,⁹ K. Yamamoto,⁴⁰
 J. Yamaoka,⁵¹ T. Yamashita,³⁹ C. Yang,⁵⁹ U.K. Yang^{m, 13} Y.C. Yang,²⁷ W.M. Yao,²⁸
 G.P. Yeh,¹⁷ J. Yoh,¹⁷ K. Yorita,¹³ T. Yoshida,⁴⁰ G.B. Yu,⁴⁸ I. Yu,²⁷ S.S. Yu,¹⁷ J.C. Yun,¹⁷
 L. Zanello,⁵⁰ A. Zanetti,⁵³ I. Zaw,²² X. Zhang,²⁴ Y. Zheng^{b, 8} and S. Zucchelli⁵

(CDF Collaboration*)

* With visitors from ^aUniversity of Athens, 15784 Athens, Greece, ^bChinese Academy of Sciences, Beijing 100864, China, ^cUniversity of Bristol, Bristol BS8 1TL, United Kingdom, ^dUniversity Libre de Bruxelles, B-1050 Brussels, Belgium, ^eUniversity of California Irvine, Irvine, CA 92697, ^fUniversity of California

¹*Institute of Physics, Academia Sinica,
Taipei, Taiwan 11529, Republic of China*

²*Argonne National Laboratory, Argonne, Illinois 60439*

³*Institut de Fisica d'Altes Energies,
Universitat Autonoma de Barcelona,
E-08193, Bellaterra (Barcelona), Spain*

⁴*Baylor University, Waco, Texas 76798*

⁵*Istituto Nazionale di Fisica Nucleare,
University of Bologna, I-40127 Bologna, Italy*

⁶*Brandeis University, Waltham, Massachusetts 02254*

⁷*University of California, Davis, Davis, California 95616*

⁸*University of California, Los Angeles, Los Angeles, California 90024*

⁹*University of California, San Diego, La Jolla, California 92093*

¹⁰*University of California, Santa Barbara, Santa Barbara, California 93106*

¹¹*Instituto de Fisica de Cantabria, CSIC-University of Cantabria, 39005 Santander, Spain*

¹²*Carnegie Mellon University, Pittsburgh, PA 15213*

¹³*Enrico Fermi Institute, University of Chicago, Chicago, Illinois 60637*

¹⁴*Comenius University, 842 48 Bratislava,
Slovakia; Institute of Experimental Physics, 040 01 Kosice, Slovakia*

¹⁵*Joint Institute for Nuclear Research, RU-141980 Dubna, Russia*

¹⁶*Duke University, Durham, North Carolina 27708*

¹⁷*Fermi National Accelerator Laboratory, Batavia, Illinois 60510*

¹⁸*University of Florida, Gainesville, Florida 32611*

¹⁹*Laboratori Nazionali di Frascati, Istituto Nazionale
di Fisica Nucleare, I-00044 Frascati, Italy*

²⁰*University of Geneva, CH-1211 Geneva 4, Switzerland*

²¹*Glasgow University, Glasgow G12 8QQ, United Kingdom*

²²*Harvard University, Cambridge, Massachusetts 02138*

²³*Division of High Energy Physics, Department of Physics,
University of Helsinki and Helsinki Institute of Physics, FIN-00014, Helsinki, Finland*

²⁴*University of Illinois, Urbana, Illinois 61801*

²⁵*The Johns Hopkins University, Baltimore, Maryland 21218*

Santa Cruz, Santa Cruz, CA 95064, ⁹Cornell University, Ithaca, NY 14853, ^hUniversity of Cyprus, Nicosia CY-1678, Cyprus, ⁱUniversity College Dublin, Dublin 4, Ireland, ^jUniversity of Edinburgh, Edinburgh EH9 3JZ, United Kingdom, ^kUniversity of Heidelberg, D-69120 Heidelberg, Germany, ^lUniversidad Iberoamericana, Mexico D.F., Mexico, ^mUniversity of Manchester, Manchester M13 9PL, England, ⁿNagasaki Institute of Applied Science, Nagasaki, Japan, ^oUniversity de Oviedo, E-33007 Oviedo, Spain, ^pQueen Mary, University of London, London, E1 4NS, England, ^qTexas Tech University, Lubbock, TX 79409, ^rIFIC(CSIC-Universitat de Valencia), 46071 Valencia, Spain,

²⁶*Institut für Experimentelle Kernphysik,*

Universität Karlsruhe, 76128 Karlsruhe, Germany

²⁷*Center for High Energy Physics: Kyungpook National University,*

Daegu 702-701, Korea; Seoul National University, Seoul 151-742,

Korea; Sungkyunkwan University, Suwon 440-746,

Korea; Korea Institute of Science and Technology Information, Daejeon,

305-806, Korea; Chonnam National University, Gwangju, 500-757, Korea

²⁸*Ernest Orlando Lawrence Berkeley National Laboratory, Berkeley, California 94720*

²⁹*University of Liverpool, Liverpool L69 7ZE, United Kingdom*

³⁰*University College London, London WC1E 6BT, United Kingdom*

³¹*Centro de Investigaciones Energeticas*

Medioambientales y Tecnologicas, E-28040 Madrid, Spain

³²*Massachusetts Institute of Technology, Cambridge, Massachusetts 02139*

³³*Institute of Particle Physics: McGill University, Montréal,*

Canada H3A 2T8; and University of Toronto, Toronto, Canada M5S 1A7

³⁴*University of Michigan, Ann Arbor, Michigan 48109*

³⁵*Michigan State University, East Lansing, Michigan 48824*

³⁶*University of New Mexico, Albuquerque, New Mexico 87131*

³⁷*Northwestern University, Evanston, Illinois 60208*

³⁸*The Ohio State University, Columbus, Ohio 43210*

³⁹*Okayama University, Okayama 700-8530, Japan*

⁴⁰*Osaka City University, Osaka 588, Japan*

⁴¹*University of Oxford, Oxford OX1 3RH, United Kingdom*

⁴²*University of Padova, Istituto Nazionale di Fisica Nucleare,*

Sezione di Padova-Trento, I-35131 Padova, Italy

⁴³*LPNHE, Université Pierre et Marie*

Curie/IN2P3-CNRS, UMR7585, Paris, F-75252 France

⁴⁴*University of Pennsylvania, Philadelphia, Pennsylvania 19104*

⁴⁵*Istituto Nazionale di Fisica Nucleare Pisa, Universities of Pisa,*

Siena and Scuola Normale Superiore, I-56127 Pisa, Italy

⁴⁶*University of Pittsburgh, Pittsburgh, Pennsylvania 15260*

⁴⁷*Purdue University, West Lafayette, Indiana 47907*

⁴⁸*University of Rochester, Rochester, New York 14627*

⁴⁹*The Rockefeller University, New York, New York 10021*

⁵⁰*Istituto Nazionale di Fisica Nucleare, Sezione di Roma 1,*

University of Rome “La Sapienza,” I-00185 Roma, Italy

⁵¹*Rutgers University, Piscataway, New Jersey 08855*

⁵²*Texas A&M University, College Station, Texas 77843*

⁵³*Istituto Nazionale di Fisica Nucleare, University of Trieste/ Udine, Italy*

⁵⁴*University of Tsukuba, Tsukuba, Ibaraki 305, Japan*

⁵⁵*Tufts University, Medford, Massachusetts 02155*

⁵⁶*Waseda University, Tokyo 169, Japan*

⁵⁷*Wayne State University, Detroit, Michigan 48201*

⁵⁸*University of Wisconsin, Madison, Wisconsin 53706*

⁵⁹*Yale University, New Haven, Connecticut 06520*

(Dated: January 28, 2008)

Abstract

This paper describes the first measurement of b -quark fragmentation fractions into bottom hadrons in Run II of the Tevatron Collider at Fermilab. The result is based on a 360 pb^{-1} sample of data collected with the CDF II detector in $p\bar{p}$ collisions at $\sqrt{s} = 1.96 \text{ TeV}$. Semileptonic decays of \bar{B}^0 , B^- , and \bar{B}_s^0 mesons, as well as Λ_b^0 baryons, are reconstructed. For an effective bottom hadron p_T threshold of $7 \text{ GeV}/c$, the fragmentation fractions are measured to be $f_u/f_d = 1.054 \pm 0.018 \text{ (stat)} {}^{+0.025}_{-0.045} \text{ (sys)} \pm 0.058 (\mathcal{B})$, $f_s/(f_u + f_d) = 0.160 \pm 0.005 \text{ (stat)} {}^{+0.011}_{-0.010} \text{ (sys)} {}^{+0.057}_{-0.034} (\mathcal{B})$, and $f_{\Lambda_b}/(f_u + f_d) = 0.281 \pm 0.012 \text{ (stat)} {}^{+0.058}_{-0.056} \text{ (sys)} {}^{+0.128}_{-0.086} (\mathcal{B})$, where the uncertainty \mathcal{B} is due to uncertainties on measured branching ratios. The value of $f_s/(f_u + f_d)$ agrees within one standard deviation with previous CDF measurements and the world average of this quantity, which is dominated by LEP measurements. However, the ratio $f_{\Lambda_b}/(f_u + f_d)$ is approximately twice the value previously measured at LEP. The approximately 2σ discrepancy is examined in terms of kinematic differences between the two production environments.

PACS numbers: 13.20.He, 13.30.Ce, 14.20.Mr, 14.40.Nd, 14.65.Fy

I. INTRODUCTION

Bottom quarks, b , produced in $p\bar{p}$ collisions combine with anti-quarks or di-quarks to form bottom hadrons. In this process, called fragmentation, the color force field creates quark-antiquark pairs $q\bar{q}$ that combine with the bottom quark to create a \bar{B} meson $|b\bar{q}\rangle$ or b baryon $|bq_1q_2\rangle$. Since the fragmentation process, which is governed by the strong force, cannot be reliably calculated by perturbative QCD [1–3], the fragmentation properties of b quarks must be determined empirically. This paper describes a measurement of the species dependence of the b -quark fragmentation rates into bottom hadrons produced in $p\bar{p}$ collisions at center of mass energy $\sqrt{s} = 1.96$ TeV during Run II of the Tevatron collider at Fermilab.

The probabilities that the fragmentation of a b quark will result in a $B^- |b\bar{u}\rangle$, $\bar{B}^0 |b\bar{d}\rangle$, or $\bar{B}_s^0 |b\bar{s}\rangle$ meson or a $\Lambda_b^0 |bdu\rangle$ baryon are denoted by f_u , f_d , f_s , and f_{Λ_b} , respectively. In this paper, f_q indicates the fragmentation fraction integrated above the momentum threshold of sensitivity in the data: $f_q \equiv f_q(p_T(\bar{B}) > p_T^{min})$ [4]. In the case that the fragmentation fractions are momentum dependent, the measured fragmentation fractions are proportional to the relative yields of the bottom hadrons integrated above the effective p_T^{min} . The contributions from the production of excited bottom hadrons that decay into final states containing a B^- , \bar{B}^0 , \bar{B}_s^0 meson or Λ_b^0 baryon are implicitly included in this definition of the fragmentation fractions, $f_q \equiv \mathcal{B}(b \rightarrow B_q X)$. Throughout the paper, unless otherwise noted, references to a specific charge state are meant to imply the charge conjugate state as well.

In Run I of the Fermilab Tevatron, which collected data from 1992–1996, the fraction of \bar{B}_s^0 mesons produced relative to the number of \bar{B}^0 mesons was measured $\approx 2\sigma$ higher at CDF [5–7] than at the LEP experiments [8–10]. Interestingly, the time-integrated flavor averaged mixing parameter, $\bar{\chi} = f_d \chi_d + f_s \chi_s$, where χ_d and χ_s are the time-integrated mixing parameters of \bar{B}^0 and \bar{B}_s^0 mesons respectively, was also measured $\approx 2\sigma$ higher in Run I [11, 12] than the LEP averages of the same quantity [13–18]. This second discrepancy led to speculations about possible sources of the enhanced average mixing rate at a hadron collider relative to electron-positron collisions, including suggestions that new physics may be the source of the disagreement [19]. Since the average momentum of b quarks produced at LEP, $\langle p(b) \rangle \sim 40$ GeV/ c , is significantly higher than at the Tevatron, $\langle p(b) \rangle \sim 10$ GeV/ c , it is also possible that the fragmentation process depends on the b -quark momentum. Another possible explanation is that f_s is higher at the Tevatron than at LEP due to the different initial mechanism of b -quark production. Of course, a more mundane possibility is that the Run I results relating to f_s are simply statistical fluctuations. To shed light on the question of whether b -quark fragmentation is different in a hadron environment than in e^+e^- collisions, the fragmentation fractions are measured in CDF Run II with high statistical precision and an updated treatment of the lepton-charm sample composition.

The analysis strategy is as follows. Semileptonic decays of bottom hadrons, $\bar{B} \rightarrow \ell^- \bar{\nu}_\ell D X$, where ℓ^- stands for electron or muon, and D represents a charm meson or baryon, in case of semileptonic bottom baryon decays, unless otherwise specified, provide large sam-

ples for studying the fragmentation properties of b quarks. This measurement determines the b -quark fragmentation fractions by reconstructing five semileptonic signatures, $\ell^- D^+$, $\ell^- D^0$, $\ell^- D^{*+}$, $\ell^- D_s^+$, and $\ell^- \Lambda_c^+$. The selection requirements are kept similar among the five lepton-charm channels in order to cancel as many systematic uncertainties as possible. The final signal requirements, though similar, have been selected to maintain good acceptance for the individual decays, which have different kinematic features. The reconstructed $\ell^- D$ signal yields, originating from the various $\bar{B} \rightarrow \ell^- \bar{\nu}_\ell DX$ semileptonic decays, are then related to the numbers of bottom hadrons (B^- , \bar{B}^0 , \bar{B}_s^0 , or Λ_b^0) produced in the b -quark fragmentation process. Since the neutrino from the semileptonic bottom hadron decay is not reconstructed, the missing energy in the decay allows semileptonic bottom hadron decays to excited charm states to contribute to the five final state decay signatures. This results in “cross-talk” between the bottom hadron species, particularly between the \bar{B} mesons. The observed semileptonic $\ell^- D$ decay signatures are related to their corresponding parent bottom hadrons through a procedure used to extract the sample composition, as described later in the text. In order to reduce systematic uncertainties in trigger and tracking efficiencies, the b -quark fragmentation fractions are measured relative to f_d . This means that the relative fragmentation fractions f_u/f_d , $f_s/(f_u + f_d)$ and $f_{\Lambda_b}/(f_u + f_d)$ are extracted from the five lepton-charm yields, taking the sample composition into account. Since the fragmentation of b quarks into b baryons other than the Λ_b^0 are ignored, a constraint requiring the fragmentation fractions f_u , f_d , f_s , and f_{Λ_b} to sum to unity is not applied.

This paper is organized as follows. The semileptonic signal reconstruction is discussed in Section II, while the sample composition procedure used to relate the lepton-charm signatures to the parent bottom hadron is described in Section III. The efficiencies needed to extract the sample composition are determined in Section IV. The fit to the fragmentation fractions is detailed in Section V. Finally, the systematic uncertainties assigned to the measurement are described in Section VI and the final results are discussed in Section VII.

II. DATA RECONSTRUCTION

A. Experimental Apparatus

The data used in this measurement represent an integrated luminosity of approximately 360 pb^{-1} collected with the CDF II detector between February 2002, and August 2004. The CDF detector employs a cylindrical geometry around the $p\bar{p}$ interaction region with the proton direction defining the positive z -direction. Most of the quantities used for candidate selection are measured in the plane transverse to the z -axis. In the CDF coordinate system, φ is the azimuthal angle, θ is the polar angle measured from the proton direction, and r is the radius perpendicular to the beam axis. The pseudorapidity η is defined as $\eta = -\ln[\tan(\theta/2)]$. The transverse momentum, p_T , is the component of the track momentum, p ,

transverse to the z -axis ($p_T = p \cdot \sin \theta$), while $E_T = E \cdot \sin \theta$, with E being the energy measured in the calorimeter.

The CDF II detector features excellent lepton identification and charged particle tracking and is described in detail elsewhere [20, 21]. The parts of the detector relevant to the reconstruction of semileptonic bottom hadron decays used in this measurement are briefly summarized below. The detector nearest to the $p\bar{p}$ interaction region is a silicon vertex detector (SVX II) [22], which consists of five concentric layers of double-sided sensors located at radii between 2.5 and 10.6 cm. An additional single layer of silicon (L00) [23] is mounted on the beam pipe at radius $r \sim 1.5$ cm, but the information from this detector is not used in this measurement. In addition, two forward layers plus one central layer of double sided silicon located outside the SVX at radii of 20-29 cm make up the intermediate silicon layers (ISL) [24]. Together with the SVX II, the ISL detector extends the sensitive region of the CDF II tracking detector to $|\eta| \leq 2.0$. CDF's silicon system provides three-dimensional track reconstruction and is used to identify displaced vertices associated with bottom hadron decays. The measurement of the momentum of charged particles in the silicon detector is significantly improved with the central outer tracker (COT) [25], an open-cell drift chamber with 30,200 sense wires arranged in 96 layers combined into four axial and four stereo super-layers (SL). It provides tracking from a radius of ~ 40 cm out to a radius of 132 cm covering $|z| < 155$ cm. The track reconstruction efficiency of the COT is found to be $(99.6^{+0.4}_{-0.9})\%$ for charged particles with $p_T > 1.5$ GeV/ c [26] and $\gtrsim 94\%$ [27] for charged particles with $p_T = 0.4$ GeV/ c . For high-momentum charged particles, the p_T resolution is found to be $\sigma(p_T)/p_T = 0.0015$ $p_T/\text{GeV}/c$. The COT also provides specific energy loss, dE/dx , information for charged particle identification with a separation between pions and kaons of approximately 1.4σ [28]. The central tracking system is immersed in a superconducting solenoid that provides a 1.4 T axial magnetic field.

Electromagnetic (CEM) [29] and hadronic (CHA) [30] calorimeters are located outside the COT and the solenoid, where they are arranged in a projective-tower geometry. The electromagnetic and hadronic calorimeters are lead-scintillator and iron-scintillator sampling devices, respectively. The energy resolution for the CDF central calorimeter is $\sigma(E_T)/E_T = [(13.5\%/\sqrt{E_T})^2 + (1.5\%)^2]^{1/2}$ for electromagnetic showers [29, 31] and $\sigma(E_T)/E_T = [(75\%/\sqrt{E_T})^2 + (3\%)^2]^{1/2}$ for hadrons [21, 30], where E_T is measured in GeV. A layer of proportional chambers (CES), with wire and strip readout, is located six radiation lengths deep in the CEM calorimeters, near the electromagnetic shower maximum. The CES provides a measurement of electromagnetic shower profiles in both the φ - and z -directions for use in electron identification. Muon candidates are identified with two sets of multi-layer drift chambers and scintillator counters [32, 33], one located outside the calorimeters (CMU) and the other (CMP) behind an additional 60 cm of iron shielding, equivalent to approximately 3 pion interaction lengths. The CMU provides coverage for particles with $|\eta| < 0.6$ and $p_T > 1.4$ GeV/ c . The CMP covers the same pseudorapidity region, but identifies muons with $p_T > 2.0$ GeV/ c with higher purity than muons reconstructed in the CMU only.

B. Trigger Requirements

CDF uses a three-level trigger system [21], where each level provides a rate reduction sufficient to allow for processing at the next level with minimal dead-time. At level 1, data from every beam crossing are stored in a pipeline memory capable of buffering data for $\approx 5.5\mu\text{s}$. The level 1 trigger either rejects an event or copies the data into one of four level 2 buffers. At level 2, a substantial fraction of the event data is available for analysis by the dedicated trigger processors. Events that pass the level 1 and level 2 trigger selection criteria are then sent to the level 3 trigger [34, 35], a cluster of computers running a speed-optimized reconstruction code. Events selected by level 3 are written to permanent mass storage.

Tracking plays a significant role in the triggers utilized for this analysis. Semileptonic $\bar{B} \rightarrow \ell^-\bar{\nu}_\ell DX$ decays are recorded using a trigger that requires a lepton and a track displaced from the interaction point and identified with the silicon vertex trigger (SVT) [36]. The decay topology of semileptonic B decays is sketched in Fig. 1. Tracks are reconstructed at level 1 with the extremely fast tracker (XFT) [37] by examining COT hits from the four axial super-layers. The XFT provides r - φ tracking information and can identify tracks with $p_T > 1.5 \text{ GeV}/c$ with high efficiency ($> 90\%$) and good transverse momentum resolution, $\sigma(p_T)/p_T = 0.016 p_T/[\text{GeV}/c]$. XFT tracks can be matched with either calorimeter clusters to identify electron candidates or with track segments in the muon detectors to identify muon candidates. The XFT tracks are extrapolated into the silicon detector system, where the SVT uses the SVX II measurements of charge deposits from charged particles to form simplified tracks. In addition, the SVT determines the distance of closest approach in the transverse plane, d_0 , with respect to the $p\bar{p}$ beam line, which is determined from a time-dependent line fit to the locus of primary interaction vertices determined from all tracks available at trigger level (see Fig. 1). The impact parameter resolution of the SVT is approximately $50 \mu\text{m}$ [36, 38], which includes a contribution of $35 \mu\text{m}$ from the width of the $p\bar{p}$ interaction region [39].

The primary trigger used in this measurement requires that the lepton and the displaced track (SVT track) must have transverse momentum values greater than $4 \text{ GeV}/c$ and $2 \text{ GeV}/c$, respectively. The displaced track's impact parameter, d_0 , must exceed $120 \mu\text{m}$ and be less than 1 mm to reject decay products of long-lived hadrons decays such as K_S^0 or Λ^0 . The opening angle, $\Delta\phi$, between the lepton and SVT track is required to satisfy $2^\circ \leq \Delta\phi(\ell^-, \text{SVT track}) \leq 90^\circ$ to increase the probability that the two tracks originate from the same \bar{B} hadron. Additionally, the invariant mass between the trigger lepton and SVT triggered track must be less than the nominal bottom hadron mass, $m(\ell^-, \text{SVT track}) \equiv \sqrt{(p^\mu(\ell^-) + p'^\mu(\text{SVT}))^2} < 5 \text{ GeV}/c^2$, where the SVT track is assumed to have the pion mass. The trigger lepton requirements are described in conjunction with their analysis selections in Section II C 1. Events that pass these trigger requirements are recorded to the lepton plus SVT trigger data stream for further analysis. In this measurement both the muon and electron plus SVT trigger data ($e+\text{SVT}$ and $\mu+\text{SVT}$) are used.

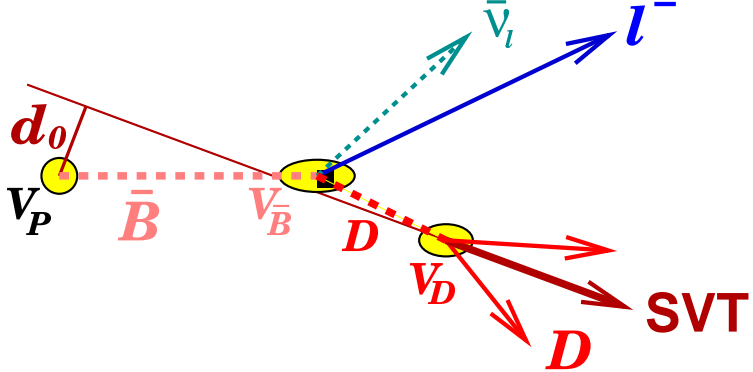


FIG. 1: Sketch of semileptonic B -decay topology in the transverse plane, where V_P is the primary vertex, V_B is the decay vertex of the bottom hadron, V_D is the decay vertex of the charm hadron, and d_0 is defined in the text. “SVT” indicates the track selected by the displaced track SVT trigger, which is also defined in the text.

An additional trigger utilized for selecting \bar{B} events is the two-track trigger (TTT), which requires two displaced tracks. Large semileptonic \bar{B} samples are also available with this trigger [40, 41], although the false lepton background is much larger as well. Semileptonic events from the TTT are used in this analysis for a study of the systematic uncertainty arising from false leptons.

C. Data Selection and Reconstruction

Events from the lepton plus SVT trigger data stream are used to reconstruct semileptonic bottom hadron decays in this analysis. First, trigger leptons are identified by re-confirming the trigger decision with offline quantities after event reconstruction. Charm candidates are then reconstructed, with the SVT track required to match one of the daughter tracks from the charm decay. The selections on the lepton-charm signals obtained are optimized to reduce combinatoric background and improve signal significance. Non-combinatoric backgrounds in the charm signals are handled separately.

1. Trigger Lepton Identification

The data analysis begins by identifying the trigger leptons from the e +SVT and μ +SVT trigger streams. The electron candidates are identified by requiring the following selection criteria. The longitudinal shower profile must be consistent with that of an electron shower, with a leakage energy from the CEM into the CHA of less than 12.5%, in order to suppress hadron contamination. The lateral shower profile of the CEM cluster is required to be consistent with a profile obtained from test beam electrons after appropriate corrections. The association of a single track with the calorimeter shower is made based on the position

matching at the CES plane, with both $|\Delta z \cdot \sin \theta| < 5$ cm and $r|\Delta\varphi| < 3$ cm conditions required. To achieve good agreement between data and Monte Carlo (MC) simulation (see Sec. IV A), an isolation requirement is applied to the trigger electron candidates by requiring that exactly only one track is found that projects to the CEM towers used to define the electron energy. To reconfirm electron trigger cuts, the offline reconstructed E_T and p_T of the electron candidate are required to be greater than 4 GeV and 4 GeV/ c , respectively. Additionally, electron candidates from photon conversions in the detector material are removed by rejecting those electron candidates that have a small opening angle with oppositely charged particles in the event.

Trigger muon candidates are reconstructed by extrapolating tracks measured in the COT to the muon system, where they are matched to track segments (stubs) reconstructed in the muon chambers. A CMU or CMP stub is required to have hits in at least three out of the four layers of planar drift chambers. Trigger muons are required to have hits in both the CMU and CMP muon chambers. The separation between a track segment reconstructed in the muon chamber and the extrapolated COT track is computed. The uncertainty in this quantity is dominated by multiple scattering in the traversed detector material. For good track to stub matching, this separation is required to be less than 15 cm and 20 cm in the $r\varphi$ -view for CMU and CMP, respectively. The transverse momentum of a muon candidate reconstructed offline is required to be greater than 4 GeV/ c .

2. Charm Candidate Selection

The SVT track is required to match one of the final state tracks in the five reconstructed charm signals: $D^0 \rightarrow K^-\pi^+$, $D^{*+} \rightarrow D^0 (\rightarrow K^-\pi^+) \pi^+$, $D^+ \rightarrow K^-\pi^+\pi^+$, $D_s^+ \rightarrow \phi (\rightarrow K^+K^-)\pi^+$, and $\Lambda_c^+ \rightarrow pK^-\pi^+$. Only well-reconstructed tracks with $p_T \geq 0.4$ GeV/ c and at least three silicon $r\varphi$ hits are retained for offline analysis. To ensure good track quality, all charm daughter tracks, except for the soft pion from the D^{*+} decay, are required to have at least five hits in at least two axial and two stereo COT super-layers. There are no COT requirements on the D^{*+} soft pion. During data reconstruction the track parameters are corrected for the ionization energy loss appropriate to the mass hypothesis under consideration. In addition, tracks are required to be fiducial in the COT, so that only tracks which are well-described by the simulation (see Sec. IV A) are used for further analysis. In particular, tracks that fall within $|z| \leq 1.5$ cm of the COT mid-plane, where no track information is recorded, and tracks that originate outside of the COT volume at $|z| \geq 155$ cm are excluded from the analysis. In addition, all tracks must at least pass through the axial SL 6 before exiting the COT. This means the exit radius of the track must be greater than the radius of the sixth super-layer $r_{SL6} = 106$ cm. This requirement is tightened for the SVT trigger track and the trigger lepton. Both tracks must pass through SL 8 of the COT ($r_{SL8} = 131$ cm) as required in the trigger. The invariant mass of the $D^0 \rightarrow K^-\pi^+$ and

$D^+ \rightarrow K^-\pi^+\pi^+$ is reconstructed within [1.40, 2.00] GeV/c^2 and [1.70, 2.00] GeV/c^2 , respectively. The reconstructed $D_s^+ \rightarrow \phi\pi^+$ mass is required to be within [1.75, 2.2] GeV/c^2 , while the $\Lambda_c^+ \rightarrow pK^-\pi^+$ is reconstructed within [2.15, 2.40] GeV/c^2 . Finally, the reconstructed charm signals are combined with the triggered lepton in a three-dimensional kinematic fit constraining all tracks to a common vertex (see Fig. 1) to establish signals that can be related to semileptonic B^- , \bar{B}^0 , \bar{B}_s^0 , and Λ_b^0 decays. The $\phi \rightarrow K^+K^-$ vertex reconstruction does not use a constraint to the known ϕ mass [42], although $|m(\phi) - 1.019|$ [GeV/c^2] is required in order to select a pure sample of ϕ candidates.

3. Backgrounds to Lepton-Charm Signals

Several backgrounds affect the semileptonic \bar{B} signals. Some of these can be reduced by judicious signal selection, while some must be included in the modeling of the signal or treated as sources of systematic uncertainties. The simplest of these backgrounds to understand are those events arising from combinatoric sources, which are generally estimated from the sidebands of the charm signal. In these backgrounds, random tracks are combined to form a charm signal which passes all charm selection requirements. This combinatoric background can most easily be reduced by selection requirements and modeled by the sideband events, which are expected to exhibit the same shape underneath the signal. A related, but more subtle type of background is that arising from the mis-identification of tracks in one charm decay arising from incorrect assignment of particle identifications in a real charm decay, resulting in "reflection" backgrounds. These backgrounds are often flat beneath the signal of interest, but occasionally they exhibit particular shapes that can affect the signal distribution non-uniformly. Some reflection backgrounds can be effectively reduced with particle identification selections, such as the specific ionization of particles, dE/dx (see Section II C 4.) Other reflection backgrounds, which have non-uniform distribution in mass beneath the charm signal are included in the fit to the signal (see Section II C 5.) MC simulated data is used to determine the shape of these reflection backgrounds.

The third type of background to the semileptonic signals arises from physical processes that produce a real lepton and charm hadron, but not through a decay directly to ℓ^-D . This includes processes which originate from the same \bar{B} , such as $\bar{B} \rightarrow D\bar{D}$, where $\bar{D} \rightarrow \ell^-X$, and $\bar{B} \rightarrow \tau^-\bar{\nu}_\tau D$, where $\tau^- \rightarrow \ell^-X$. These "physics backgrounds" are included in the fit to the sample composition (see Section III). Other backgrounds include processes in which the lepton and charm hadron originate from separate $b\bar{b}$ and $c\bar{c}$ quark pairs, *i.e.* $b \rightarrow DX$, $\bar{b} \rightarrow \ell^+X$, or $c \rightarrow DX$, $\bar{c} \rightarrow \ell^-X$. The $b\bar{b}$ background gives a wrong sign (WS) lepton-charm combination, in which the charm and lepton have the same charge, while the $c\bar{c}$ background gives right sign (RS) lepton-charm combinations, in which the charm and lepton have opposite charge. All of these processes are also possible with a real charm hadron and a false lepton. In the case of false leptons, both right sign and wrong sign lepton-charm

are expected to be present. Backgrounds which do not originate from the same \bar{B} hadron are treated as a source of systematic uncertainty and described by the wrong sign lepton-charm events, which primarily describe false leptons (see Section VI A.) The $c\bar{c}$ background is assumed to be small for a charm decaying to a lepton with $p_T > 4 \text{ GeV}/c$ [43] and is ignored, while the $b\bar{b}$ background is implicitly included in the false lepton systematic uncertainty.

4. Signal Optimization

Requirements to further enhance the lepton-charm signal include p_T cuts on the p , K , and π charm daughter tracks, and cuts on the invariant mass of the lepton-charm system, $m(\ell^- D) \equiv \sqrt{(p^\mu(\ell^-) + p'^\mu(D))^2}$, to limit feed-down from excited charm and lepton-charm combinations which do not originate from direct semileptonic bottom hadron decays. Requirements are also made on the probability of the charm and lepton-charm vertex fits.

Since bottom hadrons are longer-lived, a powerful discriminant against these backgrounds is a cut on the proper time of $\ell^- D$ candidate. The decay distance of the \bar{B} hadron is determined by defining a quantity, $L_{xy}(\text{PV} \rightarrow \ell^- D)$, which is the transverse decay distance of the lepton-charm combination from the primary interaction vertex (PV), projected on the $\ell^- D$ momentum direction. The missing neutrino produced in the semileptonic decay prevents precise knowledge of $p_T(\bar{B})$ and thus of the proper decay time of the \bar{B} candidate. Instead, a pseudo proper decay time is constructed as:

$$ct^*(\ell^- D) \equiv L_{xy}(\text{PV} \rightarrow \ell^- D) \times \frac{m(\bar{B})}{p_T(\ell^- D)}. \quad (1)$$

A $ct^*(\ell^- D) > 200 \mu\text{m}$ cut is applied to guarantee a signal from long-lived bottom hadrons and to reduce signal contamination from false leptons and other processes that can contribute a lepton and a charm hadron from uncorrelated sources (see also Section II C 3.) This requirement also drastically reduces the combinatoric background of charm candidates with real leptons. A cut on the significance of the transverse decay distance of the charm meson, $L_{xy}(\text{PV} \rightarrow D)/\sigma_{L_{xy}(\text{PV} \rightarrow D)}$, also reduces the light flavored hadron contamination in the signal. A cut on $p_T(D^0) > 5 \text{ GeV}/c$ is applied to improve agreement between the $\ell^- D^0$ data and Monte Carlo simulation used in determining the efficiencies (see Sec. IV). The selected D^{*+} candidates are a subset of the D^0 candidates. Instead of performing a vertex fit on the soft pion, π_*^+ , from the $D^{*+} \rightarrow D^0 \pi_*^+$ decay, A tight $\Delta m(D^{*+}, D^0) \equiv m(D^0 \pi^+) - m(D^0) \in [0.1440, 0.1475] \text{ GeV}/c^2$ cut is used to select a very clean $\ell^- D^{*+}$ sample. This reduces the systematic uncertainty in the selection of the $\ell^- D^{*+}$ combination relative to a $\ell^- D^0$ pair, since no additional vertex fit is performed. Consequently, the efficiency to detect the soft pion is better described by the simulation. Since the data agrees well with the simulation for tracks with p_T greater than $400 \text{ MeV}/c$, as can be seen in Fig. 2, the soft pion efficiency is determined from the simulation. A tight $\Delta m(D^{*+}, D^0) \in [0.1440, 0.1475] \text{ GeV}/c^2$ cut is used to select a very clean $\ell^- D^{*+}$ sample.

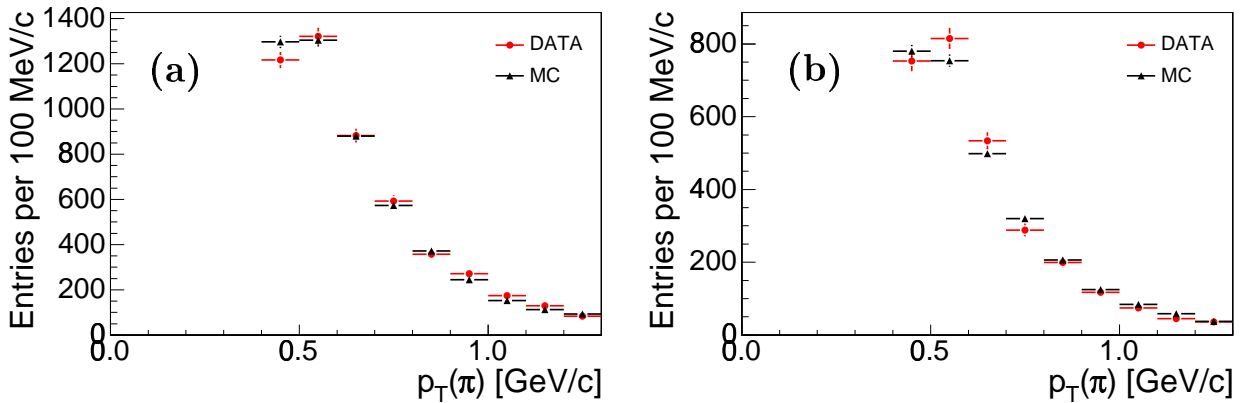


FIG. 2: Comparisons between data and simulation of $p_T(\pi_*^+)$, the soft pion from the D^{*+} decay, for the (a) $\mu^- D^{*+}$ and (b) $e^- D^{*+}$ mode.

In order to determine the final analysis selection, kinematic selection criteria are optimized with respect to the combinatoric background for each lepton-charm channel, with additional cuts designed to limit non-combinatoric background, such as the $ct^*(\ell^- D)$ and $p_T(D)$ cuts, applied during the optimization. The figure of merit (FOM) used for optimization is $S/\sqrt{S+B}$. The signal, S , is taken from inclusive $\bar{B} \rightarrow \ell^- \bar{\nu}_\ell DX$ and $\Lambda_b^0 \rightarrow \ell^- \bar{\nu}_\ell \Lambda_c^+ X$ Monte Carlo (see Sec. IV A). The background, B , is taken from the sidebands of the charm signal. In order for the FOM to accurately reflect the significance of the signals in data, S is scaled to the expected data signal with a set of nominal cuts obtained by first optimizing each cut individually without applying any other cut. The cuts are then optimized a second time applying all optimal cuts from the prior optimization except the cut being optimized. After two or three successive iterations, a stable optimal cut point is reached for all cuts.

A particle identification cut using dE/dx is found useful for reducing the combinatoric background in the Λ_c^+ signal. The combinatoric background can be significantly reduced by correctly identifying the proton from the $\Lambda_c^+ \rightarrow p K^- \pi^+$ decay utilizing the specific energy loss of the proton track measured in the COT. A dE/dx likelihood ratio, \mathcal{LR} , requirement is applied to the proton. The likelihood ratio is defined by the relation $\mathcal{LR}(p) \equiv \mathcal{L}(p)/[\mathcal{L}(p) + \mathcal{L}(K) + \mathcal{L}(\pi) + \mathcal{L}(e) + \mathcal{L}(\mu)]$, where $\mathcal{L}(i) \propto \exp\{-Z_i^2/(2\sigma_{Z_i}^2)\}$ and $Z_i \equiv \ln[dE/dx_i^{\text{meas}}/dE/dx_i^{\text{pred}}]$. Figure 3 shows the resulting \mathcal{LR} distributions for protons from the $\Lambda^0 \rightarrow p \pi^-$ decay and kaons and pions from the $D^{*+} \rightarrow D^0 (\rightarrow K^- \pi^+) \pi^+$ decay with the proton hypothesis applied. Muons are indistinguishable from pions, while electrons are well-separated from all of the other distributions, since their mass is so much lower than the mass of the other particles. A cut on $\mathcal{LR}(p) > 0.3$, as determined from the control samples, is applied to reduce background while keeping the proton efficiency high. This cut primarily removes pions, since the dE/dx separation between protons and kaons is not as good.

To cancel as many differences in signal reconstruction as possible, the selection criteria

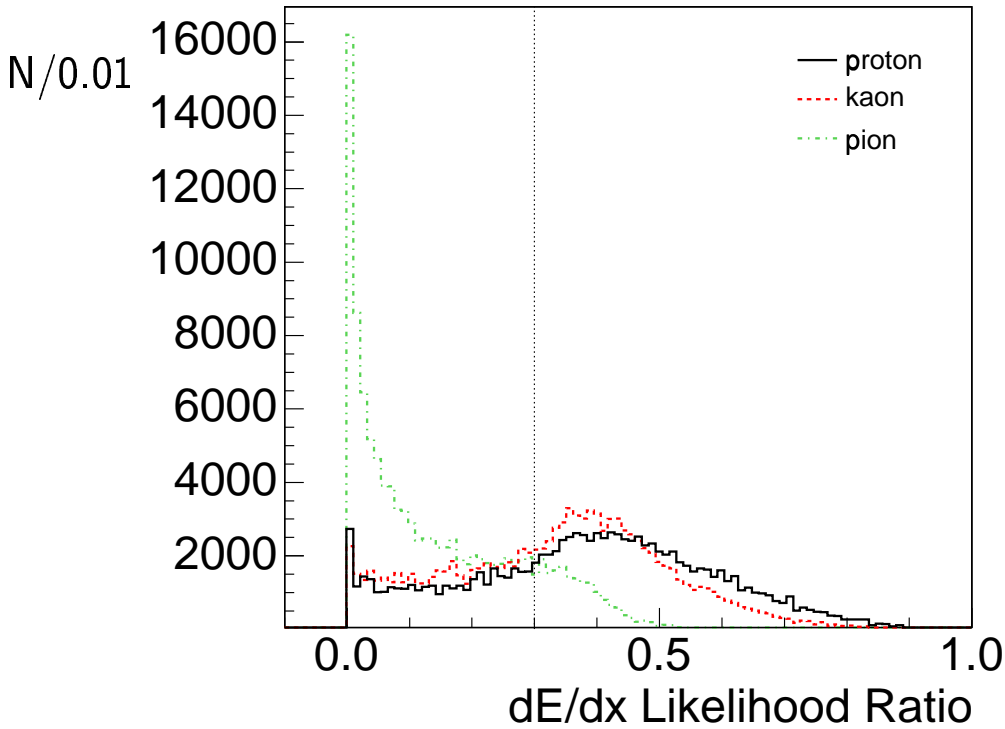


FIG. 3: $dE/dx \mathcal{LR}$ distribution for protons from $\Lambda^0 \rightarrow p\pi^-$ and kaons and pions from $D^{*+} \rightarrow D^0(\rightarrow K^-\pi^+)\pi^+$ with the proton hypothesis applied. Tracks with \mathcal{LR} to the right of the dashed vertical line are identified as protons.

are kept as similar as is feasible across charm channels. The optimized cuts designed to limit both the combinatoric and some non-combinatoric backgrounds are unified to minimize the differences in selections between channels. However, some cuts, in which different optimal values are expected due to differences in the decay kinematics, are not forced to be similar. For example, the proper decay time of the D^+ meson and Λ_c^+ baryon differ by a factor of about five. The selection criteria applied to the lepton-charm decay signatures are listed in Table I. Additional selection requirements to reduce non-combinatoric backgrounds are discussed next.

5. Reflection Backgrounds

The selection criteria discussed above (see Sec. II C 4) optimize the signal sensitivity with respect to the combinatoric background. However, there are other non-combinatoric backgrounds that must be considered. This is partially achieved with the $ct^*(\ell^-D)$ and $p_T(D)$ cuts discussed previously. Another significant background arises from reflections, which oc-

TABLE I: Signal selection requirements.

Selection cuts	$\ell^- D^0$	$\ell^- D^{*+}$	$\ell^- D^+$	$\ell^- D_s^+$	$\ell^- \Lambda_c^+$
$ct(D)$ [cm] \in	[-0.01,0.10]	[-0.01,0.10]	[-0.01,0.20]	[-0.01,0.10]	[-0.01,0.05]
$ct^*(\ell^- D)$ [cm] $>$	0.02	0.02	0.02	0.02	0.02
$\sigma_{ct^*}(\ell^- D)$ [cm] $<$	0.04	0.04	0.04	0.04	0.04
$m(\ell^- D)$ [GeV/c 2] \in	[2.4,5.1]	[2.4,5.1]	[2.4,5.1]	[2.4,5.1]	[3.4,5.5]
$p_T(D)$ [GeV/c] $>$	5.0	5.0	N/A	N/A	N/A
$p_T(p)$ [GeV/c] $>$	N/A	N/A	N/A	N/A	2.0
$p_T(K)$ [GeV/c] $>$	0.6	0.6	0.6	0.6	0.6
$\chi^2_{2D}(D) <$	10	10	10	10	5
vertex prob.($\ell^- D$) $>$	10^{-7}	10^{-7}	10^{-7}	10^{-7}	10^{-4}
$L_{xy}/\sigma_{Lxy}(D) >$	4.5	4.5	11	5	4.5
$\Delta m(D^{*+}, D^0)$ [GeV/c 2] \in	N/A	[0.1440,0.1475]	N/A	N/A	N/A
$p_T(\pi_*)$ [GeV/c] $>$	N/A	0.4	N/A	N/A	N/A
$ m(\phi) - 1.019 $ [GeV/c 2] $<$	N/A	N/A	N/A	0.0095	N/A
$dE/dx \mathcal{LR}(p)$ $>$	N/A	N/A	N/A	N/A	0.3

cur when the particle identifications in charm decay are mis-assigned. For example, if the K^+ from a $D_s^+ \rightarrow K^+K^-\pi^+$ decay is assigned the pion mass, the $\pi^+K^-\pi^+$ combination can contribute to the D^+ signal. Figure 4 shows the shapes determined from MC for reflections from (a) D^0 , (b) D^{*+} , (c) D^+ , (d) D_s^+ , and (e) Λ_c^+ decays when these decay channels are reconstructed as a different charm mode. The shapes are normalized to their expected contributions, *e.g.* assuming $f_u : f_d : f_s : f_{\Lambda_b} = 0.4 : 0.4 : 0.1 : 0.1$, where these numerical values are for illustrative purposes only. The $D_s^+ \rightarrow K^+K^-\pi^+$ decay is the most significant reflection background below the D^+ signal, shown in Fig. 4(c). This reflection is particularly problematic because the D_s^+ reflection begins just underneath the real D^+ signal. Potential $p\text{-}\pi$ mis-identification is a significant consideration in the Λ_c^+ signal, shown in Fig. 4(e). The $D^+ \rightarrow K^-\pi^+\pi^+$ decay significantly contributes to the background beneath the Λ_c^+ signal, although its contribution is flat underneath the signal.

The shape of the $D_s^+ \rightarrow K^+K^-\pi^+$ reflection background beneath the $D^+ \rightarrow K^-\pi^+\pi^+$ signal is determined from a Monte Carlo simulation (see Section IV A) study, in which semileptonic $\bar{B}_s^0 \rightarrow \ell^-\bar{\nu}_\ell D_s^+ X$ decays are generated. In these MC events $D^+ \rightarrow K^-\pi^+\pi^+$ candidates are then reconstructed. The resulting $K^-\pi^+\pi^+$ invariant mass distribution is shown in Fig. 5. The normalization of the $D_s^+ \rightarrow K^+K^-\pi^+$ reflection shape in the fit to the D^+ signal is determined by reconstructing a $D_s^+ \rightarrow \phi(\rightarrow K^+K^-)\pi^+$ signal from the wide signal window, $1.78 \text{ GeV}/c^2 \leq m(D^+ \rightarrow K^-\pi^+\pi^+) \leq 1.95 \text{ GeV}/c^2$, shown in Fig. 6. A mass cut of $|m(K^+K^-) - 1.019 \text{ GeV}/c^2| < 0.0095 \text{ GeV}/c^2$, designed to reduce background to the D_s^+ signal, is applied to the $\phi \rightarrow K^+K^-$ decay. Monte Carlo simulation is then

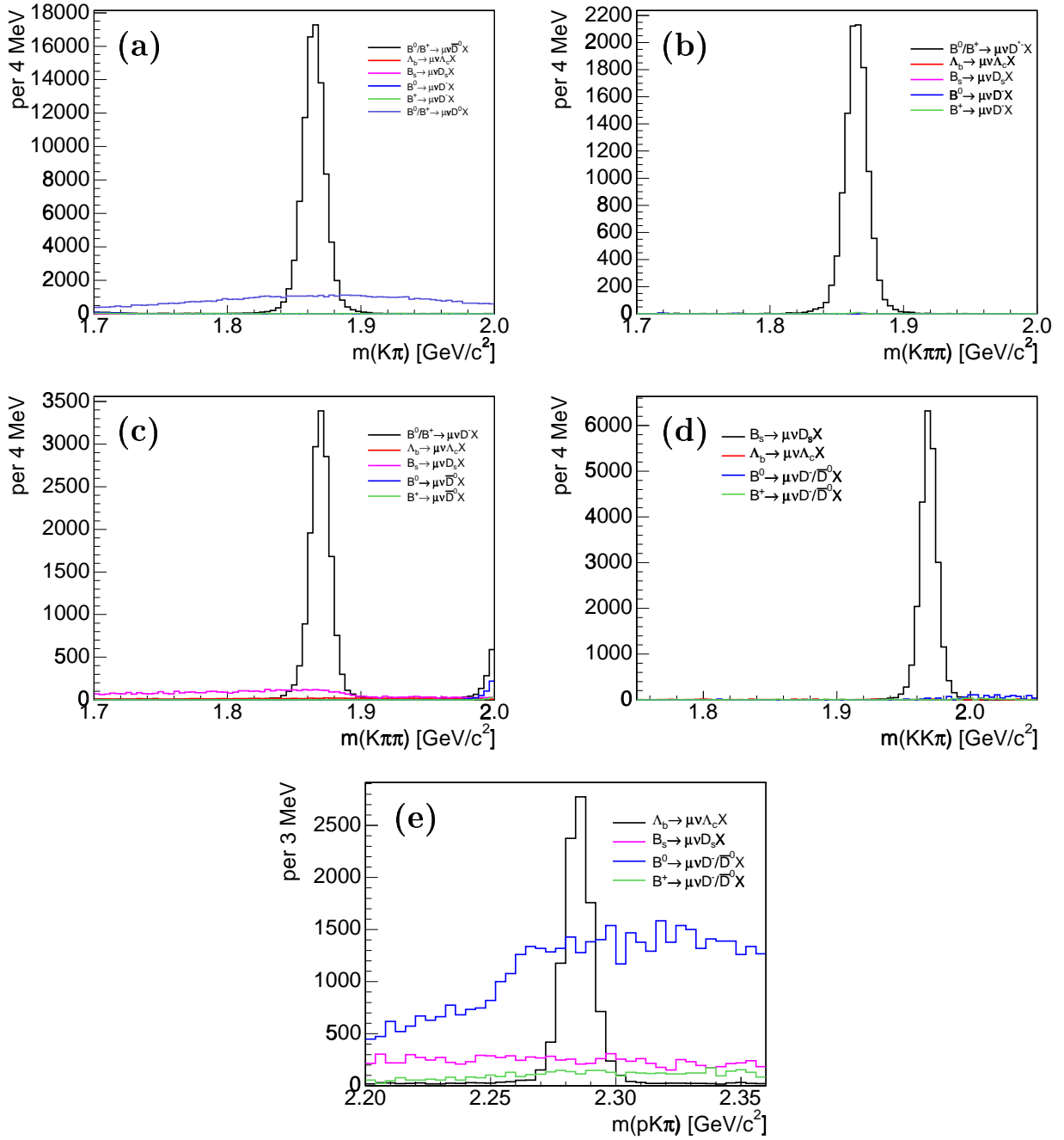


FIG. 4: Monte Carlo simulation reflection shapes for (a) D^0 , (b) D^{*+} , (c) D^+ , (d) D_s^+ , and (e) Λ_b^+ . The shapes are normalized to their expected contributions, assuming $f_u : f_d : f_s : f_{\Lambda_b} = 0.4 : 0.4 : 0.1 : 0.1$, used for illustrative purposes only.

used to measure the efficiency of the $D_s^+ \rightarrow \phi\pi^+$ decay relative to the inclusive set of $D_s^+ \rightarrow K^+K^-\pi^+$ decays that contribute to the reflection. The converse $D^+ \rightarrow K^-\pi^+\pi^+$ reflection in the $D_s^+ \rightarrow K^+K^-\pi^+$ signal is negligible due to the ϕ mass cut applied to the K^+K^- invariant mass.

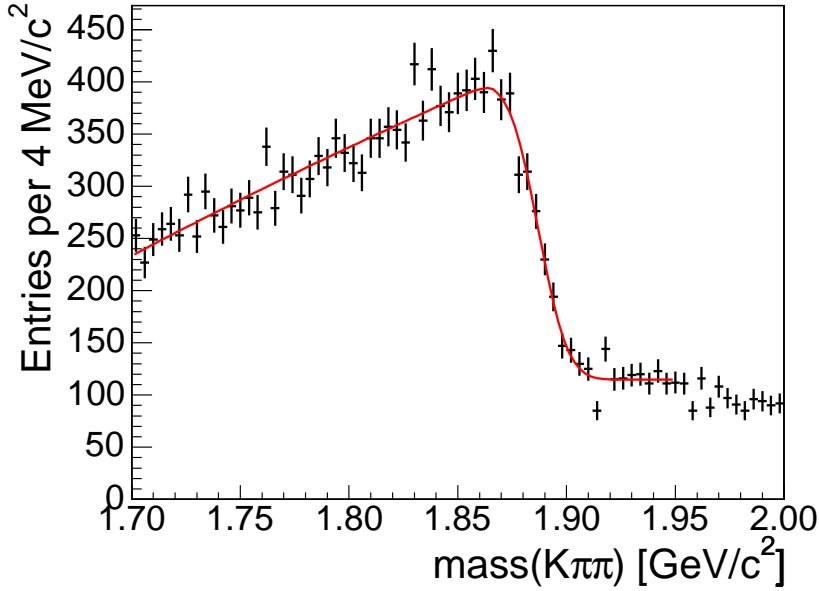


FIG. 5: Combined $D_s^+ e^-$ and $D_s^+ \mu^-$ reflection into the $K^+ \pi^- \pi^-$ invariant mass. The reflection is determined from an inclusive MC sample of $\bar{B}_s^0 \rightarrow \ell^- \bar{\nu}_\ell D_s^+ X$, where all D_s^+ meson decay modes are included.

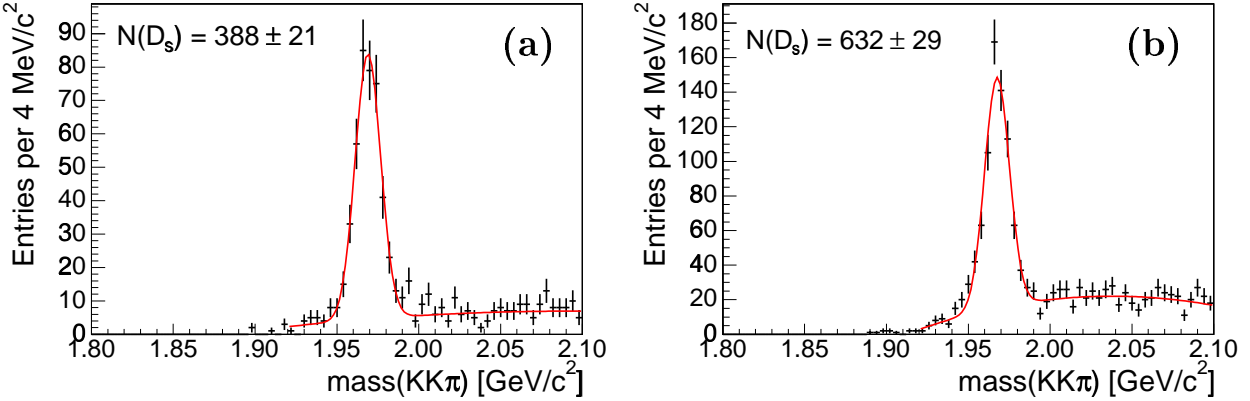


FIG. 6: $N(D_s^+ \rightarrow \phi \pi^+)$ reconstructed in $m(K\pi\pi) \in [1.78, 1.95]$ in the (a) $e+$ SVT and (b) $\mu+$ SVT data.

In a manner completely analogous to the way the D_s^+ signal yield, $N_{\text{data}}(D_s^+ \rightarrow \phi \pi^+)$, is determined in data, the D_s^+ candidates decaying to the $\phi \pi^+$ and $K^- K^+ \pi^+$ states, $N_{MC}(D_s^+ \rightarrow \phi \pi^+)$ and $N_{MC}(D_s^+ \rightarrow K^+ K^- \pi^+)$, respectively, are determined from the Monte Carlo simulation. The number of D_s^+ mesons expected to contribute to the D^+ signal can then be calculated by evaluating

$$N_{\text{data}}(D_s^+ \rightarrow K^+ K^- \pi^+) = \frac{N_{\text{data}}(D_s^+ \rightarrow \phi \pi^+)}{R_{\phi\pi}}, \quad (2)$$

where

$$R_{\phi\pi} \equiv \frac{N_{MC}(D_s^+ \rightarrow \phi\pi^+)}{N_{MC}(D_s^+ \rightarrow K^+K^-\pi^+)} = 0.246 \pm 0.016. \quad (3)$$

The numbers of D_s^+ candidates that contribute to the D^+ lepton-charm samples in the wide mass window around the D^+ signal are $N_e(D_s^+ \rightarrow K^+K^-\pi^+) = 1580 \pm 130$ and $N_\mu(D_s^+ \rightarrow K^+K^-\pi^+) = 2570 \pm 210$. The normalization of the D_s^+ reflection in the D^+ signal is later constrained to the predicted number of D_s^+ reflection events in the fit to the D^+ signal (see Sec. IID).

Since the D^+ and D_s^+ reflections in the Λ_c^+ signal are relatively flat under the signal region, sideband subtraction is expected to remove the effect of the D^+ and D_s^+ reflections on the Λ_c^+ signal distributions within statistical uncertainty. Correspondingly, the event count obtained by fitting the Λ_c^+ signal is not expected to be significantly influenced by the presence of these backgrounds. Additionally, the dE/dx cut applied to the proton (discussed in the previous section) reduces contamination from pions, which contribute to the $D^+ \rightarrow K^-\pi^+\pi^+$ and $D^{*+} \rightarrow [K^-\pi^+]\pi^+$ reflections.

D. Signal Yields

The $m(K^-\pi^+\pi^+)$, $m(K^-pi^+)$, $m(K^+K^-pi^+)$, and $m(pK^-pi^+)$ mass spectra are fit to determine the number of lepton-charm events for the ℓ^-D^+ , ℓ^-D^0 , ℓ^-D^{*+} , $\ell^-D_s^+$, and $\ell^-\Lambda_c^+$ samples. The invariant mass distributions of the charm signals are shown in Fig. 7 for the μ +SVT data and in Fig. 8 for the e +SVT data with all lepton, charm, and lepton-charm selection criteria applied. The distributions are fit with a double Gaussian and linear background shape. The reflection of D_s^+ decays into the D^+ final state is included in the fit to the D^+ signal. The normalization of the D_s^+ reflection is constrained to the predicted number of D_s^+ reflection events as described above. In order to keep the broad Gaussian and reflection shapes reasonably independent, the double Gaussian means and widths for the D^+ are determined before the reflection shape is added to the fit. When the combined fit is performed, the parameters of the double Gaussian are constrained within their uncertainties. The fits to the D^0 , D^{*+} , D^+ , D_s^+ , and Λ_c^+ charm signals for right sign lepton-charm pairs are shown in Fig. 7 for the μ +SVT data and in Fig. 8 for the e +SVT data. The invariant mass distributions for wrong sign combinations of lepton-charm pairs, *e.g.* $D^+\ell^+$, are also included in Figs. 7 and 8, indicating no significant contributions of possible backgrounds, such as false leptons, to be present in the right sign signals (see also Sec. VIA). The fitted lepton-charm yields are listed in Table II. The D_s^+ reflection is not included in the D^+ yield, since the fit shape to the D^+ includes a separate shape for the D_s^+ reflection, as discussed in Section IIC5. The dE/dx cut flattens the background and reduces its overall level by a factor of five, while it reduces the signal by $\sim 35\%$ in the μ +SVT data and $\sim 28\%$ in the e +SVT data as can be seen in Fig. 7(e)-(f) and Fig. 8(e)-(f).

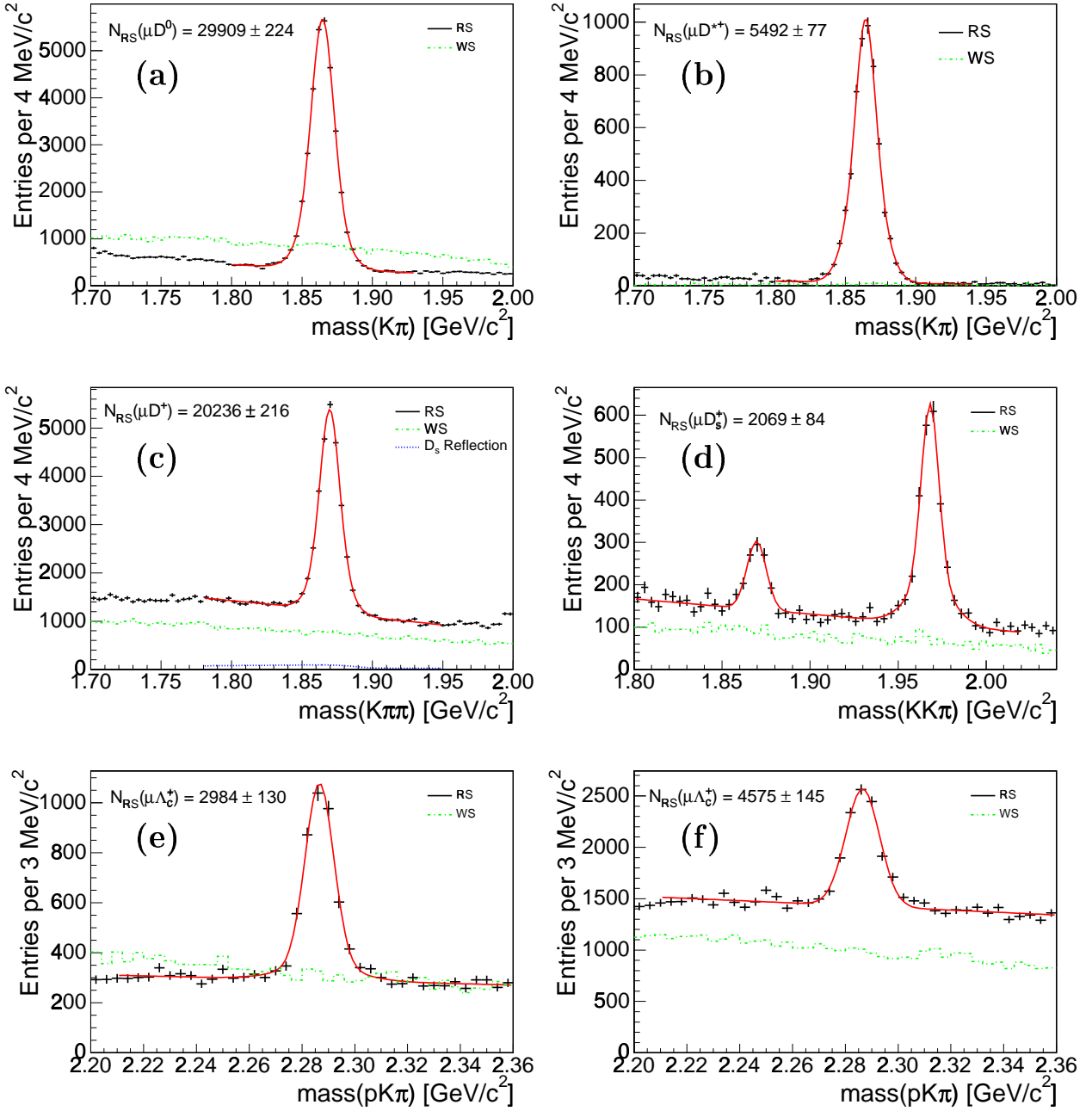


FIG. 7: μ +SVT right sign (RS) (points with error bars) and wrong sign (WS) (histogram) invariant mass distribution of (a) D^0 , (b) D^{*+} , (c) D^+ , (d) D_s^+ , (e) Λ_c^+ with all cuts applied and (f) without the dE/dx cut applied. The fit parameterizations described in the text are overlaid.

III. SAMPLE COMPOSITION DETERMINATION PROCEDURE

This measurement uses flavor SU(3) symmetry to describe the branching fractions of semileptonic \bar{B} meson decays; therefore, the partial widths of the semileptonic decays of

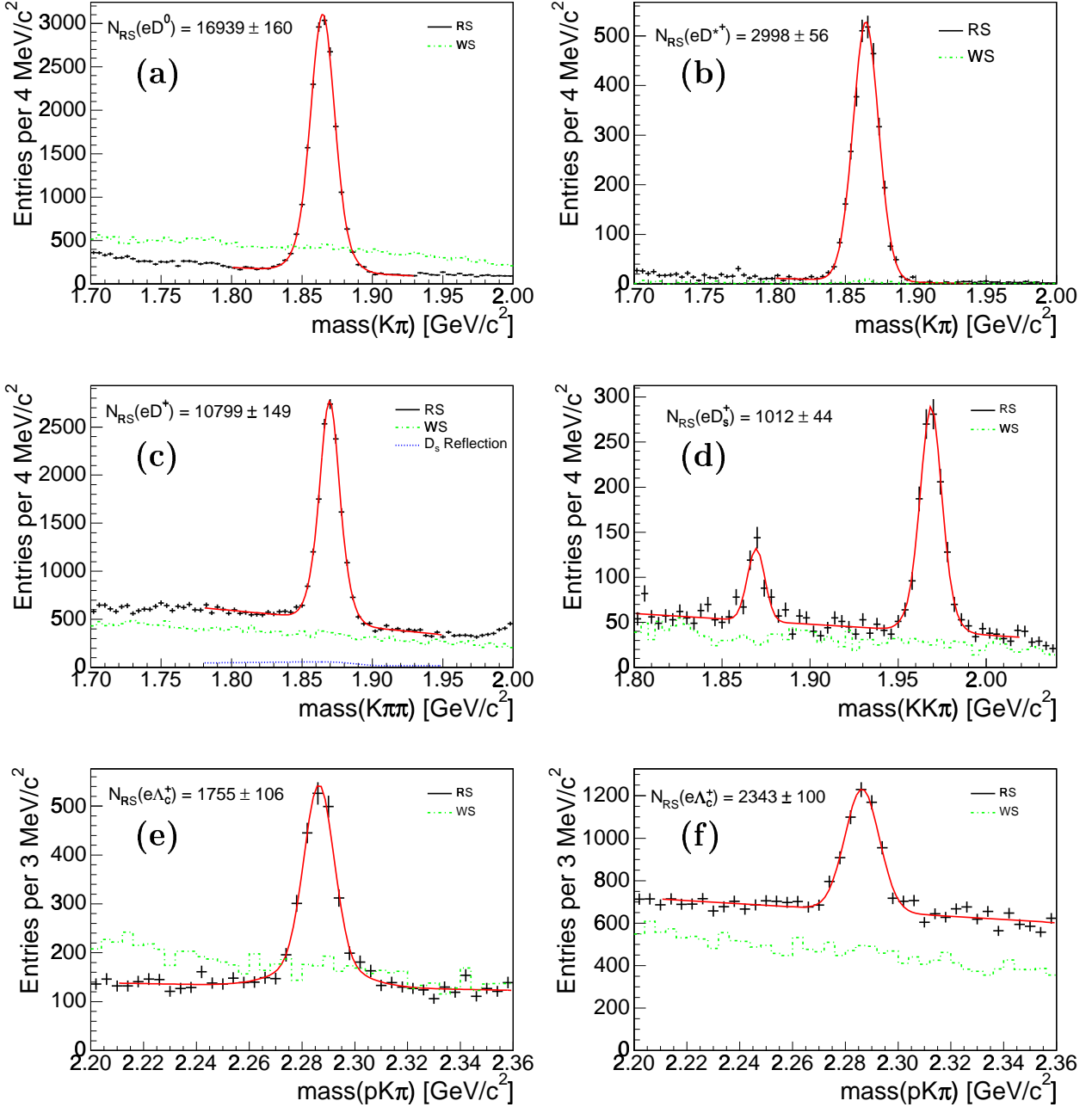


FIG. 8: $e+$ SVT right sign (RS) (points with error bars) and wrong sign (WS) (histogram) invariant mass distribution of (a) D^0 , (b) D^{*+} , (c) D^+ , (d) D_s^+ , (e) Λ_c^+ with all cuts applied and (f) without the dE/dx cut applied. The fit parameterizations described in the text are overlaid.

\bar{B} mesons are chosen to be equal, namely

$$\Gamma(\bar{B}^0 \rightarrow \ell^- \bar{\nu}_\ell X) = \Gamma(B^- \rightarrow \ell^- \bar{\nu}_\ell X) = \Gamma(\bar{B}_s^0 \rightarrow \ell^- \bar{\nu}_\ell X), \quad (4)$$

TABLE II: Fitted signal yields for lepton-charm final states in 360 pb^{-1} .

Decay	$e+\text{SVT}$			$\mu+\text{SVT}$		
	Yield	FOM	Fit Prob. [%]	Yield	FOM	Fit Prob. [%]
$\ell^- D^0$	$16,939 \pm 160$	122	64.4	$29,909 \pm 224$	159	12.5
$\ell^- D^{*+}$	$2,998 \pm 56$	54.1	1.27	$5,492 \pm 77$	73.3	1.14
$\ell^- D^+$	$10,779 \pm 149$	90.2	9.43	$20,236 \pm 216$	114	50.7
$\ell^- D_s^+$	$1,012 \pm 44$	27.3	7.84	$2,069 \pm 84$	36.6	30.2
$\ell^- \Lambda_c^+$	$1,755 \pm 106$	32.8	33.9	$2,984 \pm 130$	40.9	40.9

where

$$\Gamma(\bar{B} \rightarrow \ell^- \bar{\nu}_\ell X) = \frac{1}{\tau(\bar{B})} \mathcal{B}(\bar{B} \rightarrow \ell^- \bar{\nu}_\ell X). \quad (5)$$

This assumption is referred to as the spectator model, which also implies that the partial widths of the semileptonic bottom hadron decays into the pseudoscalar, vector, or higher excited D states are expected to be equal,

$$\Gamma(\bar{B}^0 \rightarrow \ell^- \bar{\nu}_\ell D^+) = \Gamma(B^- \rightarrow \ell^- \bar{\nu}_\ell D^0) = \Gamma(\bar{B}_s^0 \rightarrow \ell^- \bar{\nu}_\ell D_s^+) = \Gamma(\bar{B} \rightarrow \ell^- \bar{\nu}_\ell D), \quad (6)$$

with similar relations holding for D^* and D^{**} decays. The additional constraint that

$$\Gamma(\bar{B} \rightarrow \ell^- \bar{\nu}_\ell D) + \Gamma^*(\bar{B} \rightarrow \ell^- \bar{\nu}_\ell D^*) + \Gamma^{**}(\bar{B} \rightarrow \ell^- \bar{\nu}_\ell D^{**}) = \Gamma(\bar{B} \rightarrow \ell^- \bar{\nu}_\ell X), \quad (7)$$

is also applied to the partial widths. This constraint includes non-resonant decays and $b \rightarrow u$ transitions in addition to actual D^{**} decays in the D^{**} partial width. Since excited Λ_b^0 semileptonic decays are not necessarily well-described by the spectator model, fixed branching fractions are used to describe those decays [44] (see Table VI).

A simplified example illustrating the procedure used to extract the sample composition follows. Assuming that the only source of $\ell^- D^+$ combinations is from the direct decay of a neutral \bar{B} meson, such as $\bar{B}^0 \rightarrow \ell^- \bar{\nu}_\ell D^+$, the number of reconstructed $\ell^- D^+$ events can be expressed as

$$\begin{aligned} N(\ell^- D^+) &= N(\bar{B}^0) \times \mathcal{B}(\bar{B}^0 \rightarrow \ell^- \bar{\nu}_\ell D^+) \times \mathcal{B}(D^+ \rightarrow K^- \pi^+ \pi^+) \\ &\quad \times \varepsilon(\bar{B}^0 \rightarrow \ell^- \bar{\nu}_\ell D^+, D^+ \rightarrow K^- \pi^+ \pi^+) \\ &= [N(\bar{B}) \cdot f_d] \times [\tau(\bar{B}^0) \cdot \Gamma(\bar{B}^0 \rightarrow \ell^- \bar{\nu}_\ell D^+)] \times \mathcal{B}(D^+ \rightarrow K^- \pi^+ \pi^+) \\ &\quad \times \varepsilon(\bar{B}^0 \rightarrow \ell^- \bar{\nu}_\ell D^+, D^+ \rightarrow K^- \pi^+ \pi^+). \end{aligned} \quad (8)$$

The number of reconstructed $\ell^- D^+$ combinations, $N(\ell^- D^+)$, can be related to the number of \bar{B}^0 mesons, $N(\bar{B}^0)$, produced in the fragmentation process by the branching fraction of the $\bar{B}^0 \rightarrow \ell^- \bar{\nu}_\ell D^+$ decay, the branching fraction of the $D^+ \rightarrow K^- \pi^+ \pi^+$ charm decay, and

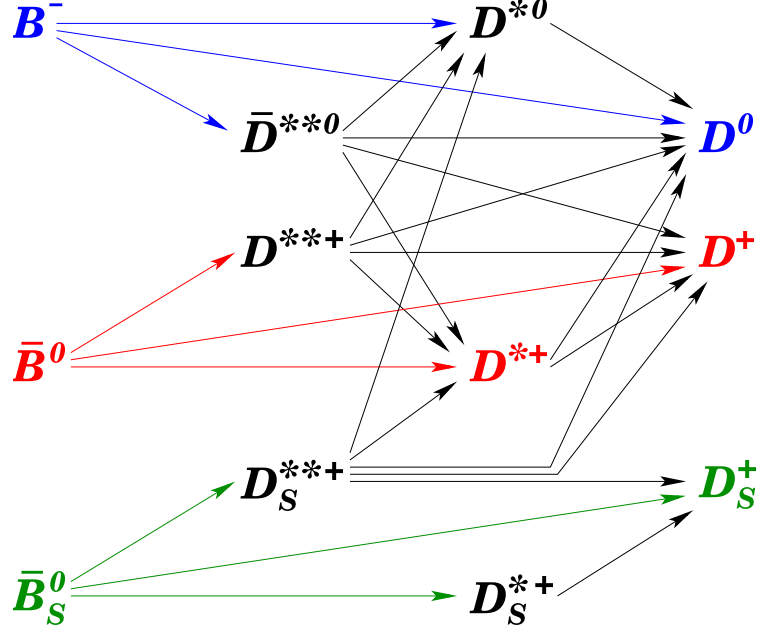


FIG. 9: Illustration of cross talk between B -meson species.

the detection and reconstruction efficiencies for the entire decay chain. $N(\bar{B}^0)$ and $N(\bar{B})$ represent the number of \bar{B}^0 and generic bottom hadrons produced, respectively.

However, as sketched in Fig. 9, cross-talk between the various bottom hadron species via the excited charm states necessitates a sample composition parameterization to relate the lepton-charm signals to the parent bottom hadrons. Introducing the relative fragmentation fractions, the sample composition for the \bar{B}^0 can be written (for illustrative purposes) as:

$$\begin{aligned}
 N(\ell^- D^+) = & N(\bar{B}^0) \times \mathcal{B}(D^+ \rightarrow K^-\pi^+\pi^+) \\
 & \times \left[\sum_{\bar{B}^0 \rightarrow D^+ X} \mathcal{B}(\bar{B}^0 \rightarrow \ell^-\bar{\nu}_\ell D^+ X) \varepsilon(\bar{B}^0 \rightarrow \ell^-\bar{\nu}_\ell D^+ X) \right. \\
 & + \frac{f_u}{f_d} \sum_{B^- \rightarrow D^+ X} \mathcal{B}(B^- \rightarrow \ell^-\bar{\nu}_\ell D^+ X) \varepsilon(B^- \rightarrow \ell^-\bar{\nu}_\ell D^+ X) \\
 & \left. + \frac{f_s}{f_u + f_d} \left(1 + \frac{f_u}{f_d} \right) \sum_{\bar{B}_s^0 \rightarrow D^+ X} \mathcal{B}(\bar{B}_s^0 \rightarrow \ell^-\bar{\nu}_\ell D^+ X) \varepsilon(\bar{B}_s^0 \rightarrow \ell^-\bar{\nu}_\ell D^+ X) \right]. \quad (9)
 \end{aligned}$$

The sample composition parameterization requires knowledge of the branching fractions of the charm hadrons, which are determined from the world average values as compiled by the Particle Data Group (PDG) [42], when available, and from theoretical predictions and symmetry principles [45], when not available in the PDG. The parameterization also requires knowledge of the efficiency of reconstructing the decay, which is primarily determined from Monte Carlo simulations. In addition to the primary decays that contribute to the semileptonic signal, indirect semileptonic decays (*e.g.* $\bar{B} \rightarrow D\bar{D}X$, $\bar{D} \rightarrow \ell^-X$) contributing

to the $\ell^- D$ final state are also included in the parameterization of the sample composition. All of the decays considered in the bottom hadron sample composition procedure are listed in Table III (see also Fig. 9).

The bottom meson branching fractions are included via the partial widths, listed in Table IV, and adjusted by the lifetime of the respective bottom hadron, given in Table V. The branching fractions used for the Λ_b^0 semileptonic decays are estimated from measurements of the branching fractions made in other CDF measurements [44], as shown in Table VI. The ground state charm branching fractions used in this measurement are listed in Table VII.

IV. EFFICIENCIES

Since the bottom hadron fragmentation fractions are measured relative to each other, most efficiencies in the measurements are expected to cancel. Many of the remaining relative efficiencies are determined from Monte Carlo simulated data in which the trigger and all detector calibrations are configured just as they are determined for a given run in real data. Comparisons between the data and the inclusive simulation samples, discussed in the subsequent section, validate the use of simulation to estimate the relative efficiencies between \bar{B} semileptonic decays and the lepton-charm signals. A few absolute efficiencies, such as the different XFT trigger efficiencies for K , π , and p are not properly described in the Monte Carlo simulation. These efficiencies must be determined from data and are discussed in Section IV B.

A. Monte Carlo Simulation

Monte Carlo simulation is used at various points throughout the measurement. Although the simulation utilized in the sample composition process is generated both for exclusive bottom hadron decays and inclusive \bar{B} semileptonic decays, all of the Monte Carlo simulation samples used in the measurement have the same parameters for generation. The simulated events are passed through the GEANT-based [46, 47] CDF II detector simulation [48]. GEANT 3 simulates the passage of the long-lived particles through the material of the detector and includes multiple scattering effects. All simulated samples are generated with a “realistic”, rather than parametric, simulation. A tuned magnetic field and Geant material description [49] are applied in order to correct for regions of the detector where the material is under-represented in the simulation.

A single bottom hadron is generated according to an input transverse momentum and rapidity spectrum, which have been determined from data. The p_T spectrum, obtained in the inclusive J/ψ cross-section measurement [20], is used as the input \bar{B} meson spectrum. However, it appears that the momentum distributions of the Λ_b^0 decay products, in particular the $\ell^- \Lambda_c^+$ momentum spectrum, are not well described using the same spectrum as is used for

TABLE III: Bottom hadron semileptonic sample composition used in the measurement. NR refers to non-resonant decays.

\bar{B}^0	B^-	\bar{B}_s^0	Λ_b^0
$\ell^- \bar{\nu} D^+$	$\ell^- \bar{\nu} D^0$	$\ell^- \bar{\nu} D_s^+$	$\ell^- \bar{\nu} \Lambda_c^+$
$\ell^- \bar{\nu} D^{*+}$	$\ell^- \bar{\nu} D^{*0}$	$\ell^- \bar{\nu} D_s^{*+}$	$\ell^- \bar{\nu} \Lambda_c(2593)^+$
$\rightarrow D^0 \pi^+$	$\rightarrow D^0 \pi^0 / \gamma$	$\rightarrow D_s^+ \gamma$	$\rightarrow \Sigma_c(2455)^{++} \pi^-$
$D^+ \pi^0 / \gamma$			$\hookrightarrow \Lambda_c^+ \pi^+$
$\ell^- \bar{\nu} D_1^+$	$\ell^- \bar{\nu} D_1^0$	$\ell^- \bar{\nu} D_{s1}^+(2460)$	$\rightarrow \Sigma_c(2455)^0 \pi^+$
$\rightarrow D^{*0} \pi^+$	$\rightarrow D^{*0} \pi^0$	$\rightarrow D_{s0}^{*+} \pi^0$	$\hookrightarrow \Lambda_c^+ \pi^-$
$\hookrightarrow D^0 \pi^0 / \gamma$	$\hookrightarrow D^0 \pi^0 / \gamma$	$\hookrightarrow D_s^+ \pi^0$	$\rightarrow \Sigma_c(2455)^+ \pi^0$
$\rightarrow D^{*+} \pi^0$	$\rightarrow D^{*+} \pi^-$	$\rightarrow D_s^+ \gamma$	$\hookrightarrow \Lambda_c^+ \pi^0$
$\hookrightarrow D^0 \pi^+$	$\hookrightarrow D^0 \pi^+$		$\rightarrow \Lambda_c^+ \pi^- \pi^-$
$D^+ \pi^0 / \gamma$	$D^+ \pi^0 / \gamma$		$\rightarrow \Lambda_c^+ \pi^0 \pi^0$
$\ell^- \bar{\nu} D_0^{*+}$	$\ell^- \bar{\nu} D_0^{*0}$	$\ell^- \bar{\nu} D_{s0}^{*+}(2317)$	$\rightarrow \Lambda_c^+ \gamma$
$\rightarrow D^0 \pi^+$	$\rightarrow D^0 \pi^0$	$\rightarrow D_s^+ \pi^0$	$\ell^- \bar{\nu} \Lambda_c(2625)^+$
$D^+ \pi^0$	$D^+ \pi^-$		$\rightarrow \Lambda_c^+ \pi^+ \pi^-$
$\ell^- \bar{\nu} D_1'^+$	$\ell^- \bar{\nu} D_1'^0$	$\ell^- \bar{\nu} D_{s1}'(2535)$	$\rightarrow \Lambda_c^+ \pi^0 \pi^0$
$\rightarrow D^{*0} \pi^+$	$\rightarrow D^{*0} \pi^0$	$\rightarrow D^{*+} K^0$	$\rightarrow \Lambda_c^+ \gamma$
$\hookrightarrow D^0 \pi^0 / \gamma$	$\hookrightarrow D^0 \pi^0 / \gamma$	$\hookrightarrow D^0 \pi^+$	$\ell^- \bar{\nu} \Sigma_c(2455)^{++} \pi^-$
$\rightarrow D^{*+} \pi^0$	$\rightarrow D^{*+} \pi^-$	$D^+ \pi^0 / \gamma$	$\rightarrow \Lambda_c^+ \pi^+$
$\hookrightarrow D^0 \pi^+$	$\hookrightarrow D^0 \pi^+$	$\rightarrow D^{*0} K^+$	$\ell^- \bar{\nu} \Sigma_c(2455)^0 \pi^+$
$D^+ \pi^0 / \gamma$	$D^+ \pi^0 / \gamma$	$\hookrightarrow D^0 \pi^0 / \gamma$	$\rightarrow \Lambda_c^+ \pi^-$
$\ell^- \bar{\nu} D_2^{*+}$	$\ell^- \bar{\nu} D_2^{*0}$	$\ell^- \bar{\nu} D_{s2}'(2573)$	$\ell^- \bar{\nu} \Sigma_c(2455)^+ \pi^0$
$\rightarrow D^{*0} \pi^+$	$\rightarrow D^{*0} \pi^0$	$\rightarrow D^{*+} K^0$	$\rightarrow \Lambda_c^+ \pi^0$
$\hookrightarrow D^0 \pi^0 / \gamma$	$\hookrightarrow D^0 \pi^0 / \gamma$	$\hookrightarrow D^0 \pi^+$	$\ell^- \bar{\nu} \Lambda_c^+ f_0$
$\rightarrow D^{*+} \pi^0$	$\rightarrow D^{*+} \pi^-$	$D^+ \pi^0 / \gamma$	
$\hookrightarrow D^0 \pi^+$	$\hookrightarrow D^0 \pi^+$	$\rightarrow D^{*0} K^+$	$\ell^- \bar{\nu} \Lambda_c^+ \pi^+ \pi^- (\text{NR})$
$D^+ \pi^0 / \gamma$	$D^+ \pi^0 / \gamma$	$\hookrightarrow D^0 \pi^0 / \gamma$	
$\rightarrow D^0 \pi^0$	$\rightarrow D^0 \pi^0$	$\rightarrow D^+ K^0$	
$\rightarrow D^+ \pi^-$	$\rightarrow D^+ \pi^-$	$\rightarrow D^0 K^+$	
$\ell^- \bar{\nu} D^{*+} \pi^0 (\text{NR})$	$\ell^- \bar{\nu} D^{*+} \pi^- (\text{NR})$	$\ell^- \bar{\nu} D_s^{*+} \pi^0 (\text{NR})$	
$\rightarrow D^0 \pi^+$	$\rightarrow D^0 \pi^+$	$\rightarrow D_s^+ \gamma$	
$D^+ \pi^0 / \gamma$	$D^+ \pi^0 / \gamma$		
$\ell^- \bar{\nu} D^{*0} \pi^+ (\text{NR})$	$\ell^- \bar{\nu} D^{*0} \pi^0 (\text{NR})$	$\ell^- \bar{\nu} D_s^+ \pi^0 (\text{NR})$	
$\rightarrow D^0 \pi^0 / \gamma$	$\rightarrow D^0 \pi^0 / \gamma$		
$\ell^- \bar{\nu} D^+ \pi^0 (\text{NR})$	$\ell^- \bar{\nu} D^+ \pi^- (\text{NR})$		
$\ell^- \bar{\nu} D^0 \pi^+ (\text{NR})$	$\ell^- \bar{\nu} D^0 \pi^0 (\text{NR})$		
$D^{(*)} \bar{D}^{(*)} K$	$D^{(*)} \bar{D}^{(*)} K$	$D^{(*)} \bar{D}^{(*)} K$	
$D^{(*)+} D^{(*)-}$			
$D_s^{(*)} D^{(*)} X$	$D_s^{(*)} D^{(*)} X$	$D_s^{(*)} D^{(*)} X$	$\tau^- \bar{\nu} \Lambda_c^+$
		$D_s^{(*)} D_s^{(*)} X$	$\tau^- \bar{\nu} \Lambda_c(2593)^+$
$\tau^- \bar{\nu} D^{+(*),(**)}$	$\tau^- \bar{\nu} D^{0(*),(**)}$	$\tau^- \bar{\nu} D_s^{+(*),(**)}$	$\tau^- \bar{\nu} \Lambda_c(2625)^+$

TABLE IV: Partial widths of the \bar{B} mesons used (from Ref. [42]).

\bar{B} Decay	Partial Width [ps^{-1}]
$\Gamma(\bar{B} \rightarrow \ell^- \bar{\nu}_\ell D)$	0.0134 ± 0.0009
$\Gamma^*(\bar{B} \rightarrow \ell^- \bar{\nu}_\ell D^*)$	0.0372 ± 0.0017
$\Gamma^{**}(\bar{B} \rightarrow \ell^- \bar{\nu}_\ell D^{**})$	0.0141 ± 0.0010

TABLE V: Bottom hadron lifetimes used in the measurement (from Ref. [42]).

\bar{B} Lifetimes	[ps]
$\tau(\bar{B}^0)$	1.536 ± 0.014
$\tau(B^-)$	1.671 ± 0.018
$\tau(B^-)/\tau(\bar{B}^0)$	1.086 ± 0.017
$\tau(\bar{B}_s^0)$	1.461 ± 0.057
$\tau(\Lambda_b^0)$	1.229 ± 0.080

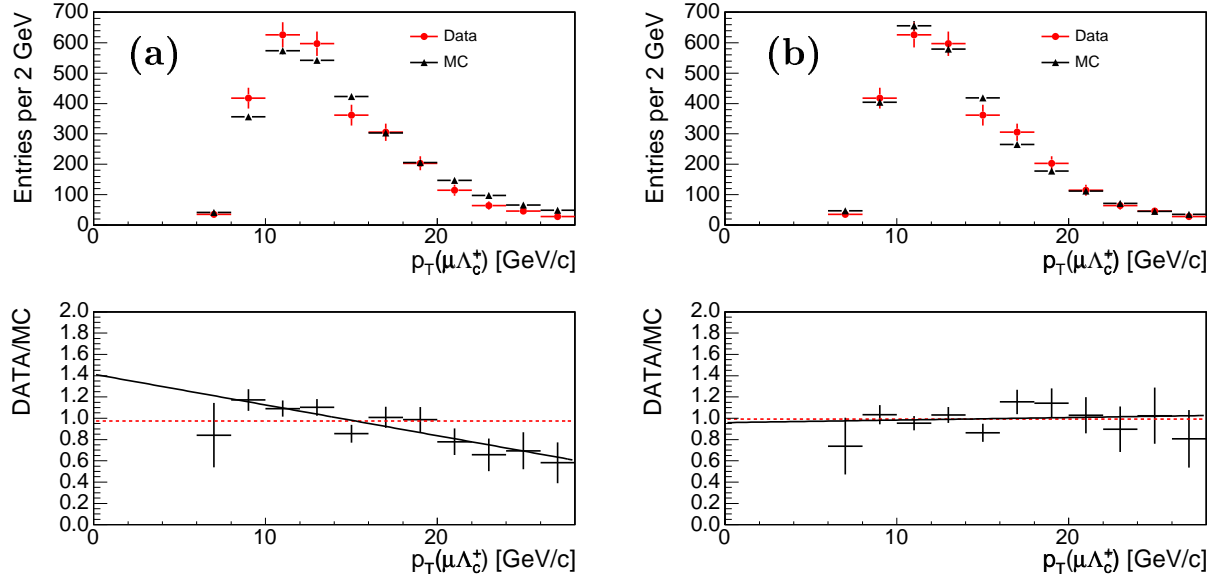
the \bar{B} mesons, as can be seen in Figure 10(a). The Monte Carlo simulation generated $\mu^- \Lambda_c^+$ transverse momentum spectrum is observed to be harder than the measured semileptonic spectrum. This indicates a potential difference in the momentum dependence of b baryon and \bar{B} meson fragmentation processes. Consequently, instead of using the spectrum used for the mesons, a p_T spectrum derived from the semileptonic $\ell^- \Lambda_c^+$ data is used in the measurement. This tuned spectrum [43] shows good agreement between data and Monte Carlo simulation, as shown in Fig. 10(b). The tuned $\ell^- \Lambda_c^+$ spectrum is obtained by re-weighting the bottom

 TABLE VI: Λ_b^0 branching fractions \mathcal{B} used in the measurement (from Ref. [44]). The lack of a quoted uncertainty indicates an assumption made for \mathcal{B} . NR refers to non-resonant decays.

Λ_b^0 Decay	\mathcal{B}
$\ell^- \bar{\nu}_\ell \Lambda_c^+ X$	$(9.2 \pm 2.1)\%$
$\ell^- \bar{\nu}_\ell \Lambda_c^+$	$(6.54 \pm 0.22)\%$
$\ell^- \bar{\nu}_\ell \Lambda_c(2593)^+$	$(3.07 \pm 1.02) \times 10^{-3}$
$\ell^- \bar{\nu}_\ell \Lambda_c(2625)^+$	$(5.14 \pm 0.99) \times 10^{-3}$
$\ell^- \bar{\nu}_\ell \Sigma_c(2455)^{++} \pi^-$	$(2.7 \pm 1.0) \times 10^{-3}$
$\ell^- \bar{\nu}_\ell \Sigma_c(2455)^+ \pi^0$	$(2.7 \pm 1.0) \times 10^{-3}$
$\ell^- \bar{\nu}_\ell \Sigma_c(2455)^0 \pi^+$	$(2.7 \pm 1.0) \times 10^{-3}$
$\ell^- \bar{\nu}_\ell \Lambda_c f_0$	2.6×10^{-3}
$\ell^- \bar{\nu}_\ell \Lambda_c \pi^+ \pi^-$ (NR)	5.2×10^{-3}
$\ell^- \bar{\nu}_\ell \Lambda_c \pi^0 \pi^0$ (NR)	2.6×10^{-3}

TABLE VII: Ground state charm branching fractions \mathcal{B} used in the measurement (from Ref. [42]).

Charm Decay	\mathcal{B} [%]
$D^+ \rightarrow K^- \pi^+ \pi^+$	8.8 ± 0.6
$D^0 \rightarrow K^- \pi^+$	3.80 ± 0.09
$D^{*+} \rightarrow D^0 \pi^+$	67.7 ± 0.5
$D_s^+ \rightarrow \phi \pi^+$	3.6 ± 0.9
$\phi \rightarrow K^+ K^-$	49.1 ± 0.6
$\Lambda_c^+ \rightarrow p K^- \pi^+$	5.0 ± 1.3


 FIG. 10: Comparisons of $\mu^- \Lambda_c^+$ transverse momentum spectrum between data and Monte Carlo simulation generated according to the p_T spectrum inferred from (a) the inclusive J/ψ cross-section measurement and (b) the tuned semileptonic Λ_b^0 spectrum. The corresponding bottom plots show the ratio of data over MC with fits of a constant (dotted) and straight line (solid) overlaid.

hadron p_T spectrum measured from the inclusive J/ψ cross-section measurement [20]. The re-weighting function is determined from the disagreement between the $\ell^- \Lambda_c^+$ data and the generated spectrum, which is fit to a first order polynomial, $w = b + m \cdot p_T$, where $b = 1.43 \pm 0.08$ and $m = -0.026 \pm 0.007$ are the values of the fit averaged between the e +SVT and μ +SVT data. The tuned spectrum is then varied by $\pm 2\sigma$ of the uncertainty on the slope (σ_m) to bound the uncertainty on this spectrum (see Sec. VII). All of the Monte Carlo simulation events are generated with an input p_T threshold of $p_T(\bar{B}) > 5$ GeV/ c and $|\eta(\bar{B})| < 1.1$.

After the bottom hadron is generated, it is then decayed using the EVTGEN decay package [45], which decays the particles according to a user-specified decay chain and theoretical

decay models. The \bar{B} meson form factors used in the Monte Carlo simulation for this analysis are taken from various models based on heavy quark effective theory (HQET) [50, 51]. The ISGW2 [50] model implemented in EVTGEN governs the \bar{B} meson semileptonic decays to the ground state and doubly excited charm mesons, while the HQET decay model, implemented in EVTGEN, is used for the \bar{B} meson semileptonic decays to excited charm states. Non-resonant D^{**} meson decays are described by the model developed by Goity and Roberts [51]. The Λ_b^0 baryon semileptonic decay model is newly implemented [43] into the EVTGEN package for this measurement. The baryon form factors for the primary semileptonic $\Lambda_b^0 \rightarrow \ell^- \bar{\nu}_\ell \Lambda_c^{+(*,**)}$ decays are taken from constituent quark model calculations made by Pervin *et al.* [52]. These results agree with the large N_c predictions by Leibovich and Stewart [53] to order $\mathcal{O}(1/m_Q)$. Non-resonant Λ_b^0 decays, which are expected to contribute comparatively little to the total Λ_b^0 semileptonic width, are described by a phase space decay model.

1. Data - Simulation Comparison

Four inclusive Monte Carlo simulation samples, $\bar{B}^0 \rightarrow \ell^- \bar{\nu}_\ell D^{0,+} X$, $B^- \rightarrow \ell^- \bar{\nu}_\ell D^{0,+} X$, $\bar{B}_s^0 \rightarrow \ell^- \bar{\nu}_\ell D_s^+ X$, and $\Lambda_b^0 \rightarrow \ell^- \bar{\nu}_\ell \Lambda_c^+ X$ are generated to validate the use of simulation to determine the kinematic efficiencies of the bottom hadron semileptonic decays used in the measurement. The agreement between the data and the Monte Carlo should not be very sensitive to variations in the D^{**} branching fractions between the default EVTGEN table and the one to be later determined in the fit for the fragmentation fractions. The agreement between data and Monte Carlo simulation is checked for quantities used in the signal selection (listed in Table I). In general, the agreement between data and simulation is good in both the $\mu+$ SVT and $e+$ SVT data. A typical example of comparisons between data and Monte Carlo in the $\mu+$ SVT sample is shown in Fig. 11 for (a) $ct^*(\mu^- D^+)$, (b) $\sigma_{ct^*}(\mu^- D^+)$, (c) $p_T(\mu^- D^+)$, and (d) $m(\mu^- D^+)$. A complete set of comparisons between data and MC can be found in Ref. [43]. The area of the simulation distribution is normalized to the corresponding area of the data distribution for this comparison. The quality of the comparisons are quantified by fitting the ratio of the data to the simulation by both a first order polynomial and a constant. The former indicates potential biases between the two distributions (*i.e.* whether the simulation distribution is too hard or soft relative to the data), while the latter gives a measure of overall agreement between the distributions. No significant disagreement, determined from the fit to a constant line, is observed between data and simulation in the quantities used for the signal selection.

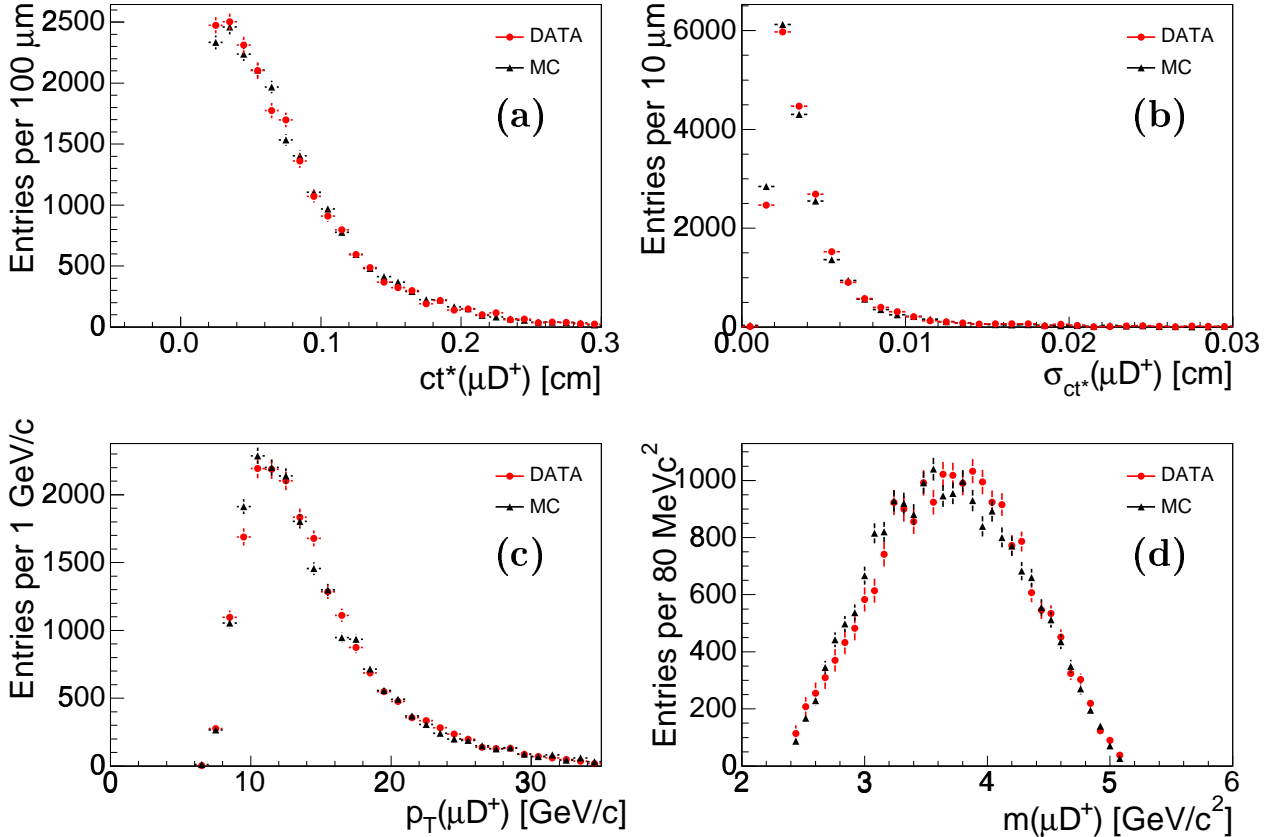


FIG. 11: Data-MC comparisons for $\mu^- D^+$ of (a) $ct^*(\mu^- D^+)$, (b) $\sigma_{ct^*}(\mu^- D^+)$, (c) $p_T(\mu^- D^+)$, and (d) $m(\mu^- D^+)$.

B. Relative Efficiency Determination from Data

Many efficiencies in the measurement of the relative fragmentation fractions are expected to cancel, and many of the remaining relative efficiencies are determined from the Monte Carlo simulation. The few efficiencies that are not well described by the simulation are determined from the data and discussed next.

1. XFT Efficiency

Differences in the XFT efficiencies of kaons, pions, and protons are expected due to the stringent hit requirement placed on COT tracks by the XFT trigger. Since the dE/dx of kaons and protons is lower than the dE/dx of pions for $p_t > 2 \text{ GeV}/c$, the COT hit requirement leads to a lower efficiency for kaons and protons relative to the pion XFT efficiency. These efficiencies are difficult to describe in the Monte Carlo simulation due to varying COT operating conditions during the data-taking period of this measurement. Therefore, they are derived from the data. The SVT efficiencies, which contribute to the triggers used in

TABLE VIII: Parameterizations for the XFT Monte Carlo simulation corrections.

Data period	<i>K</i>		π	
	a_0	a_1	a_0	a_1
Feb'02-Oct'02	0.9931 ± 0.05	-0.0725 ± 0.02	0.9772 ± 0.03	0.00968 ± 0.01
Oct'02-Jan'03	0.9584 ± 0.02	-0.1952 ± 0.007	1.0016 ± 0.01	-0.1501 ± 0.005
Jan'03-Jun'03	0.9359 ± 0.02	-0.1919 ± 0.007	0.9851 ± 0.01	-0.1341 ± 0.004
Jun'03-Sep'03	0.9282 ± 0.01	-0.1897 ± 0.005	0.9921 ± 0.008	-0.1776 ± 0.004
Sep'03-Aug'04	0.9643 ± 0.01	-0.0907 ± 0.004	0.9931 ± 0.007	-0.0678 ± 0.003
proton				
	a_0	a_1	a_2	a_3
Feb'02-Jun'03	1.063 ± 0.090	-1.326 ± 0.963	3.198 ± 3.218	-2.203 ± 3.391

this measurement, depend directly on the XFT efficiencies. The species dependence of the SVT efficiencies originate entirely from the XFT, since the energy loss between K , π , and p are negligible in the silicon detector relative to the drift chamber. The differences in the SVT efficiencies between reconstructed lepton-charm channels are therefore described by the dependence of XFT efficiencies on particle species.

The XFT efficiencies for K and π are measured by reconstructing the $D^+ \rightarrow K^-\pi^+\pi^+$ decay mode in the two-track trigger (TTT) data sample, where two tracks are required to match to the SVT trigger and no lepton requirement is made. Two of the final state K or π tracks are matched to the SVT tracks. The track that is not matched to an SVT track is treated as the unbiased track, which is then examined to determine whether it could have fired the XFT trigger. Tracks that could have passed the XFT trigger are included in the numerator of the efficiency, while all unbiased tracks are included in the denominator. A similar procedure is carried out for the proton XFT efficiency, using $\Lambda^0 \rightarrow p\pi^-$ events reconstructed in data collected with the TTT, where two other tracks in the event are required to have fired the SVT trigger. These efficiencies, binned in time to span the data set used, are shown in Fig. 12 for K and π . The ratio of the K and π efficiencies determined in the data relative to those determined in the corresponding Monte Carlo simulation are shown in Fig. 13. These corrections are parametrized by linear functions of the form $a_0 + a_1/p_T$, and the obtained fit parameters are listed in Table VIII. Details of the fits for the proton XFT efficiency can be found in Ref. [43].

2. dE/dx Efficiency

The dE/dx efficiency of the \mathcal{LR} cut applied to the proton, discussed previously in Section II C 4, is also evaluated from data and the Monte Carlo simulation is adjusted accordingly. The $\Lambda^0 \rightarrow p\pi^-$ control sample is used to evaluate the efficiency of the $\mathcal{LR}(p) > 0.3$ cut

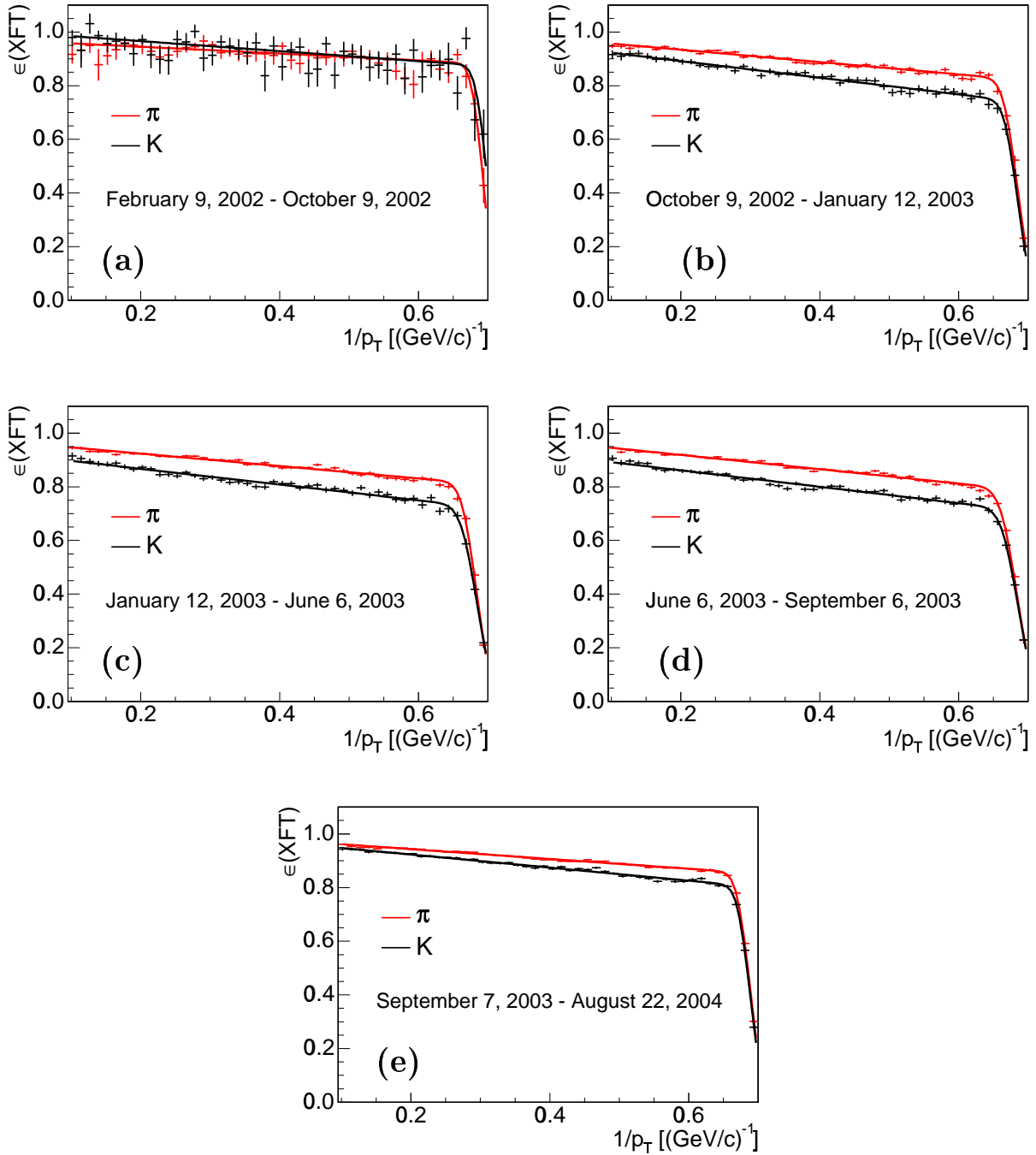


FIG. 12: XFT efficiency ϵ_{XFT} as a function of p_T^{-1} for pions (upper curve) and kaons (lower curve) for various run ranges indicated in distributions (a) through (e).

applied to the proton from the Λ_c^+ decay. The dE/dx efficiency is obtained by dividing the number of protons that pass the $dE/dx \mathcal{LR}(p)$ cut by all protons in bins of proton transverse momentum. The shape of the efficiency is parameterized by two functional forms: a third order polynomial plus a constant and using only a constant. Both parameterizations fit the

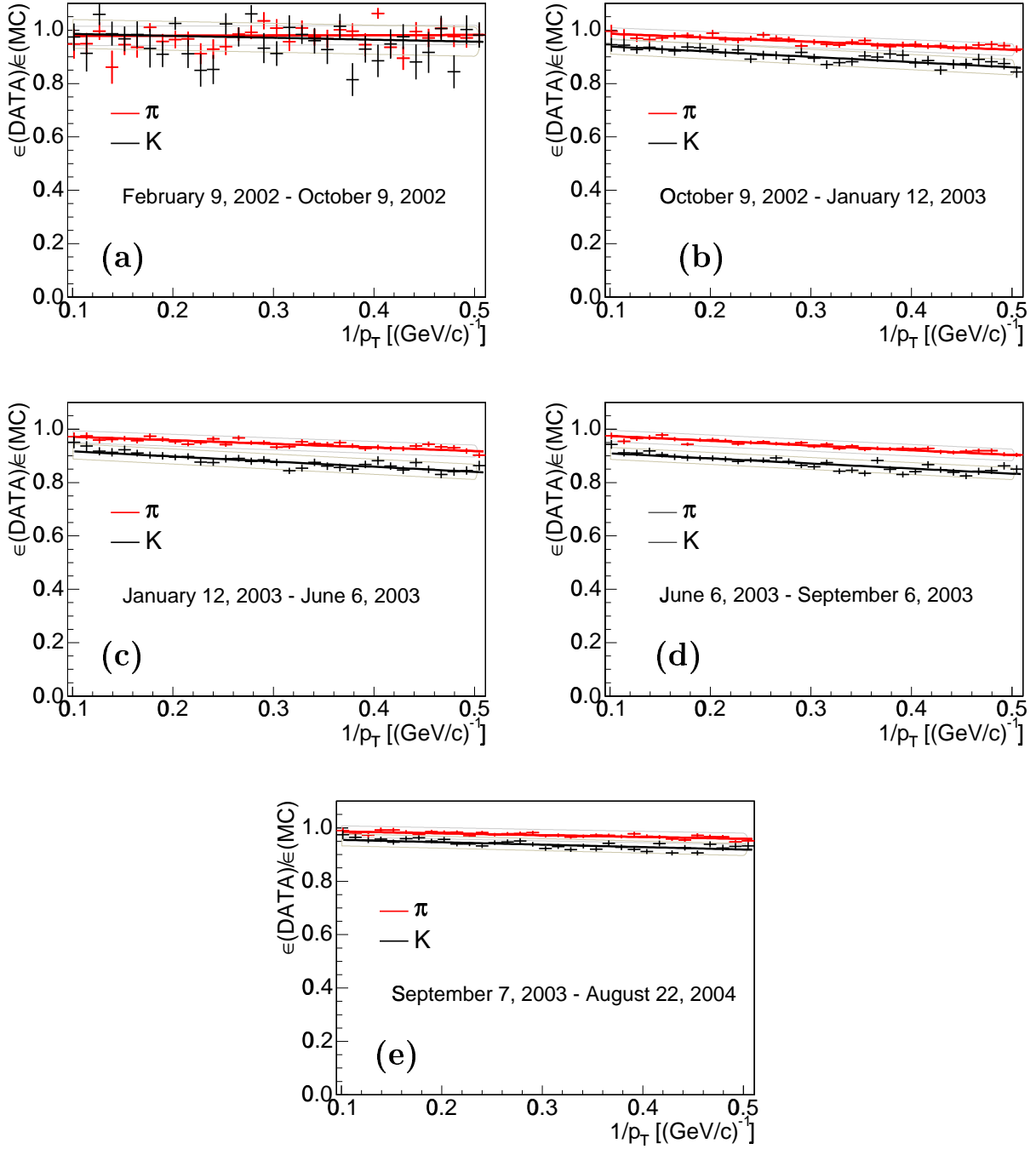


FIG. 13: Ratio $\epsilon_{\text{XFT}}(\text{DATA})/\epsilon_{\text{XFT}}(\text{MC})$ as a function of p_T^{-1} for pions (upper line) and kaons (lower line) for various run ranges indicated in distributions (a) through (e).

data well; the former is used as the default parameterization in the measurement, while the latter is used in the evaluation of systematic uncertainties (see Sec. VI).

3. Single Track Efficiency

The difference in efficiency between the two track charm topology in the $D^0 \rightarrow K^-\pi^+$ decay and a three track topology such as the $D^+ \rightarrow K^-\pi^+\pi^+$ decay arises from the efficiency of reconstructing an additional single track. Since the Monte Carlo simulation contains only the decay products of the generated bottom hadron and no additional tracks from the fragmentation process or underlying event, the efficiency of reconstructing a track in a simulation event is different from that in data. Thus the single track efficiency is determined from the data relative to the simulation. In order to evaluate this efficiency, the lepton plus four track state μ^-D^0 with $D^0 \rightarrow K^-\pi^+\pi^-\pi^+$, is reconstructed and normalized to the μ^-D^0 decay with $D^0 \rightarrow K^-\pi^+$ in both the data and the simulation. This represents the square of the efficiency, ε_{trk}^2 , to find a single track in the data relative to the simulation, assuming that the reconstruction of the third and fourth tracks in the $D^0 \rightarrow K^-\pi^+\pi^-\pi^+$ decay are uncorrelated. This assumption will be treated as a source of systematic uncertainty, as discussed in Sec. VI. This procedure yields the single track efficiency in data relative to the same efficiency in MC, $\varepsilon_{trk} = 87.8 \pm 0.8 \text{ (stat)}^{+1.9}_{-0.9} (\mathcal{B})\%$, where the systematic uncertainty is dominated by the knowledge of the relative branching fraction $\mathcal{B}(D^0 \rightarrow K^-\pi^+\pi^-\pi^+)/\mathcal{BR}(D^0 \rightarrow K^-\pi^+) = 2.10 \pm 0.03 \pm 0.06$ [54], which is used to adjust the generated Monte Carlo simulation samples for both D^0 decay modes.

4. Total Relative Efficiency

The relative efficiencies ε_{rel} that are included in the sample composition are the product of the acceptance ε_{accep} , lepton plus SVT trigger efficiency ε_{trigg} , analysis efficiency ε_{an} , and adjusted XFT efficiency $\varepsilon_{p/K/\pi \text{ trigg}}$,

$$\begin{aligned} \varepsilon_{rel}(\ell^- D^+) &= \varepsilon_{accep}(\text{MC}) \times \varepsilon_{trigg}(\text{MC}) \times \varepsilon_{an}(\text{MC}) \\ &\quad \times \varepsilon_{p/K/\pi \text{ trigg}}(\text{data/MC}). \end{aligned} \quad (10)$$

The relative efficiencies are similar for the other lepton-charm signals. An extra factor of $\varepsilon_{track}^{-1}(\text{data/MC})$ is needed for $\varepsilon_{rel}(\ell^- D^0)$ and $\varepsilon_{rel}(\ell^- D^{*+})$ to adjust the two track charm topology relative to the three track charm states, while the $\ell^- \Lambda_c^+$ relative efficiency requires an additional efficiency correction $\varepsilon_{dE/dx}(\text{data})$ for the dE/dx cut imposed on the proton candidate.

Monte Carlo yields in each channel are determined by fitting the simulation signal with a double Gaussian, analogous to the fits to the data. A single Gaussian is used to obtain the yield in the indirect lepton-charm decays, where the lepton originates from $\bar{B} \rightarrow \tau^- DX$, $\tau^- \rightarrow \ell^- X$, or another charm (*e.g.* $\bar{B} \rightarrow D\bar{D}X$, $\bar{D} \rightarrow \ell^- X$), because the yields are generally quite low in these channels and are poorly described by a double Gaussian. The total efficiencies derived for $\ell^- D^+$, $\ell^- D^0$, $\ell^- D^{*+}$, and $\ell^- D_s^+$ channels are listed

in Tables IX-XII for each \bar{B} mode considered in the sample composition. The efficiencies are calculated relative to a reference channel where the yield out of 10^7 generated events is listed for each corresponding reference channel. All of the decays shown in the tables are generated separately and for each decay 10^7 events are generated. The relative efficiencies for the primary semileptonic decays do not include the branching fractions. The efficiencies for the “physics backgrounds” include the semileptonic branching fractions of the D or τ , as well as the $\bar{B} \rightarrow DDX$ sample composition. Since a fixed sample composition is used for the $\Lambda_b^0 \rightarrow \ell^- \bar{\nu}_\ell \Lambda_c^+ X$ decays, the efficiencies quoted in Table XIII have the excited charm baryon branching fractions from Table VI applied.

V. FIT OF RELATIVE FRAGMENTATION FRACTIONS

A χ^2 -fit is used to extract the fragmentation fractions from the sample composition of the semileptonic bottom hadron decays reconstructed. The measured yields in the five lepton-charm signals are fit to the yields predicted by the sample composition procedure, and the decay rates ($\Gamma^{(*,**)}$) of the \bar{B} meson to the ground and excited states are constrained within their errors. The χ^2 , which is minimized, is

$$\begin{aligned} \chi^2 = & \sum_{i=1}^5 \left(\frac{N(\ell^- D_i)_{\text{measured}} - N(\ell^- D_i)_{\text{predicted}}}{\sigma(N(\ell^- D_i)_{\text{measured}})} \right)^2 \\ & + \left(\frac{\Gamma - \Gamma_{\text{PDG}}}{\sigma_{\Gamma_{\text{PDG}}}} \right)^2 + \left(\frac{\Gamma^* - \Gamma_{\text{PDG}}^*}{\sigma_{\Gamma_{\text{PDG}}^*}} \right)^2 + \left(\frac{\Gamma^{**} - \Gamma_{\text{PDG}}^{**}}{\sigma_{\Gamma_{\text{PDG}}^{**}}} \right)^2, \end{aligned} \quad (11)$$

where $N_{\text{predicted}}$ is determined from the sample composition process and N_{measured} is obtained from the data (see Tab. II). In order to fit in terms of better measured quantities, the number of predicted lepton-charm events are expressed in terms of $N(\bar{B}^0)$, which is an overall normalization in the fit and not indicative of the physical number of \bar{B}^0 mesons in the data, and in terms of the \bar{B} meson lifetimes relative to the lifetime of the \bar{B}^0 . The predicted number of lepton-charm events used in the fit for the \bar{B} mesons is expressed as:

$$\begin{aligned} N(\ell^- D_i)_{\text{predicted}} = & \sum_{j=d,u,s} N(\bar{B}^0) \frac{f_j}{f_d} \times \tau(\bar{B}^0) \\ & \times \tau(B_j)/\tau(\bar{B}^0) \sum_k \Gamma_k \times \sum_m \mathcal{B}(D_{jkm} \rightarrow D_i) \mathcal{B}(D_i) \varepsilon_{ijkm} \\ = & \sum_{j=d,u,s} N(\bar{B}^0) \frac{f_j}{f_u + f_d} \left(1 + \frac{f_u}{f_d} \right) \times \tau(\bar{B}^0) \\ & \times \tau(B_j)/\tau(\bar{B}^0) \sum_k \Gamma_k \times \sum_m \mathcal{B}(D_{jkm} \rightarrow D_i) \mathcal{B}(D_i) \varepsilon_{ijkm}, \end{aligned} \quad (12)$$

where $D_i = D^+, D^0, D^{*+}, D_s^+$, $\Gamma_k = \Gamma, \Gamma^*, \Gamma^{**}$, and the sum over m applies to Γ^{**} if there is more than one D^{**} state or non-resonant decay that can contribute to the final state D_i . In

TABLE IX: Efficiencies from $\ell^- D^+$ Monte Carlo simulation. For display purpose, the efficiencies are given relative to the ground state charm mode with the yield of the semileptonic decay into the ground state charm mode included in parentheses.

Decays	$e+SVT$	$\mu+SVT$
$\bar{B}^0 \rightarrow \ell^- \bar{\nu} D^+$	$1.089 \cdot 10^{-3}$ (10,890±110)	$1.307 \cdot 10^{-3}$ (13,070±120)
$\ell^- \bar{\nu} D^{*+}(D^+ \pi^0/\gamma)$	1.061 ± 0.015	1.100 ± 0.013
$\ell^- \bar{\nu} D_1^+(\pi^0 D^{*+})(D^+ \pi^0/\gamma)$	0.672 ± 0.011	0.750 ± 0.010
$\ell^- \bar{\nu} D_0^{*+}(D^+ \pi^0)$	0.625 ± 0.010	0.712 ± 0.010
$\ell^- \bar{\nu} D_1'^+(D^0 D^{*+})(D^+ \pi^0/\gamma)$	0.680 ± 0.010	0.748 ± 0.010
$\ell^- \bar{\nu} D_2^{*+}(\pi^0 D^{*+})(D^+ \pi^0/\gamma)$	0.673 ± 0.011	0.753 ± 0.010
$\ell^- \bar{\nu} D_2^{*+}(D^+ \pi^-)$	0.696 ± 0.011	0.783 ± 0.011
$\ell^- \bar{\nu} D^{*+} \pi^0(D^+ \pi^0/\gamma)$ (NR)	0.485 ± 0.008	0.638 ± 0.009
$\ell^- \bar{\nu} D^+ \pi^0$ (NR)	0.544 ± 0.009	0.764 ± 0.010
$D^{(*)} \bar{D}^{(*)} K(\ell D^+ X)$	0.0012 ± 0.0002	0.0044 ± 0.0003
$D^{(*)+} D^{(*)-}(\ell D^+ X)$	0.0092 ± 0.0004	0.0160 ± 0.0005
$D_s^{(*)} D^{(*)} X(\ell D^+ X)$	0.0027 ± 0.0002	0.0069 ± 0.0003
$\tau^- \bar{\nu} D^{(*,**)}(\ell D^+ X)$	0.0212 ± 0.0005	0.0282 ± 0.0007
$B^- \rightarrow \ell^- \bar{\nu} D_1^0(\pi^- D^{*+})(D^+ \pi^0/\gamma)$	0.658 ± 0.011	0.754 ± 0.011
$\ell^- \bar{\nu} D_0^{*0}(D^+ \pi^-)$	0.622 ± 0.010	0.727 ± 0.010
$\ell^- \bar{\nu} D_1'^0(\pi^- D^{*+})(D^+ \pi^0/\gamma)$	0.671 ± 0.011	0.753 ± 0.011
$\ell^- \bar{\nu} D_2^0(\pi^- D^{*+})(D^+ \pi^0/\gamma \pi^-)$	0.646 ± 0.011	0.759 ± 0.011
$\ell^- \bar{\nu} D_2^{*0}(D^+ \pi^-)$	0.666 ± 0.011	0.763 ± 0.011
$\ell^- \bar{\nu} D^{*+} \pi^-(D^+ \pi^0/\gamma)$ (NR)	0.491 ± 0.010	0.626 ± 0.009
$\ell^- \bar{\nu} D^+ \pi^-$ (NR)	0.534 ± 0.009	0.767 ± 0.010
$D^{(*)} \bar{D}^{(*)} K(\ell D^+ X)$	0.0005 ± 0.0001	0.0013 ± 0.0001
$D_s^{(*)} D^{(*)} X(\ell D^+ X)$	0.0008 ± 0.0001	0.0038 ± 0.0002
$\tau^- \bar{\nu} D^{(*,**)}(\ell D^+ X)$	0.0031 ± 0.0002	0.0045 ± 0.0002
$\bar{B}_s^0 \rightarrow \ell^- \bar{\nu} D_{s1}'^+(2535)(K^0 D^{*+})(D^+ \pi^0/\gamma)$	0.612 ± 0.010	0.695 ± 0.010
$\ell^- \bar{\nu} D_{s2}^{*+}(2573)(K^0 D^{*+})(D^+ \pi^0/\gamma)$	0.575 ± 0.009	0.665 ± 0.009
$\ell^- \bar{\nu} D_{s2}^{*+}(2573)(D^+ K^0)$	0.592 ± 0.010	0.691 ± 0.009
$D^{(*)} \bar{D}^{(*)} K(\ell D^+ X)$	0.0024 ± 0.0002	0.0073 ± 0.0003
$D_s^{(*)} D^{(*)} X(\ell D^+ X)$	0.0011 ± 0.0001	0.0037 ± 0.0002

that case the sum is weighted according to the branching fractions $\mathcal{BR}(D_{jkm} \rightarrow D_i)$ of the various contributing D^{**} states. The efficiencies ε_{ijkm} refer to the corresponding absolute efficiencies of events obtained in a particular final state normalized to the generated number of MC events with $p_T(\bar{B}) > 5$ GeV/ c . These efficiencies are detailed in Tables IX through

TABLE X: Efficiencies in $\ell^- D^0$ Monte Carlo simulation.

Decays	$e+SVT$	$\mu+SVT$
$\bar{B}^0 \rightarrow \ell^- \bar{\nu} D^{*+}(D^0 \pi^+)$	0.970 ± 0.012	1.028 ± 0.012
$\ell^- \bar{\nu} D_1^+(\pi^0 D^{*+})(D^0 \pi^+)$	0.616 ± 0.008	0.702 ± 0.009
$\ell^- \bar{\nu} D_1^+(\pi^+ D^{*0})(D^0 \pi^0/\gamma)$	0.605 ± 0.009	0.682 ± 0.009
$\ell^- \bar{\nu} D_0^{*+}(D^0 \pi^+)$	0.577 ± 0.008	0.679 ± 0.009
$\ell^- \bar{\nu} D_1^{' +}(\pi^0 D^{*+})(D^0 \pi^+)$	0.640 ± 0.009	0.700 ± 0.009
$\ell^- \bar{\nu} D_1^{' +}(\pi^+ D^{*0})(D^0 \pi^0/\gamma)$	0.557 ± 0.008	0.631 ± 0.008
$\ell^- \bar{\nu} D_2^{*+}(\pi^0 D^{*+})(D^0 \pi^+)$	0.613 ± 0.009	0.707 ± 0.009
$\ell^- \bar{\nu} D_2^{*+}(\pi^+ D^{*0})(D^0 \pi^0/\gamma)$	0.622 ± 0.009	0.696 ± 0.009
$\ell^- \bar{\nu} D_2^{*+}(D^0 \pi^0)$	0.640 ± 0.009	0.745 ± 0.010
$\ell^- \bar{\nu} D^{*+} \pi^0(D^0 \pi^+) \text{ (NR)}$	0.461 ± 0.007	0.562 ± 0.008
$\ell^- \bar{\nu} D^{*0} \pi^+(D^0 \pi^0/\gamma) \text{ (NR)}$	0.451 ± 0.007	0.578 ± 0.008
$\ell^- \bar{\nu} D^0 \pi^+ \text{ (NR)}$	0.518 ± 0.008	0.698 ± 0.009
$D^{(*)} \bar{D}^{(*)} K(\ell D^0 X)$	0.0024 ± 0.0002	0.0084 ± 0.0003
$D^{(*)+} D^{(*)-}(\ell D^0 X)$	0.0033 ± 0.0002	0.0074 ± 0.0003
$D_s^{(*)} D^{(*)} X(\ell D^0 X)$	0.0026 ± 0.0001	0.007 ± 0.0002
$\tau^- \bar{\nu} D^{(*,**)}(\ell D^0 X)$	0.0225 ± 0.0005	0.0311 ± 0.0007
$B^- \rightarrow \ell^- \bar{\nu} D^0$	$1.376 \cdot 10^{-3} (13,760 \pm 120)$	$1.535 \cdot 10^{-3} (15,350 \pm 130)$
$\ell^- \bar{\nu} D^{*0}(D^0 \pi^0/\gamma)$	1.024 ± 0.012	1.057 ± 0.012
$\ell^- \bar{\nu} D_1^0(\pi^0 D^{*0})(D^0 \pi^0/\gamma)$	0.643 ± 0.009	0.717 ± 0.009
$\ell^- \bar{\nu} D_1^0(\pi^- D^{*+})(D^0 \pi^+)$	0.607 ± 0.009	0.710 ± 0.009
$\ell^- \bar{\nu} D_0^{*0}(D^0 \pi^0)$	0.619 ± 0.009	0.716 ± 0.009
$\ell^- \bar{\nu} D_1^{' 0}(\pi^0 D^{*0})(D^0 \pi^0/\gamma)$	0.648 ± 0.009	0.742 ± 0.009
$\ell^- \bar{\nu} D_1^{' 0}(\pi^- D^{*+})(D^0 \pi^+)$	0.609 ± 0.009	0.709 ± 0.009
$\ell^- \bar{\nu} D_2^{*0}(\pi^0 D^{*0})(D^0 \pi^0/\gamma)$	0.638 ± 0.009	0.726 ± 0.009
$\ell^- \bar{\nu} D_2^{*0}(\pi^- D^{*+})(D^0 \pi^+)$	0.598 ± 0.009	0.710 ± 0.009
$\ell^- \bar{\nu} D_2^{*0}(D^0 \pi^0)$	0.662 ± 0.009	0.757 ± 0.009
$\ell^- \bar{\nu} D^{*+} \pi^-(D^0 \pi^+) \text{ (NR)}$	0.456 ± 0.007	0.580 ± 0.008
$\ell^- \bar{\nu} D^{*0} \pi^0(D^0 \pi^0/\gamma) \text{ (NR)}$	0.474 ± 0.007	0.597 ± 0.008
$\ell^- \bar{\nu} D^0 \pi^0 \text{ (NR)}$	0.565 ± 0.008	0.745 ± 0.009
$D^{(*)} \bar{D}^{(*)} K(\ell D^0 X)$	0.0033 ± 0.0002	0.0104 ± 0.0004
$D_s^{(*)-} D^{(*)0}(\ell D^0 X)$	0.0044 ± 0.0003	0.0109 ± 0.0003
$\tau^- \bar{\nu} D^{(*,**)}(\ell D^0 X)$	0.0403 ± 0.0007	0.0523 ± 0.0009
$\bar{B}_s^0 \rightarrow \ell^- \bar{\nu} D_{s1}^{' +}(2535)(K^0 D^{*+})(D^0 \pi^+)$	0.541 ± 0.008	0.638 ± 0.008
$\ell^- \bar{\nu} D_{s1}^{' +}(2535)(K^+ D^{*0})(D^0 \pi^0/\gamma)$	0.519 ± 0.008	0.633 ± 0.008
$\ell^- \bar{\nu} D_{s2}^{*+}(2573)(K^0 D^{*+})(D^0 \pi^+)$	0.513 ± 0.008	0.614 ± 0.008
$\ell^- \bar{\nu} D_{s2}^{*+}(2573)(K^+ D^{*0})(D^0 \pi^0/\gamma)$	0.501 ± 0.008	0.621 ± 0.008
$\ell^- \bar{\nu} D_{s2}^{*+}(2573)(D^0 K^+)$	0.537 ± 0.008	0.639 ± 0.008
$D^{(*)} \bar{D}^{(*)} K(\ell D^0 X)$	0.0022 ± 0.0002	0.0072 ± 0.0003
$D_s^{(*)} D^{(*)} X(\ell D^0 X)$	0.0014 ± 0.0001	0.0056 ± 0.0002

TABLE XI: Efficiencies in $\ell^- D^{*+}$ Monte Carlo simulation.

Decays	$e+$ SVT	$\mu+$ SVT
$\bar{B}^0 \rightarrow \ell^- \bar{\nu} D^{*+}(D^0 \pi^+)$	$0.888 \cdot 10^{-3} (8,880 \pm 100)$	$1.068 \cdot 10^{-3} (10,680 \pm 100)$
$\ell^- \bar{\nu} D_1^+(\pi^0 D^{*+})(D^0 \pi^+)$	0.642 ± 0.011	0.696 ± 0.010
$\ell^- \bar{\nu} D_1'^+(\pi^0 D^{*+})(D^0 \pi^+)$	0.680 ± 0.011	0.691 ± 0.011
$\ell^- \bar{\nu} D_2^{*+}(\pi^0 D^{*+})(D^0 \pi^+)$	0.642 ± 0.011	0.698 ± 0.011
$\ell^- \bar{\nu} D^{*+} \pi^0(D^0 \pi^+) (\text{NR})$	0.484 ± 0.009	0.552 ± 0.009
$D^{(*)} \bar{D}^{(*)} K(\ell D^{*+} X)(D^0 \pi^+)$	0.0010 ± 0.0003	0.0028 ± 0.0002
$D^{(*)+} D^{(*)-}(\ell D^{*+} X)(D^0 \pi^+)$	0.0033 ± 0.0003	0.0064 ± 0.0004
$D_s^{(*)} D^{(*)} X(\ell D^{*+} X)(D^0 \pi^+)$	0.00105 ± 0.00004	0.0023 ± 0.0002
$\tau^- \bar{\nu} D^{(*,**)}(\ell D^{*+} X)(D^0 \pi^+)$	0.018 ± 0.003	0.0235 ± 0.0007
<hr/>		
$B^- \rightarrow \ell^- \bar{\nu} D_1^0(\pi^- D^{*+})(D^0 \pi^+)$	0.646 ± 0.011	0.696 ± 0.011
$\ell^- \bar{\nu} D_1'^0(\pi^- D^{*+})(D^0 \pi^+)$	0.640 ± 0.011	0.701 ± 0.011
$\ell^- \bar{\nu} D_2^{*0}(\pi^- D^{*+})(D^0 \pi^+)$	0.620 ± 0.011	0.688 ± 0.011
$\ell^- \bar{\nu} D^{*+} \pi^-(D^0 \pi^+) (\text{NR})$	0.466 ± 0.009	0.577 ± 0.009
$D^{(*)} \bar{D}^{(*)} K(\ell D^{*+} X)(D^0 \pi^+)$	0.0006 ± 0.0001	0.0013 ± 0.0002
$D_s^{(*)} D^{(*)} X(\ell D^{*+} X)(D^0 \pi^+)$	0.00028 ± 0.00006	0.00021 ± 0.00007
$\tau^- \bar{\nu} D^{(*,**)}(\ell D^{*+} X)(D^0 \pi^+)$	0.002 ± 0.001	0.0024 ± 0.0009
<hr/>		
$\bar{B}_s^0 \rightarrow \ell^- \bar{\nu} D_{s1}'^+(2535)(K^0 D^{*+})(D^0 \pi^+)$	0.553 ± 0.010	0.620 ± 0.010
$\ell^- \bar{\nu} D_{s2}^{*+}(2573)(K^0 D^{*+})(D^0 \pi^+)$	0.525 ± 0.010	0.593 ± 0.009
$D^{(*)} \bar{D}^{(*)} K(\ell D^{*+} X)(D^0 \pi^+)$	0.0007 ± 0.0003	0.0022 ± 0.0003
$D_s^{(*)} D^{(*)} X(\ell D^{*+} X)(D^0 \pi^+)$	0.00024 ± 0.00008	0.0012 ± 0.0002

XII. In the case of the Λ_b^0 baryon, where a fixed sample composition is used, the predicted number of events is given as

$$N(\ell^- \Lambda_c^+)_{\text{predicted}} = N(\bar{B}^0) \frac{f_{\Lambda_b}}{f_u + f_d} \left(1 + \frac{f_u}{f_d} \right) \times \mathcal{B}(\Lambda_b^0 \rightarrow \ell^- \bar{\nu}_\ell \Lambda_c^+ X) \mathcal{B}(\Lambda_c^+ \rightarrow p K^- \pi^+) \times \varepsilon(\Lambda_b^0 \rightarrow \ell^- \bar{\nu}_\ell \Lambda_c^+ X). \quad (13)$$

In this case, the excited charm baryon branching fractions into the Λ_c^+ state are included in the efficiency $\varepsilon(\Lambda_b^0 \rightarrow \ell^- \bar{\nu}_\ell \Lambda_c^+ X)$ in Eq. (13), as listed in Table XIII.

There are four free parameters in the fit for the fragmentation fractions: three relative fragmentation parameters f_u/f_d , $f_s/(f_u+f_d)$, $f_{\Lambda_b}/(f_u+f_d)$, and the normalization parameter $N(\bar{B}^0)$, plus three constrained parameters: Γ , Γ^* , and Γ^{**} . The values of f_s and f_{Λ_b} are fit relative to (f_u+f_d) to minimize as many biases in the measurement as possible and to highlight the fact that the \bar{B}_s^0 is reconstructed relative to the \bar{B}^0 and B^- signals. Additionally, performing the fit relative to $f_u + f_d$ limits any possible inaccuracies in the separation of \bar{B}^0 and B^- through the sample composition procedure into the $\ell^- D^0$ and $\ell^- D^+$ final states. As

TABLE XII: Efficiencies in $\ell^- D_s^+$ Monte Carlo simulation.

Decays	e +SVT	μ +SVT
$\bar{B}_s^0 \rightarrow \ell^- \bar{\nu} D_s^+$	$0.998 \cdot 10^{-3}$ ($9,980 \pm 100$)	$1.201 \cdot 10^{-3}$ ($12,010 \pm 110$)
$\ell^- \bar{\nu} D_s^{*+}(D_s^+ \gamma)$	1.035 ± 0.014	1.11 ± 0.014
$\ell^- \bar{\nu} D_{s0}^{*+}(2317)(D_s^+ \pi^0)$	0.684 ± 0.011	0.773 ± 0.011
$\ell^- \bar{\nu} D_{s1}^+(2460)(\pi^0 D_{s0}^{*+})(D_s^+ \pi^0)$	0.709 ± 0.011	0.786 ± 0.011
$\ell^- \bar{\nu} D_{s1}^+(2460)(D_s^+ \gamma)$	0.710 ± 0.011	0.781 ± 0.011
$\ell^- \bar{\nu} D_s^{*+} \pi^0(D_s^+ \gamma)$ (NR)	0.436 ± 0.008	0.591 ± 0.009
$\ell^- \bar{\nu} D_s^+ \pi^0$ (NR)	0.479 ± 0.008	0.722 ± 0.010
$D_s^{(*)} D^{(*)} X(\ell D_s^+ X)$	0.0023 ± 0.0003	0.0086 ± 0.0007
$D_s^{(*)+} D_s^{(*)-}(\ell D_s^+ X)$	0.0075 ± 0.0003	0.0175 ± 0.0005
$\tau^- \bar{\nu} D_s^{(*,**)+}(\ell D_s^+ X)$	0.034 ± 0.005	0.052 ± 0.001
$\bar{B}^0 \rightarrow D_s^{(*)+} D^{(*)-}(\ell D_s^+ X)$	0.0055 ± 0.0003	0.0126 ± 0.0005
$B^+ \rightarrow D_s^{(*)+} D^{(*)-}(\ell D_s^+ X)$	0.0055 ± 0.0003	0.0109 ± 0.0005

 TABLE XIII: Efficiencies in $\ell^- \Lambda_c^+$ Monte Carlo simulation.

Decays	e +SVT	μ +SVT
$\Lambda_b^0 \rightarrow \ell^- \bar{\nu} \Lambda_c^+ X$	$0.629 \cdot 10^{-3}$ ($6,290 \pm 90$)	$0.722 \cdot 10^{-3}$ ($7,220 \pm 100$)
$\tau^- \bar{\nu} \Lambda_c^+ X(\ell \Lambda_c^+ X)$	0.026 ± 0.001	0.033 ± 0.0007

mentioned earlier, the sum of fragmentation fractions f_u , f_d , f_s , and f_{Λ_b} is not constrained to unity in the fit, since not all b baryons are necessarily accounted for by reconstructing $\ell^- \Lambda_c^+$ states.

The electron and muon samples are fit separately, since the relative lepton efficiencies between the electron and muon modes are not expected to readily cancel. The fit results are given in Table XIV with statistical errors only indicating good agreement between the e +SVT and μ +SVT data sets. As mentioned previously, f_q indicates the fragmentation fraction integrated above the momentum threshold of sensitivity in the data, $f_q \equiv f_q(p_T(\bar{B}) > 7 \text{ GeV}/c)$. Note that about 90% of the $\ell^- \Lambda_c^+$ combinations in data have transverse momenta below $\sim 20 \text{ GeV}/c$, but none have p_T less than $7 \text{ GeV}/c$.

VI. SYSTEMATIC UNCERTAINTIES

The main uncertainties in the measurement of the relative fragmentation fractions come from the uncertainties in the branching fractions of the charm mesons, which contribute both directly and indirectly to the measurement, and the uncertainty associated with the

TABLE XIV: Fit results with statistical errors only.

Fit Parameter	$e+$ SVT	$\mu+$ SVT
f_u/f_d	1.044 ± 0.028	1.062 ± 0.024
$f_s/(f_u + f_d)$	0.162 ± 0.008	0.158 ± 0.006
$f_{\Lambda_b}/(f_u + f_d)$	0.292 ± 0.020	0.275 ± 0.015
Γ [ps $^{-1}$]	0.0157 ± 0.0007	0.0154 ± 0.0007
Γ^* [ps $^{-1}$]	0.0327 ± 0.0014	0.0331 ± 0.0013
Γ^{**} [ps $^{-1}$]	0.0145 ± 0.0010	0.0146 ± 0.0010
$N(\bar{B}^0)$ (10^9)	2.02 ± 0.07	2.93 ± 0.10

baryon p_T spectrum, which affects the simulation-based efficiency. The uncertainties in the measurement due to the XFT and dE/dx efficiencies are negligible in comparison with other systematic uncertainties. The complete list of systematic uncertainties assigned to the fragmentation fractions is given in Table XVII. A weighted average between the $e+$ SVT and $\mu+$ SVT samples is calculated before and after applying a particular systematic variation in order to determine the systematic uncertainty for a given quantity. The determination of the individual systematic uncertainties is discussed in the following sections.

A. False Lepton Backgrounds

The wrong sign lepton-charm combinations represent several possible backgrounds that may be present in the right sign signals with a significant contribution to the wrong sign combinations expected to arise from false lepton candidates. Another contribution originates from real leptons from non-bottom sources, such as electrons from photon conversion $\gamma \rightarrow e^+e^-$ or muons from kaon and pion decay-in-flight. These sources are included in the discussion of false lepton backgrounds. The wrong sign signals are present in the data even after the prompt region is removed by requiring $ct^*(\ell^-D) > 200 \mu\text{m}$, as can be seen in Figs. 14 and 15. Additionally, some discrepancy is still observed in the $ct^*(\ell^-D)$ comparisons between data and simulation, possibly indicating a residual background from false leptons. False leptons that originate from a “ \bar{B} ”-like hadron (*i.e.* a relatively long-lived particle) are not necessarily represented equally between right sign and wrong sign combinations, as is the case with prompt false leptons. Since the false leptons of concern most likely come from a real bottom hadron in which a hadronic track has been mis-identified as a lepton, they are enhanced in the right sign over wrong sign lepton-charm combinations.

This systematic uncertainty is studied by utilizing the large false lepton sample available from the TTT semileptonic \bar{B} decays, which has approximately five times more ℓ^-D^+ and ℓ^-D^0 events than the $\ell+$ SVT trigger sample. Since the statistics are much larger in the TTT sample and the average lepton transverse momentum is lower, a larger sample of false

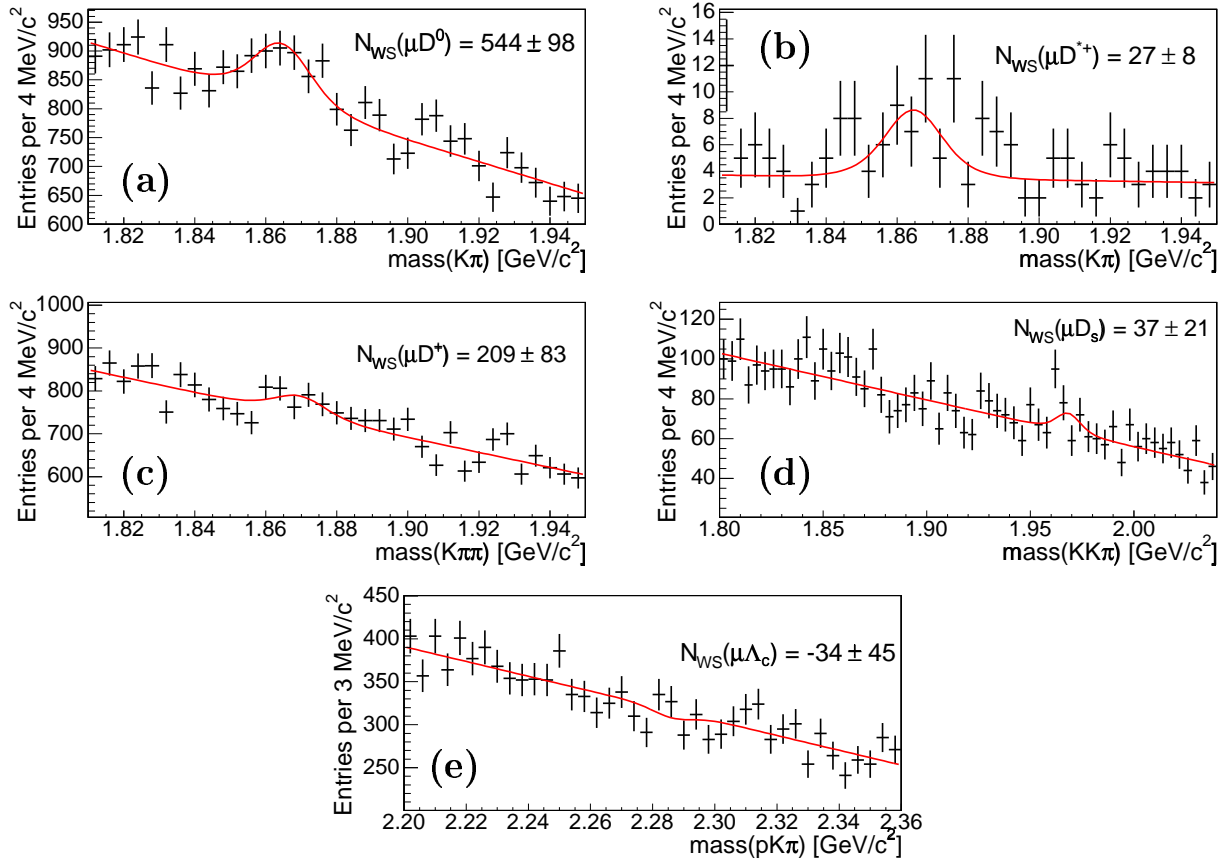


FIG. 14: μ +SVT wrong sign invariant mass distributions of (a) D^0 , (b) D^{*+} , (c) D^+ , (d) D_s^+ , and (e) Λ_c^+ after the $ct^*(\mu^-D)$ requirement.

leptons is available for the study. Lepton candidates with a low probability of being true leptons, as measured from a likelihood weighting of lepton identification variables [55, 56], are selected from semileptonic TTT events in which one of the charm daughters is matched to one SVT track and the lepton is matched to the other SVT trigger track. This sample of false leptons is then used to estimate the factor required to scale the residual wrong sign “signals” in the ℓ +SVT data to the right sign signals, giving an estimate of the false lepton contamination from bottom hadrons in the right sign signals. All selection requirements used in this analysis are applied and the numbers of right sign and wrong sign events are compared. The scaling obtained for false leptons from long-lived “bottom”-like hadrons is $w_e = 2.93 \pm 0.47$ and $w_\mu = 3.91 \pm 0.73$, assuming that all of the wrong sign events originate from long-lived sources. To obtain the systematic uncertainty, the right sign lepton-charm yields are decreased by the wrong sign yields scaled by the appropriate factor for the e +SVT and μ +SVT datasets. The fit for the fragmentation fractions is then repeated and the resulting systematic uncertainties noted in Table XVII.

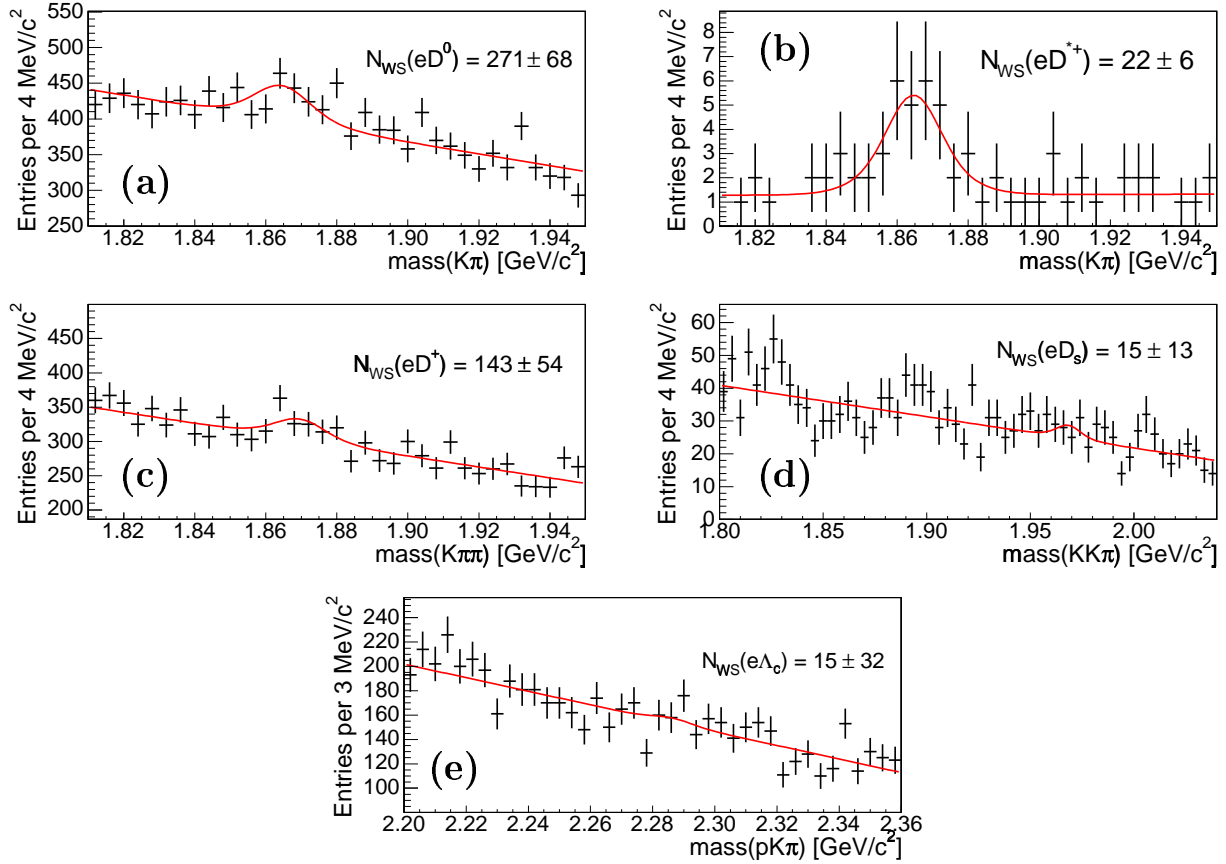


FIG. 15: $e+SVT$ wrong sign invariant mass distributions of (a) D^0 , (b) D^{*+} , (c) D^+ , (d) D_s^+ , and (e) Λ_c^+ after the $ct^*(e^-D)$ requirement.

B. Variation of Selection Requirements

The selection requirements have been chosen to be similar across the five lepton-charm channels, in order to cancel as many systematic uncertainties as possible while still respecting the different kinematic features of the decays. To check the dependence of the final result on these selection criteria, the signal selection has been varied in such a way that the $p_T(D) > 5 \text{ GeV}/c$ cut is applied to all channels, while the $\chi^2_{xy}(D)$ and vertex probability requirements are the same. The varied cuts used to assign the systematic uncertainty are listed in Table XV.

C. D_s^+ Reflection in the D^+ Signal

In addition to residual wrong sign backgrounds, another source of irreducible non-combinatorial background arises from the $D_s^+ \rightarrow K^+K^-\pi^+$ reflection into the $D^+ \rightarrow K^-\pi^+\pi^+$ signal. This effect has been measured from the data, using the simulation to scale the expected rates of generic $D_s^+ \rightarrow K^-K^+\pi^+$ decays to the $D_s^+ \rightarrow \phi\pi^+$ decay (see

TABLE XV: Alternative signal selection.

Cuts	$\ell^- D^0$	$\ell^- D^{*+}$	$\ell^- D^+$	$\ell^- D_s^+$	$\ell^- \Lambda_c^+$
$ct(D)$ [cm] \in	(-0.01,0.10)	(-0.01,0.10)	(-0.01,0.20)	(-0.01,0.10)	(-0.01,0.05)
$ct^*(\ell^- D)$ [cm] $>$	0.02	0.02	0.02	0.02	0.02
$\sigma_{ct^*}(\ell^- D)$ [cm] $<$	0.04	0.04	0.04	0.04	0.04
$m(\ell^- D)$ [GeV/c 2] \in	(2.4,5.1)	(2.4,5.1)	(2.4,5.1)	(2.4,5.1)	(3.4,5.5)
$p_T(D)$ [GeV/c] $>$	5.0	5.0	5.0	5.0	5.0
$p_T(p)$ [GeV/c] $>$	N/A	N/A	N/A	N/A	2.0
$p_T(K)$ [GeV/c] $>$	0.6	0.6	0.6	0.6	0.6
$\chi^2_{2D}(D) <$	10	10	10	10	10
vertex prob.($\ell^- D$) $>$	10^{-7}	10^{-7}	10^{-7}	10^{-7}	10^{-7}
$L_{xy}/\sigma_{Lxy}(D) >$	4.5	4.5	4.5	4.5	4.5
$\Delta m(D^{*+}, D^0)$ [GeV/c 2] \in	N/A	(0.1440,0.1475)	N/A	N/A	N/A
$ m(\phi) - 1.019 $ [GeV/c 2] $<$	N/A	N/A	N/A	0.0095	N/A
$dE/dx \mathcal{LR}(p)$ $>$	N/A	N/A	N/A	N/A	0.3

TABLE XVI: $\ell^- D^+$ yields with different D_s^+ reflection normalizations.

D_s^+ Reflection	e +SVT		μ +SVT	
	$N(D_s^+)$	$N(D^+ e^-)$	$N(D_s^+)$	$N(D^+ \mu^-)$
Constrained	$1,710 \pm 80$	$10,780 \pm 150$	$2,780 \pm 460$	$20,240 \pm 220$
Fixed	1,577	$10,780 \pm 150$	2,570	$20,270 \pm 250$
Floating	$3,270 \pm 1,100$	$10,570 \pm 200$	$5,050 \pm 1,670$	$19,910 \pm 340$
None	—	$11,020 \pm 160$	—	$20,640 \pm 260$

Section II C 5). By default, the D_s^+ reflection is included in the fit to the D^+ signal by constraining the normalization of the D_s^+ reflection within its uncertainty. In order to assign a systematic uncertainty on this method, the normalization of the reflection is allowed to vary, both by fixing $N(D_s^+)$ to the number measured from data, and also by allowing $N(D_s^+)$ to float in the fit to obtain the D^+ signal, listed for both scenarios in Table XVI. The larger effect is observed when $N(D_s^+)$ is a free fit parameter, while fixing the normalization produces a more moderate shift. Since the normalization procedure of $N(D_s^+ \rightarrow \phi\pi^+)$ relative to $N(D_s^+ \rightarrow K^+K^-\pi^+)$ is, in principle, well-understood from the data and simulation, the variations obtained from fixing the normalization are taken as the systematic uncertainty associated with this method.

D. XFT Efficiencies

Knowledge of efficiencies that are different for the different particle species is essential for the proper determination of the relative efficiencies between lepton-charm channels. One of these sets of efficiencies is the XFT trigger efficiencies (described in Section IV B 1), which cannot be accurately predicted by the simulation and are not expected to readily cancel in the relative efficiencies between the final state charm signals. The systematic uncertainty on this efficiency is determined by varying the default XFT efficiencies by 1σ of the fit parameters given in Table VIII. To determine the systematic uncertainty of the shift in the K - and π -XFT efficiencies, the π efficiency, which has the larger uncertainty of the two, is shifted up or down by the uncertainties in the XFT parameterizations, while the K efficiency is held constant. The systematic uncertainty associated with the proton efficiency is assigned by fitting the efficiency with a constant line. The proton parameterization was shifted by the full uncertainty on the fit parameters (either all up or all down), which are quite large as can be seen in Table VIII.

E. Single Track Efficiency

The efficiency to add a single track, needed to adjust the two track topology to the three track topology, is measured by reconstructing the $D^0 \rightarrow K^-\pi^+\pi^-\pi^+$ channel relative to the $D^0 \rightarrow K^-\pi^+$ decay mode (see Section IV B 3). This method assumes that the two additional pions in the $D^0 \rightarrow K^-\pi^+\pi^-\pi^+$ decay are uncorrelated. Since the two tracks are identified and pass through different parts of the detector, this assumption is reasonable. The only way the determination of the single track efficiency might be biased by the correlation of the third and fourth tracks arises from vertexing effects. To assess the degree of the bias that might occur in the vertexing of the $D^0 \rightarrow K^-\pi^+\pi^-\pi^+$ mode due to the correlation between the two additional pions, a three track vertex is formed in the Monte Carlo simulation of μ^-D^0 decays with $D^0 \rightarrow K^-\pi^+\pi^-\pi^+$ and the impact parameter of the fourth track with respect to the three track vertex is determined. If the impact parameter of the fourth track lies outside of 1σ of the error on the vertex and 1σ of the error on the impact parameter, it is assumed that the fourth track could bias the position of the vertex. The impact parameter of the fourth track is found to be outside 1σ of the three-track vertex ($5.3 \pm 0.1\%$) of the time. This fraction is assumed to correspond, to good approximation, to the degree of correlation in the efficiency of the third and fourth pions. Another source of uncertainty in the determination of the single track efficiency is the error on the ratio of branching fractions of the two reconstructed D^0 decays, $\mathcal{B}(D^0 \rightarrow K^-\pi^+\pi^-\pi^+)/\mathcal{B}(D^0 \rightarrow K^-\pi^+) = 2.10 \pm 0.03 \pm 0.06$ [54]. The systematic uncertainty from the error on this ratio of branching fractions is also included in the systematic uncertainty from the single track efficiency listed in Table XVII.

F. Sample Composition Lifetimes

\bar{B} meson lifetimes relative to the \bar{B}^0 lifetime are included in the sample composition procedure. Consequently, the \bar{B} lifetimes are needed to determine the predicted number of lepton-charm mesons (see Section V). As there are uncertainties on the PDG values [42] of the lifetimes used in the fit, which are listed in Table V, the lifetimes and lifetime ratios are varied in the process extracting the sample composition within their PDG uncertainties. The central value of the lifetime ratio $\tau(B^-)/\tau(\bar{B}^0) = 1.086 \pm 0.017$ has changed several times in several years and different values are used in the sundry measurements of f_u/f_d . Although the lifetime ratio in the PDG is slightly higher than that used in other measurements of f_u/f_d , the uncertainty on the PDG value covers the central value of the other possible lifetime ratios. No Λ_b^0 lifetime is used in the fit for the baryon sample composition, although $f_{\Lambda_b}/(f_u + f_d)$ varies slightly when the ratio $\tau(B^-)/\tau(\bar{B}^0)$ is varied within the PDG uncertainty, because the Λ_b^0 fragmentation fraction is measured relative to the \bar{B}^0 and B^- modes.

G. Monte Carlo Simulation Statistics

Since a finite number of Monte Carlo simulation events are generated for each exclusive decay to be used in the process to extract the sample composition (see Section III,) the statistics of the generated simulation is checked to see whether the statistical uncertainties on the yields, which are used to determine the efficiencies, contribute a significant uncertainty to the measurement. The simulation yields in each decay are shifted by $\pm 1\sigma$ around their central values and the efficiencies are re-determined accordingly. To assign the systematic uncertainty, half of the yields are randomly shifted up, while the other half are shifted down. In all cases, the shift in all three relative fragmentation fractions is small compared to the other uncertainties, as can be seen in Table XVII.

H. Bottom Hadron Lifetimes

Knowledge of the bottom hadron lifetimes is also needed for the generation of the various \bar{B} simulation samples. While the \bar{B}^0 and B^- lifetimes are well-measured, there are large uncertainties on the \bar{B}_s^0 and Λ_b^0 lifetimes [42]. To assign a systematic error due to the uncertainty in the knowledge of the \bar{B} and Λ_b^0 lifetimes, the simulation is re-generated with the \bar{B}_s^0 and Λ_b^0 lifetimes shifted by one sigma uncertainty on their PDG values: $\tau(\bar{B}_s^0) = (438 \pm 17) \mu\text{m}$ and $\tau(\Lambda_b^0) = (368 \pm 24) \mu\text{m}$. The shift in $f_{\Lambda_b}/(f_u + f_d)$ is one of the larger uncertainties in Table XVII, but it is still small compared to the uncertainties due to the imprecise knowledge of the baryon branching fractions.

I. p_T Spectra

The bottom hadron p_T spectra are one of the biggest uncertainties on the knowledge of the relative efficiencies. Consequently, the systematic uncertainties arising from the p_T spectra are estimated conservatively, as no definitive measurements for the \bar{B}_s^0 meson and Λ_b^0 baryon are available. The systematic uncertainty assigned to the p_T spectrum for $\ell^- \Lambda_c^+$ is taken from a $\pm 2\sigma$ variation of the tuned semileptonic Λ_b^0 p_T spectrum. The spectrum is varied by $\pm 2\sigma$ in order to provide a conservative error, since the p_T spectrum measured from the semileptonic Λ_b^0 decay is incomplete. Although the $\ell^- D_s^+$ MC generated with the p_T spectrum obtained from the inclusive J/ψ cross-section measurement [20] agrees well with the data, there is the possibility that the \bar{B}_s^0 meson p_T spectrum is different from the \bar{B}^0 and B^- spectra. This possibility is accounted for by measuring the ratio $f_s/(f_u + f_d)$ with the default generator input spectrum, while the \bar{B}^0 and B^- decays are generated with the p_T spectrum inferred from Ref. [20]. Since no significant discrepancy is observed between the $\ell^- D_s^+$ data and the simulation using the p_T spectrum from Ref. [20], this is a conservative assessment of the systematic error due to the uncertainty on the \bar{B}_s^0 momentum spectrum.

J. Specific Ionization Efficiency

Accurate knowledge of the requirement on the dE/dx based likelihood ratio $\mathcal{LR}(p)$ on the proton in the $\Lambda_c^+ \rightarrow p K^- \pi^+$ decays is important for an accurate determination of the $\ell^- \Lambda_c^+$ efficiency relative to the semileptonic bottom hadron decay efficiencies. In order to assign an uncertainty to the knowledge of the dE/dx efficiency, the measurement of the fragmentation fractions is performed without any dE/dx cut applied to either the data or simulation. The $f_{\Lambda_b}/(f_u + f_d)$ fit result is stable and the difference with the default fit is treated as a systematic uncertainty. Removing the dE/dx cut does not produce a significant change in either f_u/f_d or $f_s/(f_u + f_d)$.

K. Λ_b^0 Polarization

The polarization of the Λ_b^0 baryon in hadronic collisions is not known. By default, the Λ_b^0 baryon is unpolarized in the simulation used in this measurement. In order to assign a systematic uncertainty to the possible polarizations of the Λ_b^0 , the extreme cases of the Λ_b^0 being fully polarized are tested to bound the effect. A systematic uncertainty is assigned when the Λ_b^0 is produced either with entirely positive helicity or entirely negative helicity.

L. Bottom Hadron Branching Fractions

Systematic uncertainties due to the knowledge of the bottom hadron branching fractions arise in two places in the sample composition procedure. First, the indirect semileptonic decays (*e.g.* $\bar{B} \rightarrow D\bar{D}X$, $\bar{D} \rightarrow \ell^- X$) contributing to the lepton-charm signals, many of which are poorly determined experimentally, and second the uncertainty in the PDG semileptonic Λ_b^0 branching fraction, $\mathcal{B}(\Lambda_b^0 \rightarrow \ell^- \bar{\nu}_\ell \Lambda_c^+ X) = (9.2 \pm 2.1)\%$ [42]. Since many of the measured indirect semileptonic decays are poorly determined, the branching fractions predicted from symmetry principles for these decay modes are used in the sample composition process to determine the systematic shift in the fragmentation fractions. The contributions of indirect semileptonic \bar{B}_s^0 decays to the $\ell^- D^+$, $\ell^- D^0$, and $\ell^- D^{*+}$ signatures are small (see Tables IX-XI), but the rate for $\bar{B}^0/B^- \rightarrow D_s^{(*)+} D^{(*)}(\ell D_s^+ X)$ decays contributing to the $\ell^- D_s^+$ final state (see Table XII) is an order of magnitude larger due to the more copious fragmentation of b quarks into \bar{B}^0 and B^- mesons versus \bar{B}_s^0 mesons. To give a sense of the maximal possible effect on $f_s/(f_u + f_d)$ if no contributions from \bar{B}^0 and B^- mesons to the $\ell^- D_s^+$ yield were accounted for, the fragmentation fraction $f_s/(f_u + f_d)$ would increase by about 10% from ~ 0.160 to ~ 0.176 . This estimate is presented for general interest, though it not used as a systematic uncertainty on the measurement, as it is known to be an incorrect assumption.

To determine the systematic uncertainty associated with the inclusive semileptonic Λ_b^0 branching fraction, the PDG value is varied within its uncertainties. This is one of the largest systematic uncertainties associated with the measurement of the Λ_b^0 fragmentation fraction.

M. Charm Branching Fractions

Another source of systematic uncertainty due to the branching fractions used in the sample composition procedure arises from the often poor knowledge of the ground state charm branching fractions, which are taken from the PDG and listed in Table VII. To determine the uncertainty in the fragmentation fractions, the central values of the ground state charm branching fractions included in the sample composition are varied, one by one, within $\pm 1\sigma$ of the PDG uncertainty. The largest shift in f_u/f_d comes from $\mathcal{B}(D^+ \rightarrow K^-\pi^+\pi^+)$, while the single largest uncertainty in $f_s/(f_u + f_d)$ is due to the large error on $\mathcal{B}(D_s^+ \rightarrow \phi\pi^+)$. A poor knowledge of $\mathcal{B}(\Lambda_c^+ \rightarrow pK^-\pi^+)$ contributes the largest single systematic uncertainty to $f_{\Lambda_b}/(f_u + f_d)$.

In addition to the poorly measured ground state charm branching fractions, many of the excited charm decays also have large uncertainties. To assess a systematic uncertainty for the limited knowledge of the excited charm decays, the excited charm branching fractions are varied by shifting half of the D^{**} branching fractions randomly up by 30%, while the other half are shifted down. When quoting the final result on the fragmentation fractions, a sep-

arate systematic uncertainty is quoted due to uncertainties on external branching fractions as indicated in Table XVII.

N. Λ_b^0 Sample Composition

A systematic uncertainty is assigned for the uncertain knowledge of the Λ_b^0 sample composition (see Section III). The Λ_b^0 sample composition is considered without any of the non-resonant baryon modes included, while the total semileptonic branching fraction in both cases is required to be $\mathcal{B}(\Lambda_b^0 \rightarrow \ell^- \bar{\nu}_\ell \Lambda_c^+ X) = 9.2\%$. A systematic effect for a potential mis-modeling of the decay is also considered and found to be negligible. This uncertainty is determined by evaluating the width difference of the $m(\ell^- \Lambda_c^+)$ distribution in both the data and the Monte Carlo simulation. The RMS of the data distribution is $451 \text{ MeV}/c^2$, while the RMS of the MC is $455 \text{ MeV}/c^2$. The ratio of excited to ground state $\Lambda_b^0 \rightarrow \ell^- \bar{\nu}_\ell \Lambda_c^+$ decays is changed in the simulation such that the RMS of the simulated $m(\ell^- \Lambda_c^+)$ distribution decreases by $4 \text{ MeV}/c^2$, producing a 0.017 shift in $f_{\Lambda_b}/(f_u + f_d)$. Both uncertainties result in a total systematic uncertainty of 0.047 on $f_{\Lambda_b}/(f_u + f_d)$.

O. Total Systematic Uncertainty

The total systematic uncertainties due to the knowledge of the relative efficiencies, obtained by adding the individual systematic uncertainties related to the determination of the efficiencies used in the parameterization of the sample composition in quadrature, are $\{^{+0.025}_{-0.045}\}$ for f_u/f_d , $\{^{+0.011}_{-0.010}\}$ for $f_s/(f_u + f_d)$, and $\{^{+0.058}_{-0.056}\}$ for $f_{\Lambda_b}/(f_u + f_d)$. When uncertainties arising from branching fractions are included, the uncertainties increase to $\{^{+0.062}_{-0.074}\}$ for f_u/f_d , $\{^{+0.058}_{-0.035}\}$ for $f_s/(f_u + f_d)$, and $\{^{+0.141}_{-0.103}\}$ for $f_{\Lambda_b}/(f_u + f_d)$, as given in Table XVII.

VII. FINAL RESULTS AND DISCUSSION

The weighted average of the fragmentation fractions between the electron plus displaced track and muon plus displaced track samples yields:

$$\begin{aligned} \frac{f_u}{f_d} &= 1.054 \pm 0.018 \text{ (stat)} ^{+0.025}_{-0.045} \text{ (sys)} \pm 0.058 \text{ (\mathcal{B})}, \\ \frac{f_s}{f_u + f_d} &= 0.160 \pm 0.005 \text{ (stat)} ^{+0.011}_{-0.010} \text{ (sys)} ^{+0.057}_{-0.034} \text{ (\mathcal{B})}, \\ \frac{f_{\Lambda_b}}{f_u + f_d} &= 0.281 \pm 0.012 \text{ (stat)} ^{+0.058}_{-0.056} \text{ (sys)} ^{+0.128}_{-0.087} \text{ (\mathcal{B})}. \end{aligned}$$

Since this analysis potentially ignores the production of b baryons that might not decay into the Λ_b^0 final state, no constraint is applied requiring the fragmentation fractions f_u , f_d , f_s , and f_{Λ_b} to sum to unity. The correlation matrix for the fit is shown in Table XVIII.

TABLE XVII: Compilation of systematic uncertainties assigned.

Systematics	f_u/f_d	$f_s/(f_u + f_d)$	$f_{\Lambda_b}/(f_u + f_d)$
False Leptons	-0.039	-0.001	+0.018
Variation of cuts	± 0.011	± 0.0003	± 0.019
D_s^+ reflection in D^+	+0.001	+0.00002	+0.0001
XFT eff.	± 0.003	± 0.0004	± 0.006
Single track eff.	± 0.014	± 0.002	± 0.002
Sample comp. lifetimes	$^{+0.018}_{-0.014}$	± 0.006	± 0.002
MC statistics	± 0.005	± 0.0007	± 0.0006
Bottom hadron lifetimes	-	$^{+0.005}_{-0.001}$	$^{+0.0077}_{-0.0136}$
p_T spectra	-	± 0.008	± 0.049
dE/dx eff.	-	-	± 0.012
Λ_b^0 polarization	-	-	± 0.007
Total (eff.)	$^{+0.025}_{-0.045}$	$^{+0.011}_{-0.010}$	$^{+0.058}_{-0.056}$
Physics bkgns	± 0.001	± 0.002	± 0.001
$\mathcal{B}(\Lambda_b^0 \rightarrow \ell^- \bar{\nu}_\ell \Lambda_c^+ X)$	-	-	$^{+0.076}_{-0.048}$
$\mathcal{B}(\Lambda_c^+ \rightarrow p K^- \pi^+)$	-	-	$^{+0.091}_{-0.053}$
$\mathcal{B}(D^+ \rightarrow K^- \pi^+ \pi^+)$	± 0.054	± 0.003	± 0.010
$\mathcal{B}(D^0 \rightarrow K^- \pi^+)$	± 0.020	± 0.003	± 0.003
$\mathcal{B}(D_s^+ \rightarrow \phi \pi^+)$	± 0.0006	$^{+0.057}_{-0.034}$	± 0.001
$\mathcal{B}(D^{**})$	± 0.010	± 0.004	± 0.011
Λ_b^0 sample composition	-	-	± 0.047
Total (\mathcal{B})	± 0.058	$^{+0.057}_{-0.034}$	$^{+0.128}_{-0.087}$
Total	$^{+0.062}_{-0.074}$	$^{+0.058}_{-0.035}$	$^{+0.141}_{-0.103}$

This result is in agreement with the world average of the fragmentation fraction of B^- relative to \bar{B}^0 , which is expected to be equal to unity [42]. The result on the relative fragmentation fraction $f_s/(f_u + f_d)$ presented in this paper agrees with the LEP average $f_s/(f_u + f_d) = 0.135 \pm 0.011$ [42] within one standard deviation. Separating $\mathcal{B}(D_s^+ \rightarrow \phi \pi^+)$ from the result of $f_s/(f_u + f_d)$, for comparison with the world average, gives:

$$\frac{f_s}{f_u + f_d} \times \mathcal{B}(D_s^+ \rightarrow \phi \pi^+) = (5.76 \pm 0.18 \text{ (stat)} ^{+0.45}_{-0.42} \text{ (sys)}) \times 10^{-3}.$$

There is no significant indication of a higher rate of b -quark fragmentation to \bar{B}_s^0 mesons at the Tevatron which would contribute to the anomalous Run I values of $\bar{\chi}$ [11, 12, 19]. The uncertainty on f_s will significantly decrease with an improved measurement of $\mathcal{B}(D_s^+ \rightarrow \phi \pi^+)$, which is in preparation by the CLEO-c experiment [57].

Separating the poorly known $\mathcal{B}(\Lambda_c^+ \rightarrow p K^- \pi^+)$ and $\mathcal{B}(\Lambda_b^0 \rightarrow \ell^- \bar{\nu}_\ell \Lambda_c^+)$ from the results of

TABLE XVIII: Correlation matrix of fit parameters.

Parameter	f_u/f_d	$f_s/(f_u + f_d)$	$f_{\Lambda_b}/(f_u + f_d)$	Γ	Γ^*	Γ^{**}	$N(\bar{B}^0)$
f_u/f_d	1.0	-0.021	-0.053	-0.011	-0.135	0.162	-0.249
$f_s/(f_u + f_d)$		1.0	0.077	-0.015	-0.058	0.150	-0.116
$f_{\Lambda_b}/(f_u + f_d)$			1.0	0.425	0.563	0.239	-0.575
Γ				1.0	0.657	-0.122	-0.674
Γ^*					1.0	0.134	-0.853
Γ^{**}						1.0	-0.436
$N(\bar{B}^0)$							1.0

$f_{\Lambda_b}/(f_u + f_d)$ yields:

$$\frac{f_{\Lambda_b}}{f_u + f_d} \times \mathcal{B}(\Lambda_c^+ \rightarrow p K^- \pi^+) = (14.1 \pm 0.6 \text{ (stat)} {}^{+5.3}_{-4.4} \text{ (sys)}) \times 10^{-3} \text{ or}$$

$$\frac{f_{\Lambda_b}}{f_u + f_d} \times \mathcal{B}(\Lambda_b^0 \rightarrow \ell^- \bar{\nu}_\ell \Lambda_c^+) \mathcal{B}(\Lambda_c^+ \rightarrow p K^- \pi^+) = (12.9 \pm 0.6 \text{ (stat)} \pm 3.4 \text{ (sys)}) \times 10^{-4}.$$

This quantity can be compared more naturally with the LEP results, which quote $f_{\Lambda_b} \times \mathcal{B}(\Lambda_b^0 \rightarrow \ell^- \bar{\nu}_\ell \Lambda_c^+) \times \mathcal{BR}(\Lambda_c^+ \rightarrow p K^- \pi^+)$ [58, 59]. When all branching fractions with large uncertainties are factored out, f_{Λ_b} is $\sim 2.3\sigma$ higher than the LEP results, assuming that $f_u = f_d = 39.7\%$ at LEP. In addition, this measurement of $f_{\Lambda_b}/(f_u + f_d)$ is approximately twice as large as the world average of $f_{\Lambda_b}/(f_u + f_d) = 0.125 \pm 0.020$ [42], which is dominated by the LEP results.

A. Discussion of Results

The difference between the f_{Λ_b} result presented in this paper and the LEP results may be explained, at least in part, by the different environment of hadro-production of bottom hadrons in $p\bar{p}$ collisions. In addition to this effect, the transverse momentum of the bottom hadrons is significantly lower for the data used in this measurement, $\langle p_T(b) \rangle \sim 15 \text{ GeV}/c$, than the $b\bar{b}$ data collected at the Z pole used in the LEP measurements, $\langle p_T(b) \rangle \sim 45 \text{ GeV}/c$. To study a potential momentum dependence of f_{Λ_b} , the behavior of the fragmentation fractions in bins of the lepton-charm p_T is investigated. Note that the fragmentation fractions can depend on momentum, and the fractions reported here are for momenta integrated above the effective p_T^{min} which is chosen to be $7 \text{ GeV}/c$ in this analysis.

For this study the electron and muon datasets of the lepton-charm candidates are divided into three momentum ranges with similar statistics in each bin. The chosen momentum bins are less than $11 \text{ GeV}/c$, from 11 to $14 \text{ GeV}/c$, and greater than $14 \text{ GeV}/c$. The lepton-charm yields and corresponding efficiencies are redetermined in each momentum interval and the fit for the fragmentation fractions is repeated. The weighted average of $f_{\Lambda_b}/(f_u + f_d)$ obtained

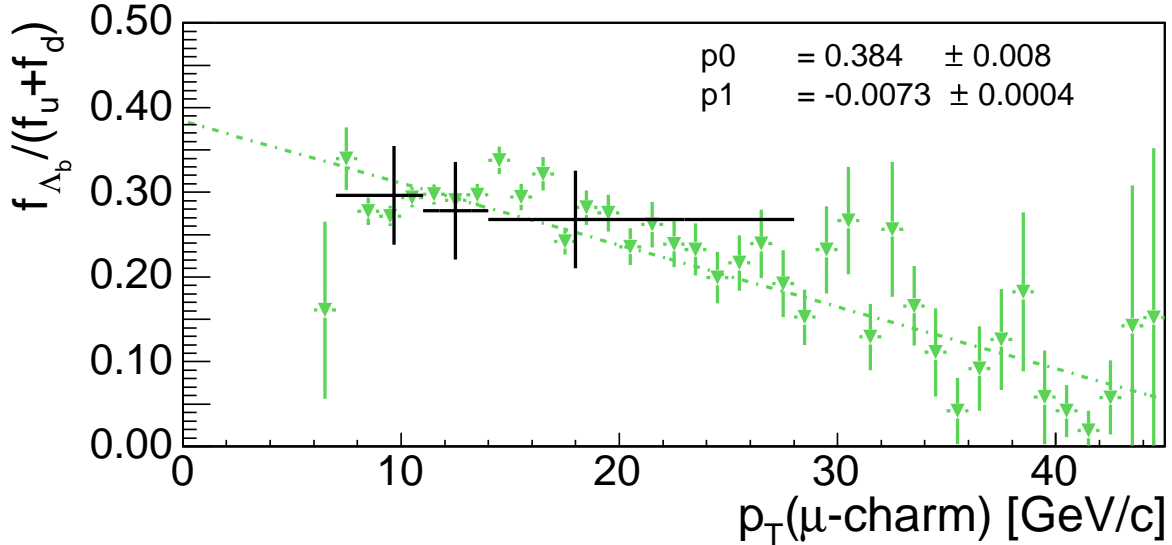


FIG. 16: Determination of $f_{\Lambda_b}/(f_u + f_d)$ for three momentum ranges (three points with error bars) overlaid on Monte Carlo simulation scaling of $f_{\Lambda_b}/(f_u + f_d)$ as a function of $p_T(\ell^-\Lambda_c^+)$ (triangles). The dashed line is a fit to the Monte Carlo simulation.

from the $e+$ SVT and $\mu+$ SVT data in the three p_T ranges is shown as three points with error bars in Fig. 16. The uncertainties on these points include the systematic uncertainties on the efficiencies, but do not reflect the uncertainties from branching fractions. The data points are consistent with a decrease in the ratio $f_{\Lambda_b}/(f_u + f_d)$ with increasing bottom hadron momentum. However, in the near future, larger CDF datasets of lepton-charm events will provide increased statistics for a more adequate extrapolation of this suggested momentum dependence of f_{Λ_b} as compared to B -hadron momenta at LEP.

To obtain a better extrapolation of the indicated momentum dependence of b -quark fragmentation into Λ_b^0 baryons, the Monte Carlo simulation tuned on the data is used to estimate such a momentum dependence. The inclusive $\Lambda_b^0 \rightarrow \ell^-\bar{\nu}_\ell \Lambda_c^+ X$ simulation generated with the tuned semileptonic Λ_b^0 p_T spectrum is compared with the inclusive $\bar{B}^0 \rightarrow \ell^-\bar{\nu}_\ell D^+ X$ simulation generated with the p_T spectrum inferred from the inclusive J/ψ cross-section measurement [20]. Assuming that the inclusive Monte Carlo samples provide a good description of the $\ell^-\Lambda_c^+$ and ℓ^-D^+ data, as demonstrated in Section IV A 1, the ratio of the momentum dependence of both datasets provides an estimate of the shape of the ratio of $dN/dp_T(\Lambda_b^0)$ to $dN/dp_T(\bar{B}^0)$. The ratio of both distributions is therefore proportional to f_{Λ_b}/f_d and thus to $f_{\Lambda_b}/(f_u + f_d)$, assuming $f_u = f_d$. To obtain an absolute normalization, the ratio of the two distributions is fixed at the mean $p_T(\ell^-\Lambda_c^+)$ of the present measurement, $\langle p_T(\ell^-\Lambda_c^+) \rangle \approx 14.1$ GeV/c, to the central value of $f_{\Lambda_b}/(f_u + f_d) = 0.281$ as obtained in this analysis. The result of this MC study is shown as triangles with error bars in Fig. 16. Fitting a straight line to these points agrees well with the three data points of $f_{\Lambda_b}/(f_u + f_d)$ obtained in three momentum bins as described above. Extrapolating the line

to $p_T(\ell^-\Lambda_c^+) \sim 35$ (40) GeV/ c yields a value for $f_{\Lambda_b}/(f_u + f_d)$ of about 0.128 (0.092). This is close to the world average of $f_{\Lambda_b}/(f_u + f_d) = 0.125 \pm 0.020$ [42], which is dominated by the LEP results. This study indicates a possible momentum dependence of the b -baryon fragmentation that would explain the difference between the f_{Λ_b} result presented in this paper and the LEP measurements.

Finally, knowledge of f_{Λ_b} will improve with better measurements of the $\Lambda_c^+ \rightarrow pK^-\pi^+$ branching fraction and the semileptonic $\Lambda_b^0 \rightarrow \ell^-\bar{\nu}_\ell\Lambda_c^+X$ branching fractions, in addition to better measurements of the Λ_b^0 semileptonic sample composition, particularly the measurement of the $\Lambda_b^0 \rightarrow \ell^-\bar{\nu}_\ell\Lambda_c(2593)^+$ and $\Lambda_b^0 \rightarrow \ell^-\bar{\nu}_\ell\Lambda_c(2625)^+$ branching fractions. Additionally, a definitive measurement of the p_T spectrum of Λ_b^0 baryons in $p\bar{p}$ collisions compared to the momentum spectrum of \bar{B}^0 mesons measured with fully reconstructed Λ_b^0 and \bar{B}^0 decay modes will shed light on expected differences in the momentum spectra and significantly reduce the systematic uncertainty of a measurement of the b -quark fragmentation fractions in the future.

Acknowledgments

We thank the Fermilab staff and the technical staffs of the participating institutions for their vital contributions. This work was supported by the U.S. Department of Energy and National Science Foundation; the Italian Istituto Nazionale di Fisica Nucleare; the Ministry of Education, Culture, Sports, Science and Technology of Japan; the Natural Sciences and Engineering Research Council of Canada; the National Science Council of the Republic of China; the Swiss National Science Foundation; the A.P. Sloan Foundation; the Bundesministerium für Bildung und Forschung, Germany; the Korean Science and Engineering Foundation and the Korean Research Foundation; the Science and Technology Facilities Council and the Royal Society, UK; the Institut National de Physique Nucléaire et Physique des Particules/CNRS; the Russian Foundation for Basic Research; the Comisión Interministerial de Ciencia y Tecnología, Spain; the European Community's Human Potential Programme; the Slovak R&D Agency; and the Academy of Finland.

- [1] H. D. Politzer, Phys. Rev. Lett. **30**, 1346 (1973).
- [2] D. J. Gross and F. Wilczek, Phys. Rev. Lett. **30**, 1343 (1973).
- [3] R. D. Field and R. P. Feynman, Nucl. Phys. **B136**, 1 (1978).
- [4] The transverse momentum, p_T , is the component of the track momentum, p , transverse to the proton beam direction.
- [5] F. Abe et al. (CDF Collaboration), Phys. Rev. D **54**, 6596 (1996).
- [6] F. Abe et al. (CDF Collaboration), Phys. Rev. D **60**, 092005 (1999).

- [7] A. A. Affolder et al. (CDF Collaboration), Phys. Rev. Lett. **84**, 1663 (2000).
- [8] P. Abreu et al. (DELPHI Collaboration), Phys. Lett. B **289**, 199 (1992).
- [9] P. D. Acton et al. (OPAL Collaboration), Phys. Lett. B **295**, 357 (1992).
- [10] D. Buskulic et al. (ALEPH Collaboration), Phys. Lett. B **361**, 221 (1995).
- [11] F. Abe et al. (CDF Collaboration), Phys. Rev. D **55**, 2546 (1997).
- [12] D. Acosta et al. (CDF Collaboration), Phys. Rev. D **69**, 012002 (2004).
- [13] D. Buskulic et al. (ALEPH Collaboration), Phys. Lett. B **284**, 177 (1992).
- [14] D. Buskulic et al. (ALEPH Collaboration), Z. Phys. C **62**, 179 (1994).
- [15] P. Abreu et al. (DELPHI Collaboration), Phys. Lett. B **332**, 488 (1994).
- [16] M. Acciarri et al. (L3 Collaboration), Eur. Phys. J. C **13**, 47 (2000).
- [17] P. Abreu et al. (DELPHI Collaboration), Eur. Phys. J. C **20**, 455 (2001).
- [18] G. Abbiendi et al. (OPAL Collaboration), Phys. Lett. B **577**, 18 (2003).
- [19] E. L. Berger et al., Phys. Rev. Lett. **86**, 4231 (2001).
- [20] D. Acosta et al. (CDF Collaboration), Phys. Rev. D **71**, 032001 (2005).
- [21] R. Blair et al. (CDF Collaboration) (1996), FERMILAB-PUB-96-390-E.
- [22] A. Sill (CDF Collaboration), Nucl. Instrum. Methods A **447**, 1 (2000).
- [23] C. S. Hill (CDF Collaboration), Nucl. Instrum. Methods A **530**, 1 (2004).
- [24] A. A. Affolder et al. (CDF Collaboration), Nucl. Instrum. Methods A **453**, 84 (2000).
- [25] A. A. Affolder et al. (CDF Collaboration), Nucl. Instrum. Methods A **526**, 249 (2004).
- [26] D. Acosta et al. (CDF Collaboration), Phys. Rev. Lett. **93**, 032001 (2004).
- [27] D. Acosta et al. (CDF Collaboration), Phys. Rev. Lett. **91**, 241804 (2003).
- [28] A. Abulencia et al. (CDF Collaboration), Phys. Rev. Lett. **97**, 012002 (2006).
- [29] L. Balka et al. (CDF Collaboration), Nucl. Instrum. Methods A **267**, 272 (1988).
- [30] S. Bertolucci et al. (CDF Collaboration), Nucl. Instrum. Methods A **267**, 301 (1988).
- [31] A. Abulencia et al. (CDF Collaboration), J. Physics G **34**, 2457 (2007).
- [32] G. Ascoli et al., Nucl. Instrum. Methods A **268**, 33 (1988).
- [33] T. Dorigo (CDF Collaboration), Nucl. Instrum. Methods A **461**, 560 (2001).
- [34] K. Anikeev et al. (CDF Collaboration), IEEE Trans. Nucl. Sci. **47**, 65 (2000).
- [35] K. Anikeev et al. (CDF Collaboration), Comput. Phys. Commun. **140**, 110 (2001).
- [36] A. Bardi et al., Nucl. Instrum. Methods A **485**, 178 (2002).
- [37] E. J. Thomson et al., IEEE Trans. Nucl. Sci. **49**, 1063 (2002).
- [38] W. Ashmanskas et al. (CDF Collaboration), IEEE Trans. Nucl. Sci. **49**, 1177 (2002).
- [39] D. E. Acosta et al. (CDF Collaboration), Phys. Rev. D **71**, 052003 (2005).
- [40] A. Abulencia et al. (CDF Collaboration), Phys. Rev. Lett. **97**, 062003 (2006).
- [41] A. Abulencia et al. (CDF Collaboration), Phys. Rev. Lett. **97**, 242003 (2006).
- [42] S. Eidelman et al. (Particle Data Group), Phys. Lett. B **592**, 1 (2004).
- [43] K. R. Gibson, Ph.D. thesis, Carnegie Mellon, FERMILAB-THESIS-2006-09 (2006).
- [44] S.-S. Yu, Ph.D. thesis, Univ. of Pennsylvania, FERMILAB-THESIS-2005-11 (2005).

- [45] D. J. Lange, Nucl. Instrum. Methods A **462**, 152 (2001).
- [46] R. Brun, R. Hagelberg, M. Hansroul, and J. C. Lassalle, CERN-DD-78-2-REV (1978).
- [47] R. Brun and F. Carminati (1991), prepared for 9th International Conference on Computing in High-energy Physics (CHEP 91), Tsukuba, Japan, 11-15 Mar 1991.
- [48] E. Gerchtein and M. Paulini, ECONF **C0303241**, TUMT005 (2003), arXiv:physics/0306031.
- [49] D. Acosta et al. (CDF Collaboration), Phys. Rev. Lett. **96**, 202001 (2006).
- [50] N. Isgur and M. B. Wise, Phys. Rev. D **43**, 819 (1991).
- [51] J. L. Goity and W. Roberts, Phys. Rev. D **51**, 3459 (1995).
- [52] M. Pervin, W. Roberts, and S. Capstick, Phys. Rev. C **72**, 035201 (2005).
- [53] A. K. Leibovich and I. W. Stewart, Phys. Rev. D **57**, 5620 (1998).
- [54] Q. He et al. (CLEO Collaboration), Phys. Rev. Lett. **95**, 121801 (2005).
- [55] G. Giurgiu, Ph.D. thesis, Carnegie Mellon, FERMILAB-THESIS-2005-41 (2005).
- [56] V. Tiwari, Ph.D. thesis, Carnegie Mellon, FERMILAB-THESIS-2007-09 (2007).
- [57] N. Adam (CLEO Collaboration) (2006), arXiv:hep-ex/0607079.
- [58] P. Abreu et al. (DELPHI Collaboration), Z. Phys. C **68**, 375 (1995).
- [59] R. Barate et al. (ALEPH Collaboration), Eur. Phys. J. C **2**, 197 (1998).